Nucleation and magnetism of supercooled Co-B metallic liquid under high magnetic field

Yixuan He

To cite this version:

Yixuan He. Nucleation and magnetism of supercooled Co-B metallic liquid under high magnetic field. Physics [physics]. UGA (Université Grenoble Alpes), 2019. English. NNT : . tel-02380643

HAL Id: tel-02380643
https://theses.hal.science/tel-02380643

Submitted on 26 Nov 2019

Communauté
UNIVERSITÉ Grenoble Alpes

THÈSE

Pour obtenir le grade de

DOCTEUR DE LA COMMUNAUTE UNIVERSITE GRENOBLE ALPES

préparée dans le cadre d'une cotutelle entre la Communauté Université Grenoble Alpes et la Nortwestern Polytechnical University (Xi'an, Chine)

Spécialité : **Physique**

Arrêté ministériel : le 6 janvier 2005 – 25 mai 2016

Présentée par **Yixuan HE**

Thèse codirigée par **Eric BEAUGNON et Jinshan LI**

préparée au sein des **Laboratoires CNRS/LNCMI et State Key Laboratory of Solidification Processing**

dans les Écoles Doctorales de Physique de Grenoble et Graduate school of Northwestern Polytechnical University

Nucléation et magnétisme des métaux liquides Co-B en surfusion sous champ magnétique intense

Nucleation and magnetism of supercooled Co-B metallic liquid under high magnetic field

Thèse soutenue publiquement le **25 Octobre 2019**,
devant le jury composé de :

Mme Céline DARIE,
Professeur, Université Grenoble Alpes, Président
M. Qiang WANG
Professeur, Northeastern University, Shenyang, Rapporteur
M. Damien FABREGUE
Professeur, INSA Lyon, Rapporteur
M. Yunbo ZHONG
Professeur, Shanghai University, Examinateur
M. Jinshan LI
Professeur, Northwestern Polytechnical University, Xi'an, Codirecteur de thèse
M. Eric BEAUGNON
Professeur, Université Grenoble Alpes, Codirecteur de thèse
M. Jun WANG
Professeur, Northwestern Polytechnical University, Xi'an, membre invité

Abstract

In the present work, a thorough investigation has been conducted on the Co-B alloys in terms of the microstructure evolution during non-equilibrium solidification with/without magnetic field and the temperature induced liquid-liquid structure transition.

In this work, a Co-20at.%B hypereutectic alloys was undercooled by the melt fluxing technique and the microstructure was characterized by the back-scattering diffraction technique. A transition from hypereutectic to hypoeutectic was found at a critical undercooling of ΔT=119 K. When ΔT<119 K, a primary directional dendritic β-Co_3B phase surrounded by the regular of α-Co+β-Co_3B lamellar eutectics was found. When ΔT>119 K, the above hypereutectic microstructure changes into hypoeutectic structure with the α-Co phase as the primary phase. According to dendrite growth model, the transition from hypereutectic to hypoeutectic can be ascribed to the higher growth velocity of the α-Co phase than the β-Co_3B phase, i.e., the growth-controlled mechanism. The current work shows also that there is a coupled zone skewed to the β-Co_3B phase in the Co-B alloys system.

Cyclic superheating and cooling were carried out for the undercooled hypereutectic Co-20at.%B, eutectic Co-18.5at.%B and hypoeutectic Co-17at.%B alloys. For each alloy, there is a critical overheating temperature T_c^0 at which there is a sharp increase of the mean undercooling, i.e., the mean undercooling is about 80 ℃ when the overheating temperature is below T_c^0, whereas the mean undercooling is about 200 ℃ when the overheating temperature is above T_c^0. DSC measurements show that there is a thermal absorption peak in the heating process, the peak temperature of which is nearly equal to the critical overheating temperature, indicating that the temperature induced liquid-liquid structure transition does occur and should relate highly to nucleation in the undercooled Co-B eutectic melts. The effect of the liquid-liquid structure transition on nucleation was interpreted by the recent nucleation theory that considers the structures of overheated melts, and the composition-dependent overheating temperature was ascribed to the change of local favored structures. The present work provides further evidences for the liquid-liquid structure transition and is helpful for understanding solidification in undercooled melts.

By in situ measuring the magnetization, the temperature induced liquid-liquid structure transition was further investigated. A magnetization anomaly in term of the non-Curie-Weiss temperature dependence of magnetization was observed in the overheated state, demonstrating a temperature induced liquid-liquid structure transition. This anomalous behavior was found to be a universal formula for the Co-B binary alloy system. A transition point (T_0), two different Curie constants and two paramagnetic Curie temperatures ($\theta(\mathrm{L_I})$, $\theta(\mathrm{L_{II}})$) corresponding to two distinct kinds of liquids (i.e., high-magnetization liquid I and low-magnetization liquid II) are determined. The Curie constant of liquid II was found much higher, which is attributed to the survived covalent bond below T_0. The effects of magnetic field intensity on the liquid-liquid structure transition and paramagnetic Curie temperatures are studied. T_0 and $\theta(\mathrm{L_{II}})$ are found not sensitive to the field intensity, whereas, $\theta(\mathrm{L_I})$ shifts to lower temperatures with the increasing magnetic field intensity. With the increased concentration of Co, T_0, $\theta(\mathrm{L_I})$ and $\theta(\mathrm{L_{II}})$ shift to higher temperatures and the Curie constants for the liquid I and liquid II decrease. Based on the location of T_0, a guideline was drawn above the *liquidus* in the Co-B phase diagram, which could provide a significant guidance to the practical melt treatment.

Under an imposed magnetic field, a morphological alignment was found for the primary α-Co phase with its primary dendrite trunk or long axis paralleling to the direction of magnetic field. The primary α-Co phases are rod-like or spherical at relatively high undercooling, and the application of magnetic field is more conducive to obtain such kind of α-Co phases. The magnetic energy, magnetic torque and time required for rotation were analyzed theoretically to evaluate the magnetic alignment and alignment mechanisms. The dipolar forces between particles were calculated, based on which the phenomenon that the primary α-Co particles self-organize as chain-like stacking was described.

Key words: Co-B alloys; Non-equilibrium solidification; Nucleation; Magnetic field; Liquid-liquid structure transition; Phase selection.

Résumé

Dans le cadre du présent travail, une étude approfondie a été menée sur les alliages Co-B en termes d'évolution de la microstructure lors d'une solidification hors équilibre avec ou sans champ magnétique ainsi que sur une transition liquide-liquide induite par la température.

Dans ce travail, un alliage hypereutectique Co-20at.%B a été sous-refroidi par la technique de l'encapsulation vitreuse et la microstructure a été caractérisée par la technique de microscopie électronique par électrons rétrodiffusés. Une transition de l'hypereutectique à l'hypoeutectique a été trouvée à un sous-refroidissement critique de $\Delta T=119$ K. Quand $\Delta T<119$ K, une phase dendritique directionnelle primaire β-Co_3B entourée par l'eutectique lamellaire régulière de α-Co+β-Co_3B a été observée. Lorsque $\Delta T>119$ K, la microstructure hypereutectique ci-dessus se transforme en structure hypoeutectique avec la phase α-Co comme phase primaire. Selon le modèle de croissance de la dendrite, le passage de l'hypereutectique à l'hypoeutectique peut être attribué à la vitesse de croissance plus élevée de la phase α-Co que de la phase β-Co_3B, c'est-à-dire un mécanisme contrôlé par la croissance. Les travaux actuels montrent également qu'il existe une zone de couplage dévié avec la phase β-Co_3B dans le système des alliages Co-B.

La surchauffe et le refroidissement cycliques ont été effectués pour les alliages hypereutectiques sous-refroidis Co-20at.%B, eutectiques Co-18.5at.%B et hypoeutectiques Co-17at.%B. Pour chaque alliage, il y a une température critique de surchauffe T_c^0 à laquelle il y a une brutale augmentation du sous-refroidissement moyen, c'est-à-dire passant de 80 ℃ pour une surchauffe inférieure T_c^0, à 200 ℃ pour une surchauffe supérieure à T_c^0. Les mesures DSC montrent qu'il y a un pic d'absorption thermique dans le processus de chauffage, dont le pic de température est presque égal à la température critique de surchauffe, ce qui indique qu'une transition structurale liquide-liquide induite par la température se produit et doit être étroitement liée à la nucléation dans le liquide eutectique Co-B sous refroidi. L'effet de la transition structurale liquide-liquide sur la nucléation a été interprété par la récente théorie de la nucléation qui considère les structures des liquides en fusion surchauffées, et la température de surchauffe critique T_c^O, dépendante de la composition, a été attribuée au changement de structures préférentielles locales. Le présent travail fournit d'autres preuves de la transition structurale liquide-liquide et est utile pour comprendre la solidification dans les métaux liquides sous-refroidis.

Grace à une mesure in situ de l'aimantation, la transition structurale liquide-liquide induite par la température a été étudiée plus en profondeur. Une anomalie d'aimantation en terme de non dépendance de l'aimantation selon une loi de Curie-Weiss a été observée à l'état surchauffé, ce qui démontre une transition structurale liquide-liquide induite par la température. Ce comportement anormal s'est avéré être une règle universelle pour le système d'alliage binaire Co-B. Une température de transition (T_0) et deux températures de Curie paramagnétiques ($\theta(L_I)$, $\theta(L_{II})$) correspondant à deux structures différentes des liquides sont déterminées. Les effets de l'intensité du champ magnétique sur la transition liquide-liquide et les températures de Curie paramagnétiques sont étudiés. T_0 et $\theta(L_{II})$ ne sont pas sensibles à l'intensité du champ, tandis que $\theta(L_I)$ passe à des températures plus basses avec une intensité croissante du champ magnétique. Avec une concentration croissante de Cobalt, T_0, $\theta(L_I)$ et $\theta(L_{II})$ passent à des températures plus élevées et les constantes de Curie pour le liquide I et le liquide II diminuent. En se basant sur la mesure de T_0, une ligne directrice a été tracée au-dessus du liquidus dans le diagramme de phase Co-B, ce qui pourrait fournir une aide significative pour le traitement pratique de fusion de l'alliage.

Sous l'effet d'un champ magnétique imposé, un alignement morphologique a été trouvé pour la phase primaire α-Co avec son tronc primaire de dendrite ou son grand axe parallèle à la direction du champ magnétique. Les phases primaires de α-Co sont de formes cylindriques ou sphériques avec un sous-refroidissement relativement élevé, et l'application d'un champ magnétique est plus propice à l'obtention de ce type de phases α-Co. L'énergie magnétique, le couple magnétique et le temps requis pour la rotation ont été analysés théoriquement pour évaluer l'alignement magnétique et les mécanismes d'alignement. Les forces dipolaires entre les particules ont été calculées sur la base desquelles le phénomène d'auto-organisation des particules primaires de α-Co sous forme d'empilement en chaîne a été décrit.

Mots clés : Alliages Co-B ; Solidification non équilibrée ; Nucleation ; Champ magnétique ; Transition de structure liquide-liquide ; Sélection de phase.

Content

Chapter 1 Literature review

1.1 General introduction

Most metallic materials experienced one or several processes from liquid to solid before they were made into components. The process of liquid to solid has crucial influence on the mechanical, physical properties and related to lots of defects, especially metallurgical defects, which always leads to the failure of important components. As a result, investigation on the liquid metallic melts is of great importance and attracts us a lot of attention.

The metallic melt used to be traditionally considered as homogenous and isotropic liquid according to the classical thermodynamics theory. However, as the experimental and numerical methods develop, recent research results show that the melt has short range order, medium range order, topological range order etc., and the liquid state polymorphism is widely accepted [1-17]. Thus it is widely accepted that liquid-liquid structure transition (L-LST) exists in almost all the materials, e.g., some metallic melts [1, 9, 18, 19], metalloid liquids [20, 21], molecular liquids [22, 23]. It can be in either single component liquid like Si [24], P [20], C [25], Ca [26], Te [27], or multi-component liquid, e.g., $Co_{76}Sn_{24}$ [28], H_2O [29], SiC [30]. In this work our attention is paid to the metallic melts only.

In this chapter, Section 1.2 provides basic knowledge of L-LST. In Section 1.3 we review the recent experimental methods to characterize the L-LST and in the following sections, we give a detailed review on the results of experimental study of L-LST and its impact on the nucleation, microstructure and properties. Finally, we summarize the chapter and outline several prospective topics of future research.

1.2 Basic concepts of liquid-liquid structure transition

There is no ideal model to describe the liquid structure because of its uncertainty and instability. Different from crystal structure, liquid structure is non-symmetric and long-range disordered. Experiments and numerical simulation results shows that there are nomadic atom clusters surrounded by free atoms in the liquid. The size of cluster changes with temperature. Not just thermal expansion, there are growing experimental and theoretical supports for the existence of thermal contraction of atom clusters in the heating process [31-34].

1.2.1 Classification of liquid-liquid structure transition

A single-component liquid may have more than two kinds of isotropic liquid states and the transition between these different states is called liquid-liquid structure transition [16]. In general, L-LST can be classified by the condition in which it occurs, namely pressure induced L-LST, temperature induced L-LST and other external physical field induced L-LST. Pressure induced L-LST mostly occurs in molecular liquid such as C [25], P [20]. However, the influence of pressure on metallic melt is not as obvious as that on molecular liquid so the L-LST in metallic melt is mostly temperature or other external physical field or both induced.

Another classification of L-LST is based on the reversibility of the transition process, namely reversible L-LST and irreversible L-LST. Fig. 1.1a shows the temperature dependence of nuclear magnetic resonance observables in metallic glass forming liquid $La_{50}Al_{35}Ni_{15}$ [35]. The Knight shift (K_s) of the liquid, which is sensitive to changes of structures, displays a non-linear dependence on temperature during cooling process. The crossover demonstrably indicates that a temperature-induced L-LST in the melt. Subsequently, the sample was reheated again and the continuous reheating curve of K_s reproduces the values of the cooling curve except a hysteresis in the temperature range of 1008-1033 K, which is due to the expected undercooling effect. This observation clearly unveils that such transition is reversible. The inverse magnetization (1/M) as a function of temperature curve of $Co_{76}Sn_{24}$ alloy is shown in Fig. 1.1b [28]. During heating, a distinct crossover is observed at T_0. During cooling, the 1/M-T curve nearly overlaps with the heating curve above T_0 but remains incessant with the identical slope below T_0, which indicates the L-LST is irreversible. Although the mechanism of reversible and irreversible L-LST is not clear, it refers to the species of the Short Range Orders and the properties of elements.

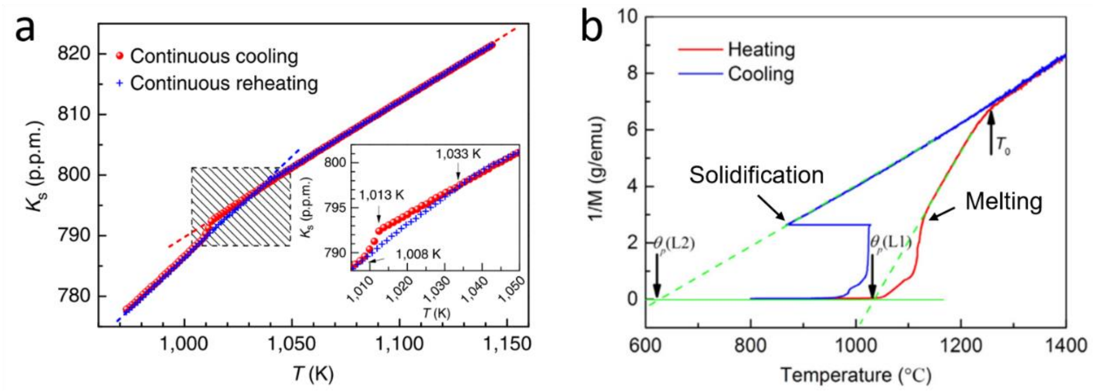

Fig. 1.1. (a) T dependence of ^{27}Al K_s during continuous cooling and reheating in the temperature interval of 973-1143 K [35]. The liquids temperature is 970 K and the glass transition temperature is 528 K for this glass system. (b) 1/M-T curve of $Co_{76}Sn_{24}$ alloy measured in 1 T magnetic field [28].

Furthermore, the existence of L-LST can be evidenced either in an overheated liquid or in an undercooled liquid, e.g., as shown in Figs. 1.2a and 1.2b, L-LST is evidenced (a) in the $Bi_2Te_{2.7}Se_{0.3}$ melt above its melting point (620 ℃) [36] and (b) in the supercooled $Zr_{57}Nb_5Al_{10}Cu_{15.4}Ni_{12.6}$ liquid, about 115 K below the melting temperature [3].

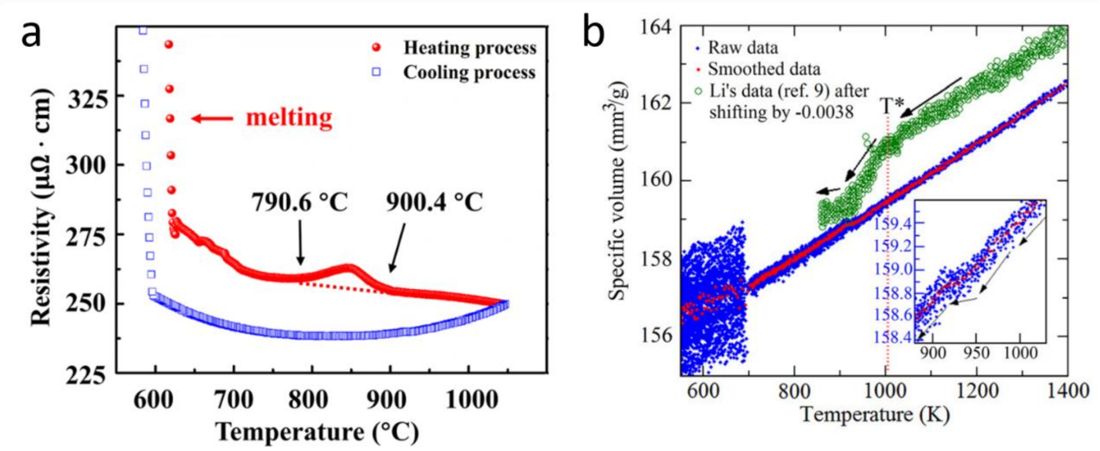

Fig. 1.2. (a) Liquid-liquid structure transition in the $Bi_2Te_{2.7}Se_{0.3}$ melt above the melting point [36], which is evidenced by an anomalous hump on the ρ-T curve during the heating process. (b) Specific volume as a function of temperature measured during cooling. A small discontinuity is indicated by arrows (see the inset) in the slope of the specific volume data, which suggests that a liquid-liquid structure transition in the $Zr_{57}Nb_5Al_{10}Cu_{15.4}Ni_{12.6}$ liquid in undercooled state [3].

1.2.2 Mechanism of the liquid-liquid structure transition in metallic melts

The mechanism of L-LST refers to the content and the behavior of atomic clusters, namely short range orders (SROs) and medium range orders (MROs), which relate to the properties of elements. Tanaka held the view that liquid is not homogeneous and in liquid locally favored structures exist [16]. The nearest-neighbor coordination difference leaves space of local structural variation of chemical and topological order [37]. Thus, the SROs (even MROs) of liquid might vary with temperatures, causing the change of thermodynamical properties. There are growing experimental and theoretical supports for the existence of L-LSTs in metallic melts and plausible three dimensional structural models can be reconstructed via simulation methods such as reverse Monte Carlo [38], *ab initio* molecular dynamics (AIMD) [39], cluster alignment method [37], etc.

Fig. 3 depicts the three-dimensional representation of average SRO of liquid Ga at the selected four temperatures using the recently-developed cluster alignment method, which describes the local atomic packing and has been applied to directly visualize the average local SRO and MRO in the liquid [37]. At 1600 K, the clusters exhibit weak SRO, indicating a highly disordered structure. The local SRO enhances upon cooling. At 600 K, the crystalline orthorhombic-like local atomic packing is detected. Combined with high-temperature and high-energy XRD measurements and AIMD simulations, an intriguing liquid structure change between two different Ga liquid regimes is discovered, i.e., the high-coordinated orthorhombic-like atomic packing at low temperature region in liquid breaks up during heating and displays low-coordinated disordered polyhedrons at high temperature region.

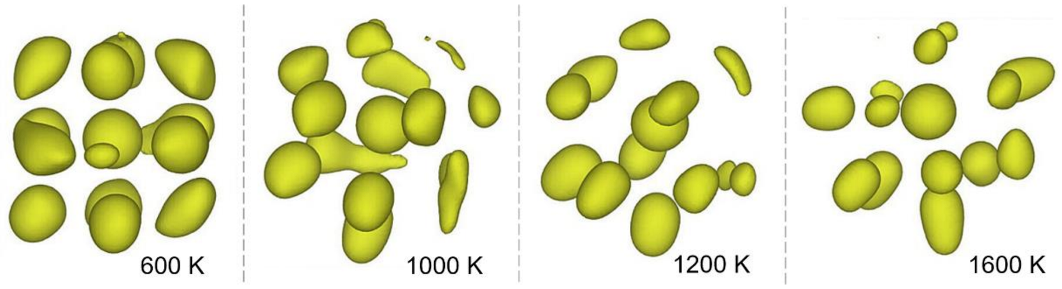

Fig. 1.3. Atomistic morphology evolution in liquid Ga [37].

Tanaka [16] thought an L-LST can be predicated on two order parameters, i.e., density and bond ordering. The density order parameter maximizes the density (or packing) to lower the attractive interaction energy, which ultimately leads to long-range ordering or crystallization. The bond order parameter describes the packing of locally favored structures, which captures both SRO and MRO. At high temperatures, the liquid is in an excited state. The liquid transforms into an energetically more favorable state with higher density as the temperature decreases. Iwashita et al. [40] studied the liquid state of various metallic systems through classical and AIMD simulations. The results suggest that elementary excitations in high temperature metallic liquids are local configurational changes in the atomic connectivity network. The L-LST is attributed to the competition between the configurational excitations and phonons. However, a rigorous experimental observation of L-LST is still lacking because of the harsh conditions in experiments, including, (i) high Temperature (and often high pressure); and/or (ii) deep in the undercooling regime where crystallization is prone to occur. As a result, the mechanism of L-LST remains still inconclusive to date.

1.3 Methods to characterize the liquid-liquid structure transition

So far, a lot of efforts have been made to study the liquid metal and much experimental and numerical evidence has been accumulated for the existence of the L-LST in metallic liquids. The experimental methods on L-LST research mainly focus on detecting the liquid structure and they can be sorted into direct measurement and indirect measurement roughly. The direct methods could be classified into diffraction methods and absorption methods. The main mechanism of diffraction method on L-LST research is the diffraction of neutron, electron or X-ray. The absorption methods are based on the radiation scattering. Indirect methods measure the physical parameters that have close relationship with the liquid structure.

1.3.1 Experimental methods

1.3.1.1 Direct methods to study the L-LST

Direct methods are effective and accurate ways to analyze liquid structure, which offer the average and one-dimensional structural information of the liquid state directly. According to the mechanism they utilized, the direct methods can be classified into diffraction methods and absorption methods. Radial distribution function *g(r)*, mean nearest neighbor distance r_1, coordination number N_1 of the liquid metal could be obtained indirectly by diffraction methods or absorption methods, which show the structure of the liquid state accurately.

Common diffraction methods include X-ray diffraction, electron diffraction and neutron diffraction which are based on the diffraction of X-ray, electron and neutron respectively [41]. Neutron scattering lengths mainly depend on nuclear mass, and X-ray scattering lengths dependent on the number of electrons, the two techniques provide complementary information for a polyatomic liquid or glass [42]. Besides, neutron is electro-neutral but it has magnet moment, which leads to deep penetration and magnetic diffraction when it is utilized on magnetic materials. Up to now, to investigate the atomic scale structure of metallic liquid, the most frequently used X-ray diffraction methods are energy dispersive X-ray diffraction (EDXD) [43, 44], high energy synchrotron X-ray diffraction (HESXRD) [1, 37], small-angle X-ray scattering (SAXS) [45], wide-angle X-ray scattering (WAXS) [45], etc.

Compared with the usual diffraction methods, X-ray absorption fine structure (XAFS) [46], an absorption method, has the advantage of providing information in respect of the local atomic arrangement around a specific atomic species. In contrast to this, a diffraction experiment gives information of atomic arrangements around a reference atom which represents an average of all atomic species present in the specimen [47]. Furthermore, X-ray absorption phenomenon depends on the effect of SRO, so whether the atoms in the system are periodic or not XAFS is always an effective method.

High temperature nuclear magnetic resonance (NMR) [35] can also be used to detect structure changes in metallic melt, however, due to its difficulty, there is just quite few results about metallic melts up to now.

1.3.1.2 Indirect methods to study the L-LST

Indirect methods are widely applied due to the limit and the high cost of direct methods. Physical parameters that are sensitive to the liquid structure are selected. Physical parameters such as density [48], heat capacity [49], internal friction [50], magnetic susceptibility [51], resistivity [52], specific volume [53], viscosity [54], etc., can be chosen and the structure of instruments is relatively simple and effective.

Compared to other physical parameters and the derived methods, the magnetic susceptibility and its corresponding method [55] have certain advantages. On the one hand, by in-situ measuring the temperature and magnetization, the melting behavior, the solidification process and other possible transformations can be observed; see Fig. 1.4. On the other hand, with the help of glass fluxing technique, the magnetization of the liquid alloy can be in-situ measured in a very wide temperature range from hundreds of degrees above the melting point (overheated state) to hundreds of degrees below the melting point (supercooled state). As a consequence, this method can be used to study the possible L-LST either in the overheated state or in the supercooled state.

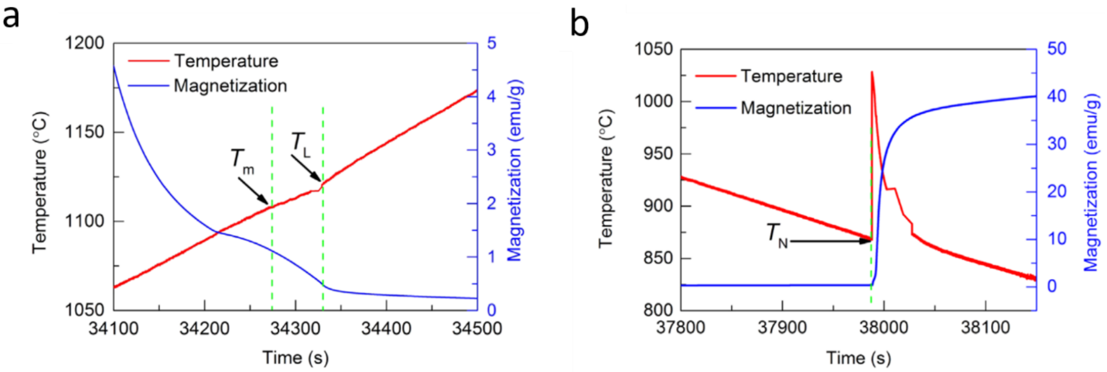

Fig. 1.4. The temperature and magnetization as a function of time of $Co_{76}Sn_{24}$ alloy, showing the range around (a) the melting and liquids point during heating and (b) the nucleation point during

cooling measured in 1 T magnetic field where the field gradient is 1490 G/cm [28].

1.3.2 Simulation methods

Recently, using computer calculation to investigate the structure of liquids, especially under extreme condition such as high pressure, high temperature and deep supercoiling, which is known as 'No man's land' [56], have attracted deep interesting among the world. So far, many methods such as Monte Carlo simulations [56], reverse Monte Carlo analysis [38], phase field calculations [57], free energy methods [58], molecular dynamics simulations [59], ab initio molecular-dynamics simulations [60], first-principles calculations [61] and the combination of both methods, i.e., first-principles molecular dynamics [62] were adopted to study L-LST and had already made certain progress.

1.4 Effects of the liquid-liquid structure transition on solidification

There has been a notable trend in engineering practices that the properties and solidified microstructure of many alloys are dependent on the thermal history of their parent liquids [36]. The alteration of the solidification microstructure due to different thermal histories is thought to be ascribed to their different liquid states. Therefore, controlling the liquid states, based on the L-LSTs, has been confirmed to be effective in regulating the subsequent solidification processes, microstructures and properties.

1.4.1 Nucleation

Nucleation is an activated process in which the system has to overcome a free energy barrier in order for a first-order phase transition between the metastable and the stable phases to take place

[2]. The ability to control nucleation lies at the heart of the development of novel microstructures for advanced materials applications [63]. In metallic liquids, the ordering structure can be the precursor of nuclei, thus any structure transitions inside the metallic melt can make the nucleation process different.

Yu et al. [36] studied the solidification behaviors of the $Bi_2Te_{2.7}Se_{0.3}$ alloy with different liquid states. As shown in Fig. 1.5, the sample that experienced L-LST shows that the nucleation and growth undercooling degrees are significantly enlarged and the solidification time is shortened. The atomic bonds of crystals are only partly broken on melting. The SROs similar to the corresponding solid crystal still remain in overheated melt within a certain temperature range. These SROs as the intrinsic growth nuclei can lead to the variation of undercooling. When an alloy is melted below the L-LST temperature, the SROs can easily become the core of nucleation, which promote the nucleation during cooling. At a temperature higher than that of the L-LST, these SROs break or dissolve to generate new atomic clusters. The SROs then become more uniform and disordered, changing the melt state. A melt with smaller and disorder clusters is difficult to nucleate. Therefore, a greater undercooling is needed for nucleating [64].

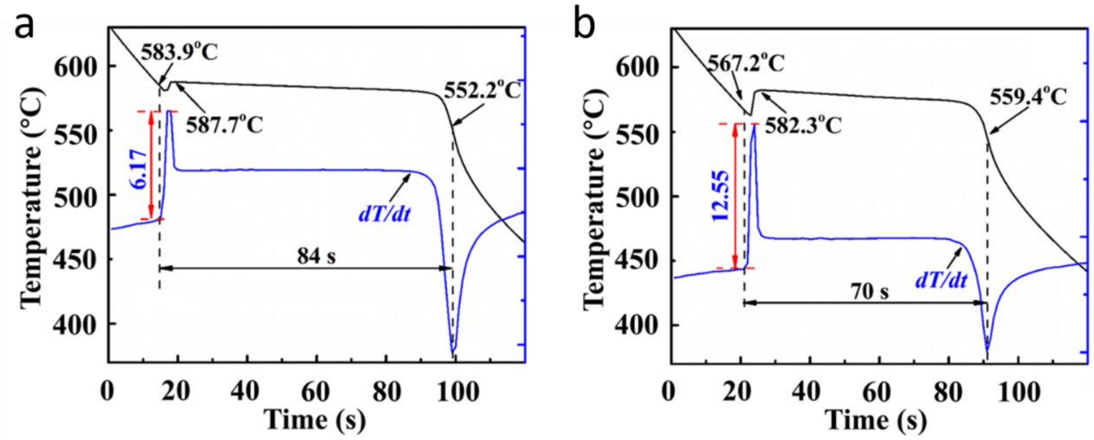

Fig. 1.5. Cooling curves for $Bi_2Te_{2.7}Se_{0.3}$ liquid alloy. (a) Sample without the process of the L-LST

and (b) sample experienced the L-LST [36]. The temperature indicated by the first arrow from the left of each picture is the nucleation temperature, T_N. The second arrow indicates the recalescence temperature, T_G. The red double sided arrow shows the height of the first peak for dT/dt curve, Δh. The black double sided arrow shows the solidification time.

Wang et al. [18] evidenced an L-LST in the overheated $Co_{83}B_{17}$ alloy, and they found the L-LST has strong influence on the nucleation temperature of undercooled melt. The average stable undercooling increased from 80 K to 180 K when the melt undergoes L-LST, as shown in Fig. 1.6. The same effect is also observed in $Co_{76}Sn_{24}$ alloy [19] and the other two compositions of Co-B alloys [65].

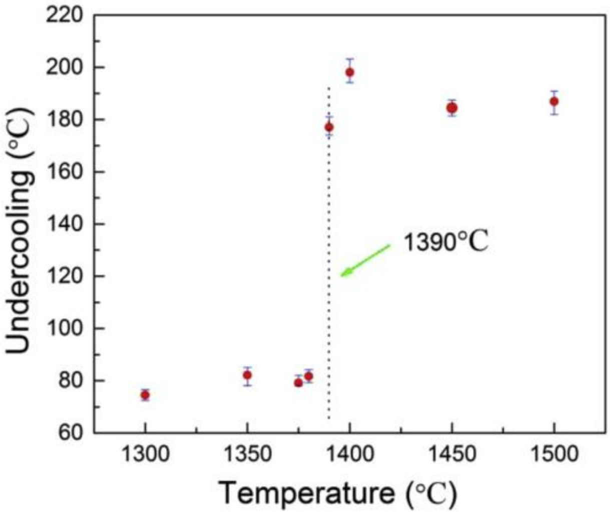

Fig. 1.6. The mean undercooling of the $Co_{83}B_{17}$ alloy processed at different overheating temperature. When the melt is overheated above L-LST temperature (1390 ℃), the melt can obtain a much higher undercooling before nucleation [18].

The survived tiny crystals in the liquid acts as a template, catalyzing the nucleation. To reduce the nucleation barrier, the new phase with the structure close to the local structure in the liquid tend to nucleate first, even it is metastable. Kelton et al. [9] demonstrated an enhanced icosahedral SRO with undercooling in Ti-Zr-Ni liquids that form icosahedral quasicrystals, decreasing the barrier for the nucleation of the metastable *i* phase, even over the formation of stable polytetrahedral crystal phases. The first recalescence is due to the formation of an icosahedral quasicrystal (*i* phase) and the metastable *i* phase transforms after 2-3 s to the C14 Laves phase (the second recalescence); see Fig. 1.7.

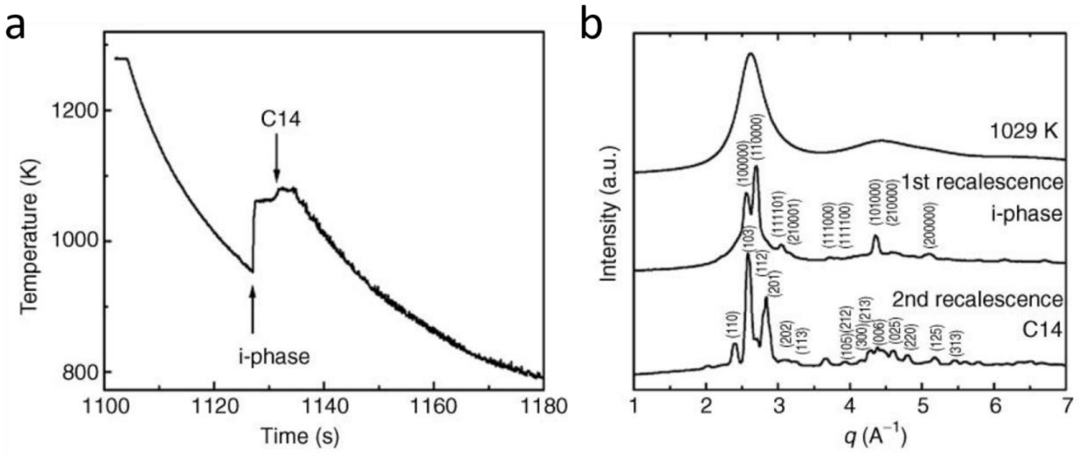

Fig. 1.7. (a) Cooling curves for an electrostatically levitated 2.5 mm droplet of $Ti_{39.5}Zr_{39.5}Ni_{21}$ with temperature as a function of time, showing two recalescence events. (b) X-ray diffraction pattern as a function of momentum transfer q for the undercooled liquid Ti-Zr-Ni alloy at 1029 K and during the first and the second recalescence [9].

1.4.2 Crystallization products and microstructure

The L-LST has a significant impact on the solidification structures and there are growing experimental supports for the feasibility of changing the liquid state, based on the LLST, to modify the solidification microstructures. Fig. 1.8 shows the solidification microstructures of Bi-Sb10 wt% alloy [68]. The primary phase of sample solidifying from the melt without L-LST (Fig. 1.8a) is obviously coarse and the morphology is irregular while the primary phase of sample solidifying from the melt that experienced L-LST is fine and uniform (Fig. 1.8b). As we mentioned above, the atomic bonds of crystals are only partly broken on melting and the SROs similar to the corresponding solid crystal remain in liquids within a certain temperature range. These SROs are beneficial to become the nuclei to promote nucleation and growth of crystal during cooling, owing to the convenient structure. Besides, it is worth mentioning that the liquid is inhomogeneous since the SROs are different in shape and size. Therefore, the microstructure morphology is irregular and coarse when the alloy is melted below the L-LST temperature. As the temperature increasing, atoms obtain more and more kinetic energy. Up to the L-LST temperature, the energy is large enough to overcome the energy barrier and the SROs disintegrate and break up, resulting in a relatively homogeneous and disorder liquid. This kind of liquid is difficult to meet the need of nucleation and thus a greater undercooling degree is needed. According to the classical nucleation theory, the density of critical nucleus site and nucleation rate will be higher with a greater undercooling. Furthermore, the growth rate is slower due to the lower atom diffusion rate resulting from the great undercooling. Therefore, the microstructure morphology is fine and uniform when the alloy is melted above the L-LST temperature.

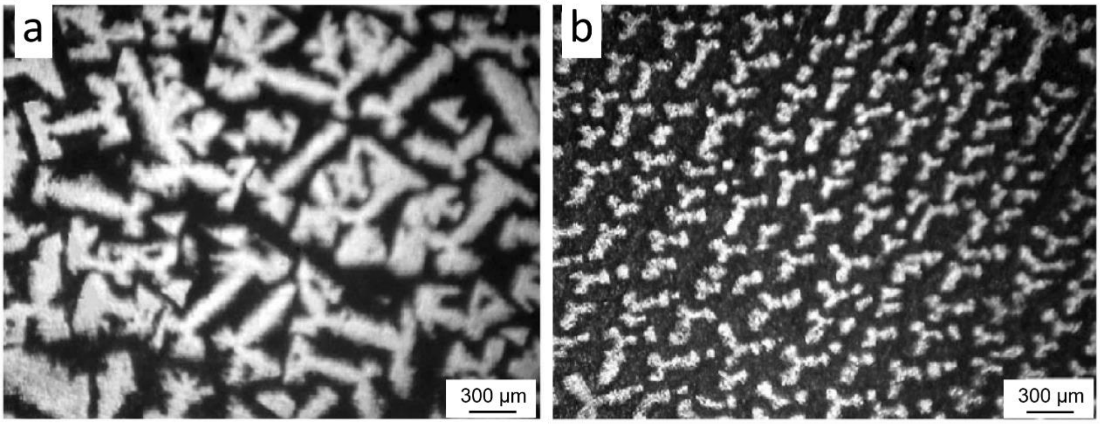

Fig. 1.8. Solidification microstructures of Bi-Sb10 wt% alloy as observed by optical microscopy. (a) Sample without the process of the L-LST and (b) sample experienced the L-LST [68].

The grain refining effect caused by L-LST is evidenced in several alloys. The same effect can also been applicable for eutectic alloys. Fig. 1.9 shows the microstructures of the $Sn_{57}Bi_{43}$ eutectic alloy solidified from different liquid state [69]. The microstructure of the sample experienced the L-LST has a degree of refinement and the lamellar spacing of eutectic structures decreases significantly. Similar refinement phenomenon is observed in the $Sn_{75}Bi_{25}$ hypoeutectic alloy [70]. The lamellar spacing of eutectic structures decreased from 7.6 to 2.1 μm after the L-LST; see Fig. 1.10.

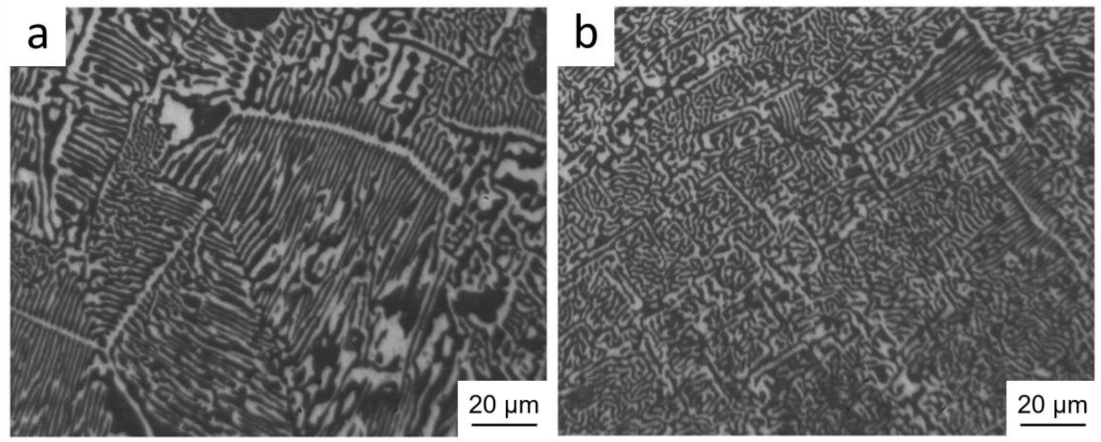

Fig. 1.9. Solidification microstructures of the $Sn_{57}Bi_{43}$ eutectic alloy. (a) Sample without the process of the L-LST and (b) sample experienced the L-LST [69].

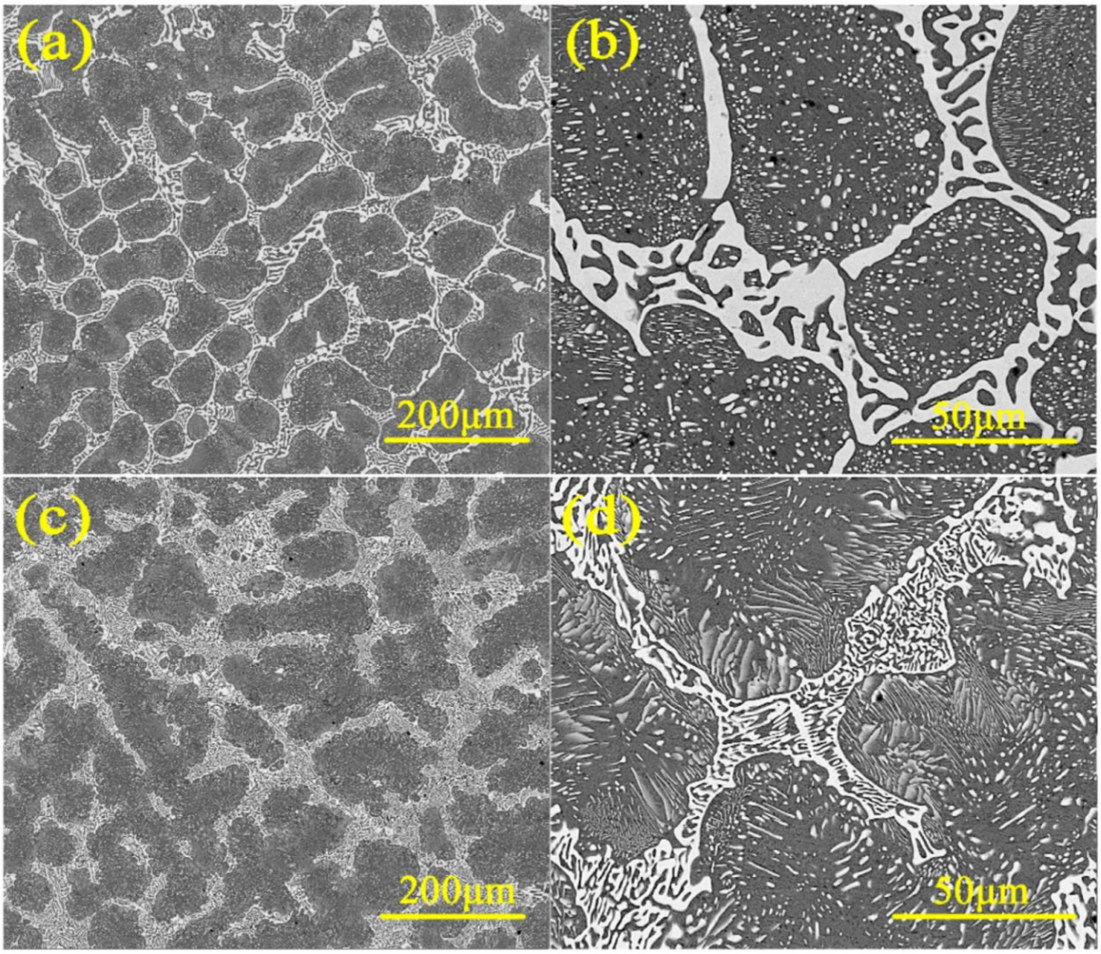

Fig. 1.10. Solidification microstructures of the $Sn_{75}Bi_{25}$ hypoeutectic alloy. (a) and (b) Sample without the process of the L-LST; (c) and (d) sample experienced the L-LST [70].

There are many favored atomic pairs corresponding to different SRO, since the atoms of constituent element are not distributed uniformly in metallic liquid. The SRO composed of favored atomic pair acts as preexistent nuclei, which can directly grow and form corresponding nano-crystalline phases. The crystallization production is related to the configuration of SRO and the number of different SROs. As mentioned above, the configuration of SRO and the number of different SROs evolve with the increasing temperature, especially at the L-LST temperature. Therefore, the crystallization products also can be altered by the L-LST. The DSC curves of three $Ti_{40}Zr_{25}Ni_{8}Cu_{9}Be_{18}$ metallic glass rods prepared at different liquid temperature are shown in Fig.

1.11a [71]. An endothermic signal peak (indicated by the green arrow) is only observed in the curve of Rod1, which is supposed to be owing to the crystallization products precipitated during first crystallization are different. For Rod1, icosahedral phase precipitates during first crystallization and this metastable icosahedral phase transforms to the stable Laves phase at high temperature through the endothermic reaction. However, for Rod2 and Rod3, stable phase rather than metastable icosahedral phase precipitates directly from amorphous matrix. The XRD patterns of Rod1 and Rod2 after isothermal annealing confirm the hypothesis; see Figs. 1.11b and 1.11c. For Rod1, some new peaks appear after first crystallization, which is typical diffraction pattern of icosahedral phase. However, there is no typical diffraction pattern of icosahedral phase in XRD pattern after first crystallization for Rod2. The difference in crystallization products indicate that Rod1 and Rod2 possess different initial microstructures, i.e., different liquid states. It can be inferred that there is a temperature induced L-LST between Rod1 (1123 K) and Rod2 (1573 K), which has a significant influence on the crystallization products.

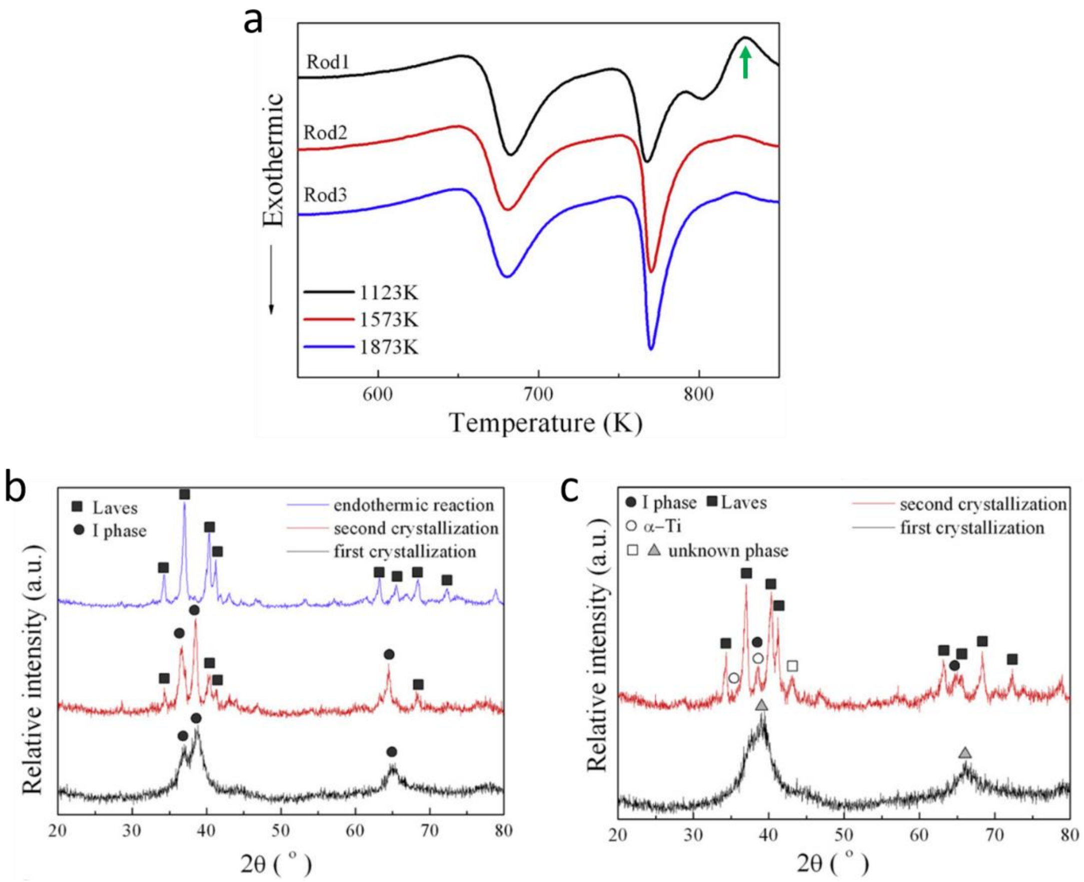

Fig. 1.11. (a) DSC curves of three $Ti_{40}Zr_{25}Ni_8Cu_9Be_{18}$ metallic glass rods prepared at different liquid temperatures, (b) and (c) XRD patterns of rod1 and rod2 after isothermal annealing [71].

1.4.3 Properties

Since the L-LST has a big influence on the nucleation, crystallization products and microstructure as we mentioned above, it is reasonable to conjecture that these alterations might lead to an enhancement of the properties of commercial-scale ingots, thus benefitting applications.

Wettability. Li et al. [12] studied the effect of L-LST on wettability of Sn-0.7Cu solder, and they found the wettability was improved when the sample solidified from the melt experienced the L-LST; see Fig. 1.12. It can be found that the overall spreading area in Fig. 1.12b is larger than that of Fig. 1.12a. The melt which experienced L-LST is more disordered and homogeneous than the melt did not experience, so atoms in the former state are more active as compared to that of the latter.

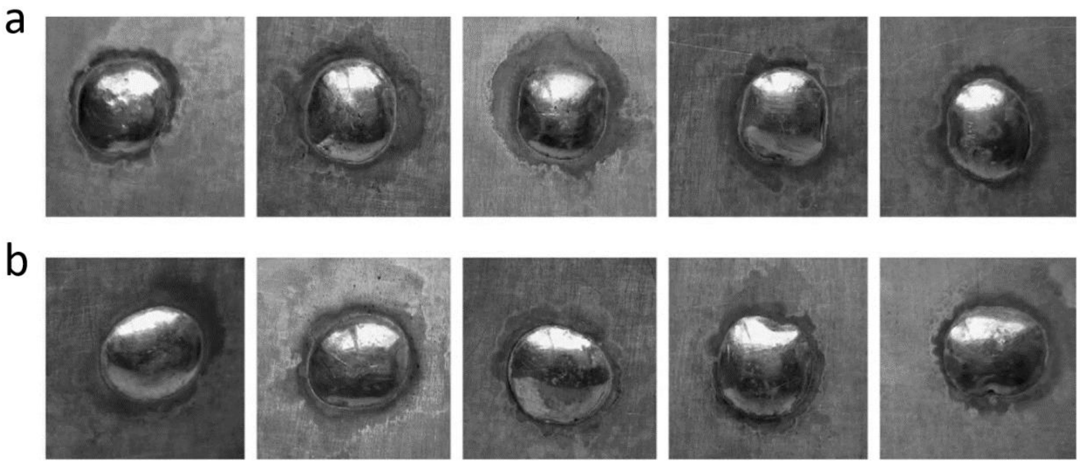

Fig. 1.12. Spreadability testing of the solders. (a) Sample without the process of the L-LST and (b) sample experienced the L-LST [12].

Corrosion resistance. With increasing melt temperature, the corrosion potential (E_{corr}) of $Al_{97}La_3$ alloy ribbon increases and the corrosion current density (I_{corr}) decreases; see Fig. 1.13 [5]. With the increase of overheating temperature, the melt structure becomes more uniform and random, and the atomic cluster size becomes small, which is retained in rapidly solidified alloys. Therefore, the corrosion resistance is improved with the more uniform structure prepared by melt heat treatment.

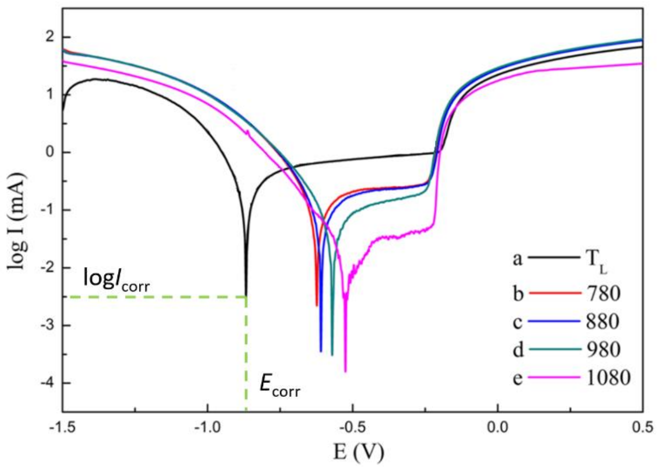

Fig. 1.13. Potentiodynamic polarization curves of $Al_{97}La_3$ alloy prepared at different liquid temperatures [5].

Mechanical Properties. Fig. 1.14 presents the compressive engineering strain-stress curve for the Rod1 and Rod2 [71]. As described earlier in Fig. 1.11, Rod1 is prepared without the process of L-LST and Rod2 experienced the L-LST. As shown in Fig. 1.14, the plasticity of Rod1 is higher than that of Rod2, although they exhibit same elastic limit about 2.3% and yield strength near 1900 MPa. Many other mechanical properties are also found can be affected by L-LST, such as the hardness [36], tensile properties [72].

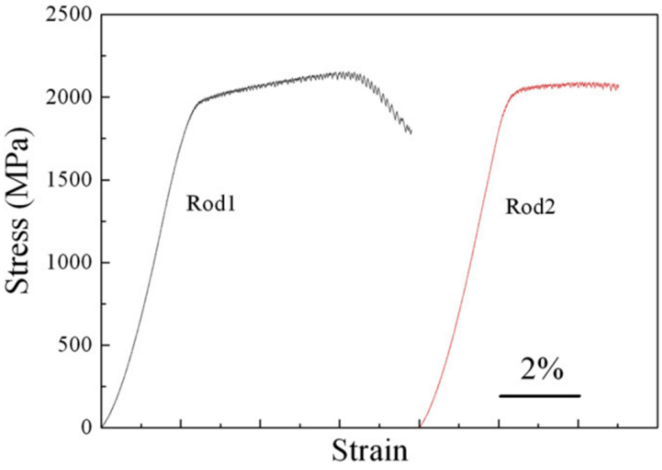

Fig. 14. Compressive engineering strain-stress curve for Rod1 and Rod2 [71].

Magnetic property. Hu et al. [73] studied the influence of melt temperature on the magnetic properties of $(Fe_{71.2}B_{24}Y_{4.8})_{96}Nb_4$ bulk metallic glass. A stronger Invar effect with lower Curie temperature and larger spontaneous volume magnetostriction is found in the sample cast from 1623 K; see Fig. 1.15. This abnormality, which cannot be eliminated by annealing, is attributed by the hyperfine field distribution. This special local structure is inherited from the melt, which has a L-LST. Through a slow-cooling process, the melt in the L-LST is frozen to a crystalline structure contained Y_2Fe_{17} phase with a high intensity signal.

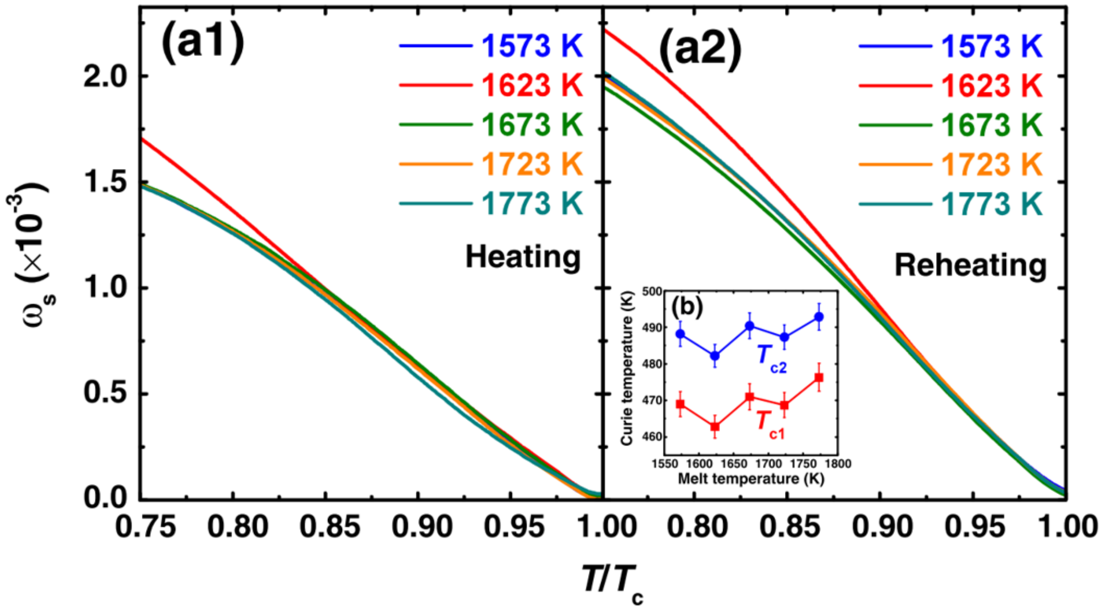

Fig. 1.15. (a1) and (a2) Spontaneous volume magnetostriction (ω_s) as a function of the reduced Curie temperature (T/T_c). (b) two Curie temperatures determined in heating and reheating process [73].

1.5 Summary

In this chapter, the mechanism and experimental research of L-LST in metallic liquid is summarized. When heated slightly above *liquidus*, specific alloy melts are not homogeneous and stable as traditionally supposed. Instead, there are numerous SORs in the liquid and they will remain in a certain range of temperature. These inherent SORs are unstable relative to free atoms and change discontinuously with the increasing temperature, resulting in L-LST. The classification of L-LST can be based on the inducing condition, the reversibility of the transition process and the thermodynamic property of the transition.

Experimental methods on L-LST can be classified into direct methods and indirect methods. A comparison between them has been made and can be summarized as follows:

- Direct methods can be classified into diffraction methods and absorption methods. Both of them are effective and accurate ways to clarify the liquid structure, which offer the statistical structural information of the liquid state. However, these methods require high cost, special operative technique.

- Indirect methods show L-LST by detecting the abnormal change of the specific physical parameters, which is sensitive to the liquid structure. Although they cannot offer the direct information of the melt, indirect methods can be easily applied under special conditions and they are also sensitive and accurate.

Controlling the liquid states, based on the L-LSTs, has been confirmed to be effective in regulating the subsequent solidification processes, microstructures and properties. It provides a promising approach to manipulate the materials with desired microstructure and outstanding properties, even when only a simple solidification process is performed.

At the future stage, the mechanism of L-LST needs to be further understood. More adequate models of liquid structure, especially for those systems with L-LST, are essential for the simulation and experimental research. Moreover, the relationship between the L-LST and the abnormal change of physical parameters requires to be clarified.

1.6 Résumé

Dans ce chapitre, les mécanismes et les recherches expérimentales sur les transitions structurales liquide-liquide dans un liquide métallique sont résumés. Lorsqu'ils sont chauffés légèrement au-dessus du liquidus, certains alliages fondus ne sont pas homogènes et stables comme on le suppose traditionnellement. Au lieu de cela, il existe dans le liquide de nombreux ordres à courte distance qui subsisteront dans une certaine plage de température. Ces ordres à courte distance intrinsèques sont instables par rapport à des atomes libres et changent de façon discontinue avec l'augmentation de la température, ce qui entraîne des transitions structurales liquide-liquide. La classification des transitions structurales liquide-liquide peut être basée sur les conditions de transformation, la réversibilité du processus de transition et les propriétés thermodynamiques de la transition.

Les méthodes expérimentales sur les transitions structurales liquide-liquide peuvent être classées en méthodes directes et méthodes indirectes. Une comparaison entre elles a été faite et peut être résumée comme suit :

- Les méthodes directes peuvent être classées en méthodes de diffraction et méthodes d'absorption. Les deux sont des moyens efficaces et précis pour préciser la structure du liquide, et offrent une information structurelle statistique de l'état liquide. Cependant, ces méthodes nécessitent une technique opératoire spéciale et coûteuse.
- Les méthodes indirectes montrent les transitions structurales liquide-liquide en détectant le changement anormal de paramètres physiques spécifiques, qui sont sensibles à la structure du liquide. Bien qu'elles ne puissent pas offrir directement une information sur le métal fondu, les méthodes indirectes peuvent être facilement appliquées dans des conditions spécifiques et elles sont également sensibles et précises.

Il a été confirmé que le contrôle de l'état liquide, basé sur les transitions structurales liquide-liquide, est efficace pour réguler les processus de solidification, les microstructures et les propriétés résultantes. Il fournit une approche prometteuse pour manipuler les matériaux avec la microstructure désirée et des propriétés exceptionnelles, même lorsqu'un simple processus de solidification est effectué.

Pour la suite, il faudra mieux comprendre le mécanisme des transitions structurales liquide-liquide. Des modèles plus adéquats de la structure des liquides, en particulier pour les systèmes avec des transitions structurales liquide-liquide, sont essentiels pour la simulation et la recherche expérimentale. De plus, la relation entre les transitions structurales liquide-liquide et les anomalies de changement de paramètres physiques doit être clarifiée.

Chapter 2 Materials, experimental details

2.1 Materials preparation

Co based alloys are the most promising candidates to be undercooled below their Curie temperature due to the small difference between *liquidus* and Curie temperature. The material used in the present work is Co-B binary alloys. The phase diagram is shown in Fig. 2.1. Three near eutectic point composition, i.e., hypereutectic Co-20at.%B, eutectic Co-18.5at.%B and hypoeutectic Co-17at.%B are chosen for investigation. The Co-B master alloys, with a mass of 25 g, were prepared from high purity (4 N) elements by arc-melting an argon atmosphere in a water-cooled copper crucible with a nonconsumable tungsten electrode and a titanium getter. Prior to melting, the surfaces of Cobalt blocks were cleaned mechanically to grind off the surface oxide. The ingots were melted for five times to ensure composition homogeneity. The final mass loss was found to be within 0.3wt.%.

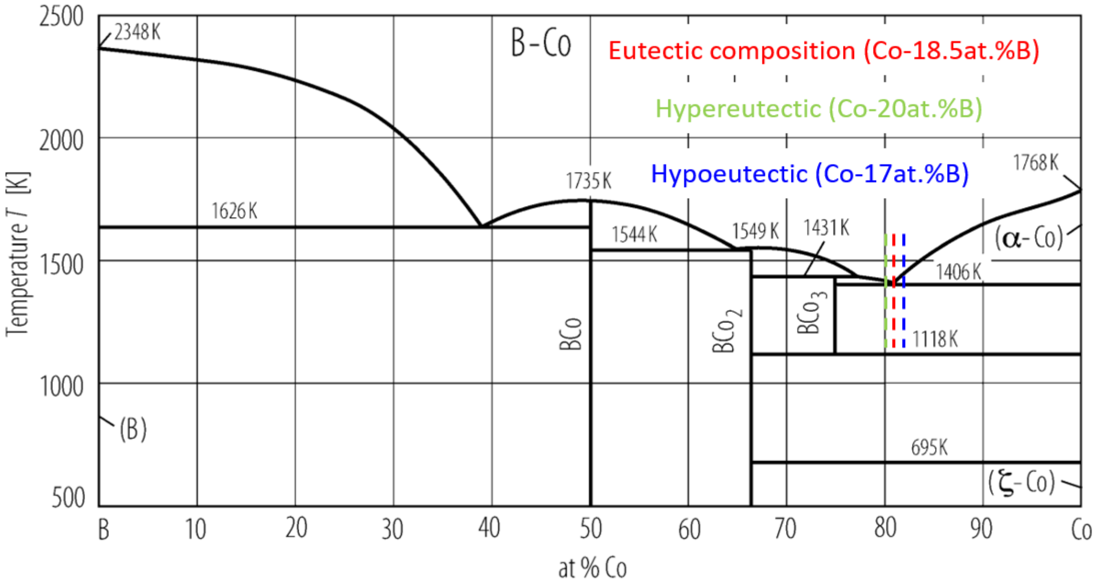

Fig. 2.1. Phase diagram of Co-B binary alloys [74].

2.2 Original microstructure and phase constituent of as-cast alloys

The master alloys were cross-sectioned and polished for structural observation using scanning electron microscope (SEM, TESCAN VEGA3). The phases therein were identified by X-ray diffraction (XRD, DX-2700) utilizing Cu-Kα radiation. The working conditions were 40 kV and 30 mA for the X-ray tube and the scanning rate was set to be 0.02 °/s. Fig. 2.2 shows the microstructures of the as-cast hypereutectic Co-20at.%B, eutectic Co-18.5at.%B and hypoeutectic Co-17at.%B alloys. For the hypereutectic Co-20at.%B alloy, the primary Co_3B dendrite was solidified firstly and then the remaining liquid was transformed into lamellar eutectics: α-Co + Co_3B (see Fig. 2.2a). For the eutectic Co-18.5at.%B alloy, the microstructure is lamellar eutectics without any visible primary phases (see Fig. 2.2b). For the hypoeutectic Co-17at.%B alloy, primary solidification of α-Co dendrite is followed by the eutectic reaction $l \rightarrow \alpha$-Co + Co_3B (see Fig. 2.2c). Such a result for the microstructures is consistent with the Co-B phase diagram [74]. It should be pointed out that α-Co after solidification can be transformed partly into ε-Co by a solid-state transformation as shown in the XRD patterns (Fig. 2.3), according to which the microstructure should be consisted of α-Co, Co_3B and ε-Co. Although the crystal structures of α-Co (BCC) and ε-Co (HCP) are different, they cannot be distinguished by the contrast in SEM.

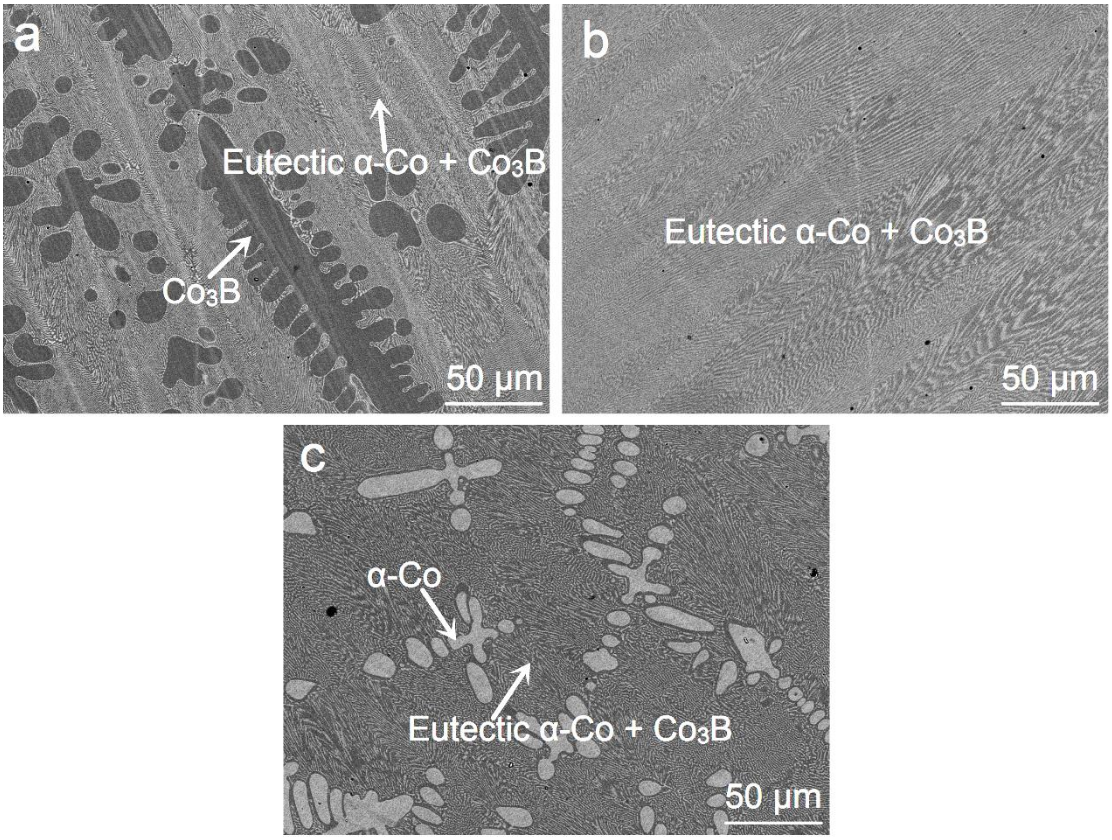

Fig. 2.2. Solidification microstructure of the as-cast (a) hypereutectic Co-20at.%B alloy, (b) eutectic Co-18.5at.%B alloy and (c) hypoeutectic Co-17at.%B alloy.

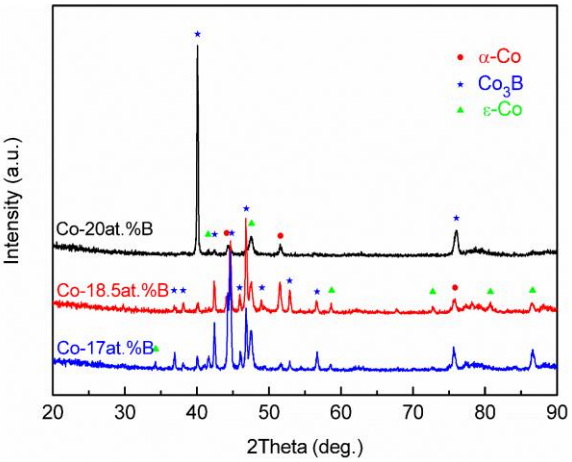

Fig. 2.3. XRD patterns of as solidified Co-B eutectic alloys.

2.3 Experimental apparatus

2.3.1 Overheating dependent undercooling

The undercooling experiments were carried out in an induction furnace. Samples, masses in about 2 g prepared by cutting the master ingots, were placed in quartz crucibles with boron oxide flux, then melted and cyclically superheated and undercooled. The glass slag, B_2O_3, was dehydrated at 800 ℃ for 6 h in advance. The alloy was heated up to a series of overheating temperatures and held therein for 5 min during every thermal cycle. A two color infrared pyrometer with ±5 K accuracy and 10 ms response time was used to in-situ measure the thermal history of the samples. The schematic diagram of the experimental apparatus is shown in Fig. 2.4.

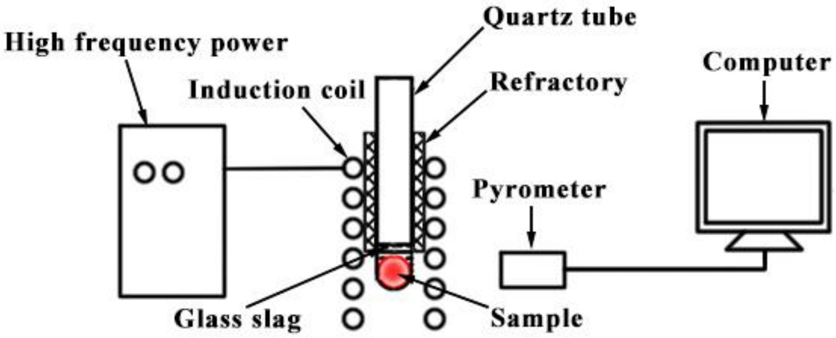

Fig. 2.4. Schematic diagram of the experimental apparatus used to study the effect of overheating on the undercooling behavior.

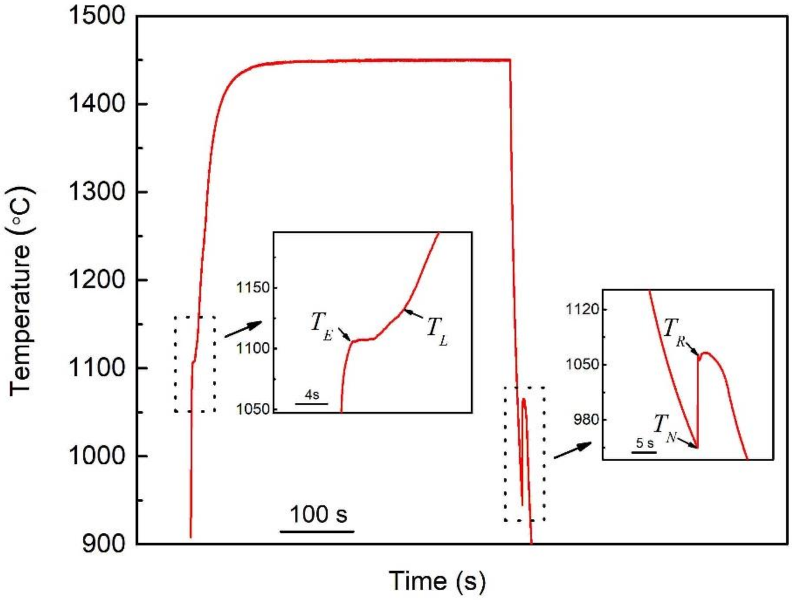

Fig. 2.5. Typical temperature profile as measured by pyrometer during heating, melting, overheating and solidification with recalescense after nucleation. The enlarged figures show the melting and

nucleation points.

Fig. 2.5 shows the measured typical temperature-time profiles of the undercooled hypoeutectic Co-17at.%B alloy. The melting point (same as the eutectic point, T_E), the *liquidus* temperature (T_L), the overheating temperature, the nucleation temperature (T_N) and the recalescense temperature (T_R) are marked. Undercooling here is defined as the difference between the nucleation temperature and the *liquidus* temperature.

2.3.1 Experimental platform for solidification and in-situ magnetization measurement

With the recent development of superconducting technology, the application of cryogen-free superconducting magnet has greatly promoted the application of magnetic fields in advanced materials processing in the research of fundamental magneto science. The application of magnetic field on materials processing has been a subject of much attention since two decades, and becomes a new direction of materials science: electromagnetic processing of materials (EPM) [75]. Present research indicates that the application of magnetic field can change the thermodynamic state of phase transitions of materials and influence the phase transformation process [76]. In solid state phase transitions, heat treatment under the magnetic field can change the morphology of the microstructure [77, 78]. For crystal with magneto anisotropy, the grain can be aligned when heat treated under magnetic field, and can make bulk textured materials [79, 80]. Very recently, the solidification of materials under magnetic field has become a hot topic. The solidification process has great importance on the final properties, and the application of magnetic field in the solidification process can change the morphology, distribution, and growth velocity of the precipitated phases and obtain in-situ formed composites, gradient materials, and anisotropic materials with unique structure and excellent properties [81-86].

To build new facilities which can be used in high magnetic fields are very important for the development of magneto-science. Until now, many new platforms have been built in superconducting magnet which can be used for materials processing or characterizing phase transitions or physical parameters variations, e.g., the differential thermal analysis (DTA) facility in high magnetic fields [87], the magnetization measurement facility by Faraday balance method [88], and dilatation measurement method in high magnetic fields to in-situ observe the phase transition process [89], and the levitation apparatus using simultaneous imposition of alternating and static magnetic fields [90]. However, up to now, it is still lack of experimental facilities, which are suitable for understanding non-equilibrium solidification under strong magnetic field, even though non-equilibrium solidification is a very important research area and has many potential applications. Due to the limitation of the experimental facilities, the non-equilibrium solidification under magnetic field has been little investigated. Beaugnon and Gaucherand have succeeded in achieving large undercooling and conducting solidification of Co based alloys in high magnetic fields [80, 88]. However, up to now, there still lacks an efficient way to obtain high undercooling to conduct controlled non-equilibrium solidification experiments like that without magnetic field. Deep investigation on the magnetic properties of undercooled melt, nucleation, grain growth, and microstructure evolution from undercooled melt solidified under strong magnetic field is an essential way for underlying the mechanism of solidification of deep undercooled melt under strong magnetic field. In order to obtain very large undercooling, metals and alloys need to be heated a few hundred degrees above their melting point and held for a certain period to eliminate impurity elements and avoid heterogeneous nucleation.

Therefore, we built a furnace using SiC heating element for the undercooling platform in superconducting magnet. By tuning the position of the heater, the undercooling platform can change between homogeneous to gradient magnetic field. Incorporating a high accuracy balance for measuring the magnetic force exerted on the sample, a magnetization measurement system was built for undercooled melt.

2.3.1.1 Undercooling in high magnetic field

The present undercooling platform is installed in a helium free superconducting magnet with maximum intensity 12 T produced by Cryogenic Ltd. It takes about 15 min to obtain its maximum field strength. The magnet has a bore in 5 cm diameter and 48 cm in length. When the furnace is put in the working space, the maximum temperature zone is 20 cm from the top surface of the magnet. The diameter of the sample is smaller than 0.7 cm, thus, the field gradient caused by the sample size within the area of maximum field is relatively small while the force exerted on the sample is large enough for magnetization measurement.

In order to meet the demand for obtaining high overheating, we use a high density SiC spiral type heating element (I Squared R Element CO., INC.). The heating element with diameter 2.5 cm outside and 1.5 cm inside can be heated up to 1650 ℃. The double wall water cooled jacket is used to cool the system between the heating element and magnet. Between the water cooled jacket and SiC heater, 6 mm thick refractory wool is used for heat insulation. A direct current power supply (Sorensen DCS80-37E) is used as heating power (the maximum voltage and current used are about 60 V and 20 A, respectively). The maximum heating rate can be up to 100 ℃/min, and the maximum cooling rate is up to 150 ℃/min when the temperature is above 800 ℃. The length of the heating zone is 10 cm, and the temperature homogeneity in the maximum heating zone is less than ±3 ℃ within 2 cm heating zone, which can guarantee temperature homogeneity of the sample. The heating system is controlled by an “S type” thermal couple installed in the homogeneous heating zone below the sample crucible. A temperature controller (Eurotherm 3504) is used to automatically tune the DC power supply, and the system is controlled by Itools software installed in a PC. To ensure the linearity of the heating and cooling, 3 segments proportional-integral-derivative (PID) parameters are calibrated and used as the controlling parameter, which could control the thermal history of the sample precisely.

The temperature of the melt is measured on-line by a two-color pyrometer (ISR50-LO, IMPAC). An optic fiber head installed with the pyrometer is used to avoid the magnetic field effect on the pyrometer. Before measuring the temperature, the pyrometer is calibrated by an “S type” thermocouple and the melting point of pure metals (e.g., Co and Cu), and the emissivity slope is tuned to make sure the measured temperature is within ±2 ℃. Glass fluxing combined with cyclic overheating is used to achieve large undercooling in superconducting magnet. The sample is encapsulated in molten glass slag, and combination of cyclic heating by holding at given overheating and cooling is used to purify the molten alloys. The controlling parameters affecting the undercooling are overheating temperature, holding time, cyclic heating times, and cooling rate. There are many glasses which can be used as the purifying slag, and B_2O_3 is one of the most efficient one for obtaining high undercooling. The molten glass slag can purify the melt by reducing the heterogeneous nucleation sites inside the alloy and increase the mean undercooling. High purity SiO_2 quartz tube with a hemisphere bottom shape is used as heating crucible. By heating for several cycles with the controlling system, the melt is cooled to a given undercooling when the maximum undercooling is in a rather stable state. The schematic diagram of the system is shown in Fig. 2.6.

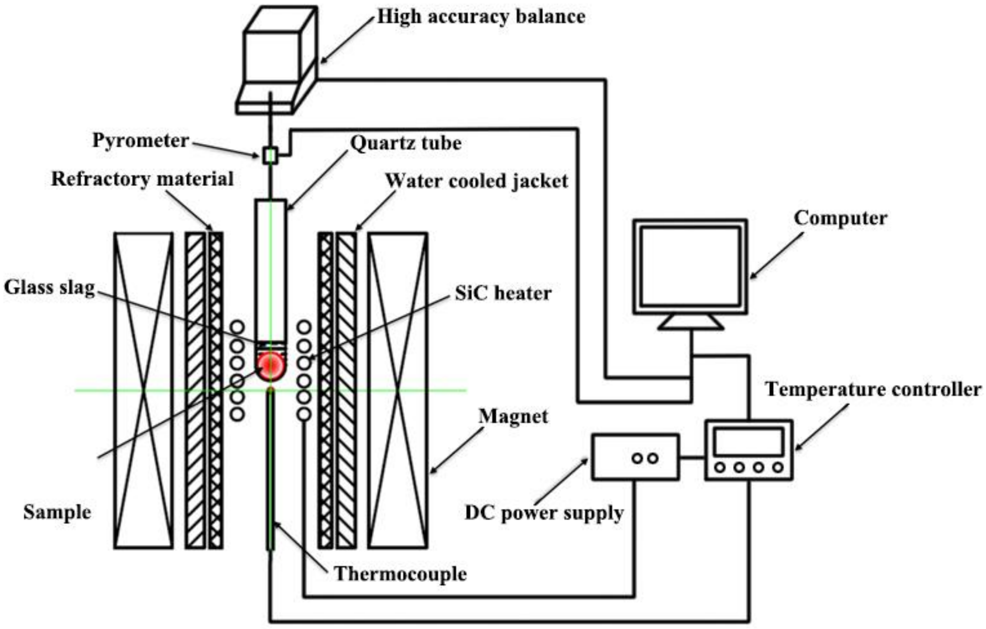

Fig. 2.6. Schematic diagram of the undercooling facility in a superconducting magnet.

Fig.2.7 shows the typical solidification curves of the undercooled $Co_{78}Sn_{22}$ alloy. Fig.2.7 is measured by pre-setting a heating program: first, heating at 40 ℃/min to 1325 ℃, holding for 10 min, and cool down at 120 ℃/min to different targeted undercooling temperatures. The undercooled melt is first rather stable (also we can call this incubation time, depending on the alloy itself and the heating history, and sometimes very long—can be up to several hours) holding for a period, and then an abrupt increase of the temperature happens, denoting the recalescence behavior (inset of Fig. 2.7). When the temperature comes back to the crystallization temperature, the DC power of the furnace is turned off, and the solidified alloy was naturally cooled down at the cooling rate around 120 ℃/min. Based on this platform, many other metals and alloys have been processed with high undercooling in high magnetic field, e.g., pure ferromagnetic Co is highly undercooled to more than 360 ℃ and a strongly magnetized liquid is observed [82], diamagnetic pure Cu is undercooled to more than 260 ℃, $Co_{79.5}Sn_{20.5}$ near eutectic can be undercooled up to 280 ℃. By presetting a heating program, solidification can be carried out in different undercoolings in different field intensities, which will be quite convenient for non-equilibrium solidification investigations.

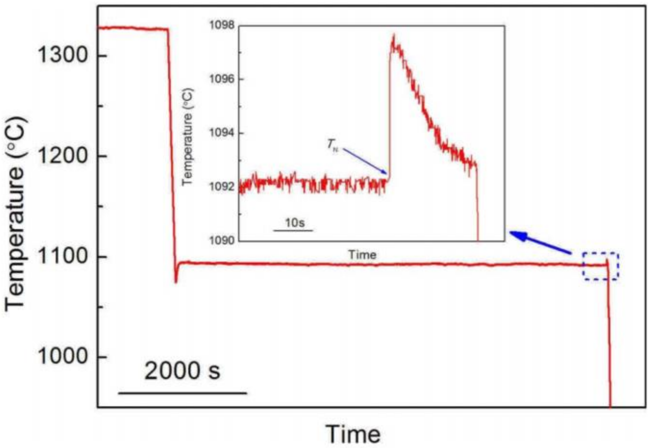

Fig. 2.7. Typical solidification traces of $Co_{78}Sn_{22}$ alloy with controlled undercooling carried out with the experimental platform. Inset shows the recalescence process of the undercooled melt. By setting the undercooling temperature, controlled solidification at certain undercooling can be obtained.

2.3.1.2 In-situ magnetization measurement in gradient magnetic field

A magnetic susceptibility measurement system under high magnetic field was built by a Faraday balance method [88, 91], and was used to investigate the magnetic properties of undercooled melt and monitor the phase transitions during controlled heating condition.

Fig. 2.8 shows the schematic diagram of the force acting on paramagnetic material ($\chi > 0$) in a magnet. The arrows in horizontal direction show the radial force from the center of the magnet bore to the magnet wall while the vertical ones show the force along the magnetic bore. In the magnet center region (marked as •), the field is larger when the sample is closer to magnet wall. Thus, a sample with a positive magnetic susceptibility will deviate from the magnet axis and finally contact with the edge and the heating element. Under this condition, due to friction and perturbance, any measurement for the magnetic force acting on the sample is not accurate. Above the maximum field region, there exists an equilibrium zone (marked as ⋆), where the magnetic force exerted on the sample in the radial direction is to the center of the magnet, which means that the sample will be automatically centered in the magnet, without any contact with the heating element. Although the field intensity in this area is much smaller than the maximum field, it is still large enough for magnetic force measurement by electronic balance. In the present equipment, the field intensity in the sample position (marked as ⋆) is about 52% of the maximum field intensity zone (marked as •).

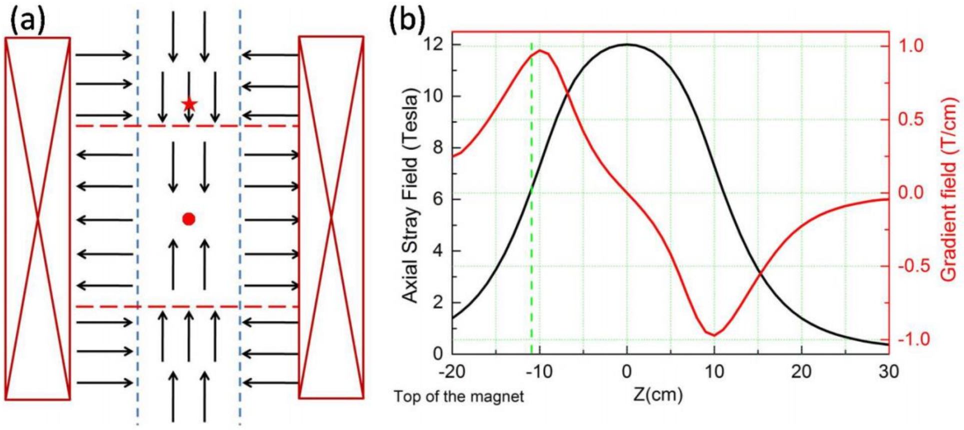

Fig. 2.8. (a) Schematic illustration of radial and axial forces applied on a ferromagnetic or paramagnetic material, in the room temperature bore of a superconducting magnet, (b) field gradient along the vertical direction of the magnet when the field intensity is 12 T, the dotted line represents the field profile at the position marked as ⋆ in (a).

The sample with positive magnetic susceptibility will undertake magnetic force downward to the vertical direction. For a freely suspended sample below the balance, the magnetic force can be calculated by

$$F_Z = mM\frac{dB}{dZ} \tag{2.1}$$

where m, M are mass (kg) and magnetization per kilogram ($\mathrm{A \cdot m^2 \cdot kg^{-1}}$), dB/dZ is the magnetic field gradient (T/m). When the magnetic field is applied, the measured mass corresponds to the addition of force exerted on the sample, sample holder, quartz crucible, glass slag, and the gravity of the whole system. Then, we can express the measured results

$$F_Z = \left(m_{measured} - m_{background}\right) g \tag{2.2}$$

where $m_{measured}$ and $m_{background}$ are the measured magnetic force on the sample and the background including the gravity of the system and magnetic force exerted on the sample holder, quartz crucible, and glass slag, respectively. g is acceleration of gravity constant in m s^{-2}. The background signal mainly corresponds to the negative contribution of diamagnetic quartz tube and sample holder. Compared with the ferromagnetic sample, the background can be neglected. However, when the alloy is in a weak paramagnetic state, e.g., high temperatures above its Curie point, accurate measurement of the background becomes very important. During the measurement, the sample is put 105 mm above the maximum field region, and the field gradient dB/dZ is calibrated by pure Ni.

The magnetization of ferromagnetic materials is very sensitive to temperature, and large error can be obtained when the temperature of the sample is not homogeneous or incorrect. Thus, to ensure the accuracy of the temperature, two factors are considered. First, tune the position of the heating element precisely. The temperature within the maximum heating zone is within ±3 ℃ in 2 cm, and the diameter of tested sample is within 6 mm, which means the temperature gradient can be controlled to be very small when the sample is put in the maximum temperature zone. Second, the heating and cooling rate used is normally below 10 ℃/min. The low rate can make sure that the temperature varies homogeneously during measurement.

Then, the measured data totally comes from the field effect, and also the background from the force exerted on the sample holder by the magnetic field is included. The background caused by the magnetic force can be measured by carrying the experiments without sample at the same heating program. Considering the difficulty in measuring temperature when there is no sample, pure diamagnetic Cu is used to determine the temperature during the scan of the background since Cu has very negligible effect on the background due to its low magnetic susceptibility. Fig. 2.9 is the turbulence of the system by measuring Cu in 1 T magnetic field. It can be seen that the background caused by magnetic field has very limited effect on the measuring results. From the measuring range, the variation of the mass is within 15 mg, which can make sure the accuracy of measurement at high temperature when the magnetic susceptibility of sample is very small. In this case, the background should be subtracted before calculation. The turbulence of the system mainly comes from the heat flow of the heating element and the magnetic force exerted on the system including the quartz tube and holding system.

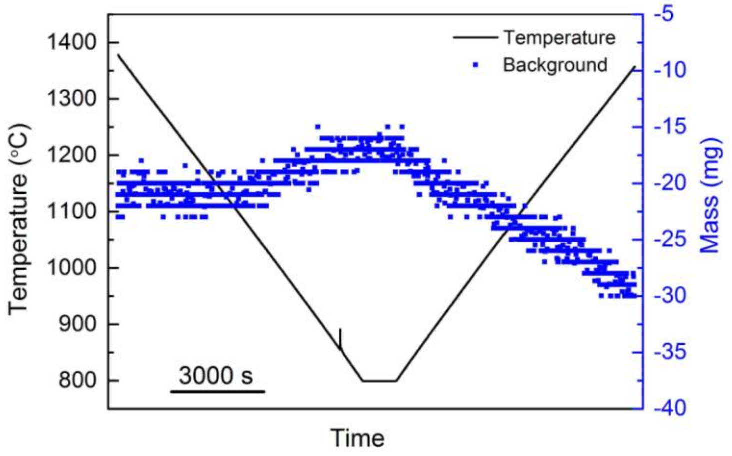

Fig. 2.9. Measured data for pure Cu with 1 T magnetic field. The blue square symbol shows the signal of the balance during heating according to the black line.

Fig. 2.10 shows the typical magnetization and temperature as a function of time curve of $Co_{76}Sn_{24}$ alloy measured at a heating rate of 10 ℃/min in 0.26 T magnetic field. During heating process, the magnetization decreases with increasing temperature and a large decrease happens when approaching the Curie point. When the temperature is above the Curie point, the alloy is in paramagnetic state, and the magnetization decreases continuously with the increasing temperature.

The deviation from the linear heating line at 1111 ℃ shows the melting of the alloy. The melting process is finished at 1135 ℃, where we can see an inflexion point. The magnetization curve shows the same trend, no obvious difference is shown at the melting point and a typical decrease point at the fully liquid temperature (shown in Fig. 2.11a). During the cooling process, the magnetization remains unchanged with the decrease temperature and no change happens at melting point: the alloy melt comes into the undercooled state. At 867 ℃, rapid temperature increase is detected (recalescence) due to the large latent heat release accumulated during deep undercooling process, where the magnetization of the undercooled liquid starts to increase faster after the solidification of the alloy, as seen in Fig. 2.11b. The magnetization of the liquid metal can be measured in a wide temperature range which can be used to in-situ characterize the structure transition inside the liquid and also the phase transition process from undercooled melt due to the magnetization variations.

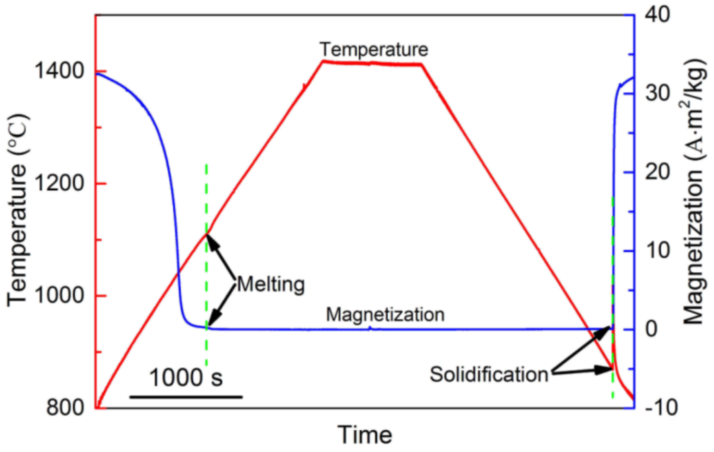

Fig. 2.10. Typical magnetization and temperature as a function of time curve of $Co_{76}Sn_{24}$ alloy measured at heating and cooling rate of 10 ℃/min. The field intensity and gradient at the sample position are 0.26 T and 0.0388 T/cm, respectively.

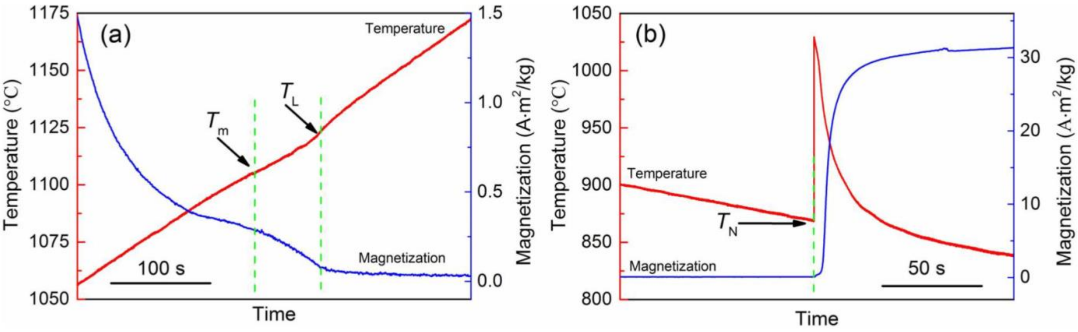

Fig. 2.11. Enlarged figure around (a) melting point and (b) recalescence range in Fig. 2.10.

2.4 Summary

In this chapter, the materials and experimental details are summarized. A home-made experimental platform for solidification of undercooled melt and synchronous measurement of magnetization under strong magnetic field is reported particularly. The facility can be used for in-situ measurement of the magnetization of the undercooled melts and to studying the non-equilibrium solidification from deeply undercooled metals and alloys in magnetic field. The key advantages of this apparatus are first, we can obtain large undercooling in high fields by glass fluxing technique in combination with cyclical superheating and supercoiling method, which is comparable to the maximum undercooled obtained by traditional method without magnetic field. Second, we can have a controlled thermal history with linear heating and cooling speed with high accuracy. Third, the temperature and magnetization measurement system are fast and on-line, which is very suitable for the investigation of both the structure transitions in the liquid in a wide temperature range (overheated and undercooled state) and the solid state phase transformations.

2.5 Résumé

Dans ce chapitre, les matériaux et les procédés expérimentaux sont résumés. En particulier, une plate-forme expérimentale réalisée au laboratoire permet de réaliser la solidification en sous refroidissement d'alliages fondus et de suivre simultanément l'évolution de la susceptibilité magnétique en champ intense. L'installation peut être utilisée pour la mesure in situ de l'aimantation des alliages liquides sous refroidis et pour l'étude de la solidification hors équilibre des métaux et alliages en sous refroidissement profond sous champ magnétique. Cet appareil a trois principaux avantages. Premièrement, il est possible d'obtenir un grand sous-refroidissement sous champ intense, par la technique de l'encapsulation vitreuse du verre en combinaison la méthode de surchauffe et sous refroidissement cycliques, qui est comparable au sous-refroidissement maximum obtenu par la méthode traditionnelle sans champ magnétique. Deuxièmement, nous pouvons appliquer un programme de température bien contrôlé avec une vitesse de chauffage et de refroidissement linéaire et une grande précision. Troisièmement, le système de mesure de la température et de l'aimantation est rapide et en temps réel, ce qui est très utile pour l'étude des transitions de structure dans le liquide dans une large gamme de température (état surchauffé et sous-refroidi) et l'étude des transformations en phase solide.

Chapter 3 Phase selection in rapid solidification of undercooled Co-B alloy

3.1 Introduction

Rapid solidification has attracted increasing attention during the past decades ascribing to its non-equilibrium effects, with which it is possible to produce the supersaturated solid-solutions [92], amorphous [71], quasi-crystals [93], metastable crystalline phases [94] and grain-refined materials [95]; these are unobtainable by near-equilibrium solidification and have important potential for functional and/or structural applications. Generally, rapid solidification can be realized by rapidly quenching [96] and bulk undercooling techniques [97]; the latter that achieves a high undercooling by excluding heterogeneous nucleation substrates often outperforms the former that increases the cooling rate of solidification. One of the superiorities is to study phase selection, a common and important phenomenon during rapid solidification that determines the solidification sequence and the final industrial applications [98-107]. Compared with the solidification by rapid transfer of heat from the melt to the environment that is limited by the cooling conditions and the volume of sample, the undercooled melts obtained thermodynamically by suppressing the onset of nucleation upon natural cooling is a better way to control phase selection and to study the controlling mechanisms.

At low undercooling, an equilibrium phase should be primarily formed, whereas at high undercooling, determination of the final phase selection pathway needs a comprehensive study of the crystalline characteristics of the competing phases [102]. Yang et al. [108] found that the stable Fe_2B phase is substituted by the metastable Fe_3B phase in the as-solidified structure as a result of a preferred nucleation of Fe_3B in the undercooled Fe-B eutectic alloy. In a Ni-38wt.%Si eutectic alloy, Lai et al. [109] found that the primary phase changes from the NiSi to the $NiSi_2$ phase due to the growth-controlled mechanism, based on in-situ observations of the recalescence processes by a high-speed camera. Based on the published literature on undercooled metallic and oxide melts. Li et al. [110] suggested that phase selection during rapid solidification can be categorized to be nucleation-controlled and growth-controlled. It is worth to note that almost all the previous studies on phase selection can be classified into two cases, i.e., one is that there is a metastable candidate to compete with the stable phase and phase selection occurs between the stable and the metastable phase [94, 105, 111] and the other is that phase selection occurs between two stable phases, e.g., for alloys at the eutectic composition [109].

A solidification microstructure selection map (SMSM), which allows a presentation of processing windows leading to specific microstructures for given alloy compositions and processing conditions, is very helpful in the selection of appropriate processing conditions [112]. One useful SMSM is so-called coupled zone, which represents the growth temperature/composition region where the eutectic grows more rapidly than do crystallizations of the α or β phase [113]. In the case of symmetrical phase diagram, i.e., non-faceting/non-faceting systems, the coupled zone will also become symmetrical. However, in the case of un-symmetrical phase diagram, i.e., non-faceting/faceting systems, the different growth characteristics of the two phases lead to a less coupled growth process at a non-isothermal interface, and therefore skewed coupled zone will formed and high growth rates may lead to the formation of α primary crystals even in the β side of the eutectic composition [114, 115]. A series of skewed coupled zone have been published for Al-Fe [116], Al-Si [117], Fe-C [118], etc.

Phase selection in rapid solidification of undercooled Co-B alloys was also studied. In the alloys around the eutectic composition, e.g., the $Co_{81.5}B_{18.5}$ alloy, Wei et al. [119, 120] found that the metastable $Co_{23}B_6$ phase forms instead of the stable Co_3B phase when the undercooling is larger than a critical undercooling of $\Delta T = 60$ K and the eutectics are consisted of $Co_{23}B_6$ and α-Co phases. In this chapter, a Co-20at.%B hypereutectic alloy was undercooled successful to ΔT=213 K. A critical undercooling of ΔT=119 K was found at which the microstructure changes from hypereutectic to hypoeutectic. Both nucleation and growth kinetics were discussed to describe phase selection, according to which competition between the two stable phases was found to be growth-controlled.

3.2 Experimental

In this chapter, the as-solidified Co-20at.%B hypoeutectic alloy was undercooled by the melt fluxing technique. A detail description of the set-up is given in 2.3.1.1 Chapter 2. Each sample was melted, superheated and solidified several times until a desired undercooling was achieved. However, a desired undercooling caused by spontaneous nucleation upon natural cooling sometimes is difficult. In such case, the controlled solidification mode of the resistance heating furnace was adopted. By setting the nucleation temperature, controlled solidification with a certain undercooling can be obtained.

The as-solidified samples were prepared following standard metallographic procedures (i.e. hot mounting in resin, grinding in the sequence from 220# to 2000# sand papers and polishing). The microstructures were observed by a VEGA II LMH SEM instrument with the back-scattered electron mode (BSE). The grain orientations were measured by SEM (TESCAN VEGA 3 LMU) with an EBSD analysis system after polishing the samples by the SiO_2 colloidal suspension in a vibratory polisher.

3.3 Transition from hypereutectic to hypoeutectic

3.3.1 Original microstructure and phase constituent

According to the phase diagram of the Co-B system [74], the Co-18.5 at%B alloy is at the equilibrium eutectic point constituting by the α-Co and β-Co_3B phases. In this chapter, the selected alloy composition is Co-20at.%B, i.e., a hypereutectic alloy. Under a near-equilibrium condition, the microstructure of the Co-20at.%B hypereutectic alloy should be composed by the primary β-Co_3B phase and α-Co+β-Co_3B eutectics. The micrograph of the master alloy used presently shows that its solidification starts from the formation of primary β-Co_3B dendrites and ends at the eutectic solidification of the remaining liquid into α-Co+β-Co_3B lamellar eutectics (Fig. 3.1a). After solidification, some of the α-Co phases undergo a solid-state phase transformation and are transformed into the ε-Co phases with a different crystal structure. The XRD patterns (Fig. 3.1b) also prove the presence of α-Co, ε-Co and β-Co_3B phases in the master alloy.

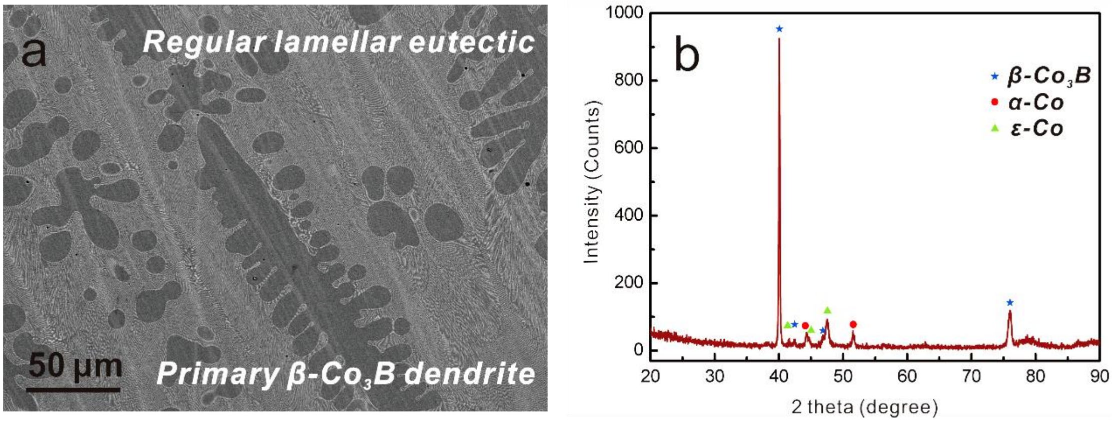

Fig. 3.1. (a) SEM image and (b) XRD patterns of the as solidified Co-20at.%B hypereutectic alloy.

3.3.2 Cooling histories

Fig. 3.2 shows the natural cooling curves of samples at various degrees of undercooling $\Delta T \approx 35$ K, $\Delta T \approx 119$ K, $\Delta T \approx 158$ K and $\Delta T \approx 213$ K. Two types of thermal behavior can be found, i.e., single and dual. The single thermal behavior refers to a single thermal event which is characterized by a sharp increase of temperature, i.e., recalescence (see Fig. 3.2d). The dual thermal behavior refers to two thermal events and can be classified into two sub-types. For the first one, the second event sets in at a higher temperature and ends at a slightly lower or much lower temperature than the initial temperature of the first event (Figs. 3.2a and c). For the second one, the second event sets in at a higher temperature and ends also at a higher temperature than the initial temperature of the first event (Fig. 3.2b). Regarding that the onset temperature of second recalescence is higher than of the first one, the undercooling ΔT in the present work is defined as the difference between the onset temperature of first recalescence and the equilibrium temperature of liquidus T_L. For an undercooling less than 213 K, e.g. ΔT≈35 K, ΔT≈119 K and ΔT≈158 K, two temperature recalescence events are available in the cooling history. The first recalescence event should be ascribed to rapid growth of primary phase and the second should correspond to eutectic solidification. However, for an undercooling larger than 213 K, there is a significant change in the recalescence behavior, i.e., only one recalescence event can be found on the cooling curve. Since two transformation processes may share the same feature in the temperature rise and complete within several microseconds [109, 121], one recalescence event does not means that only one transformation process takes place during solidification.

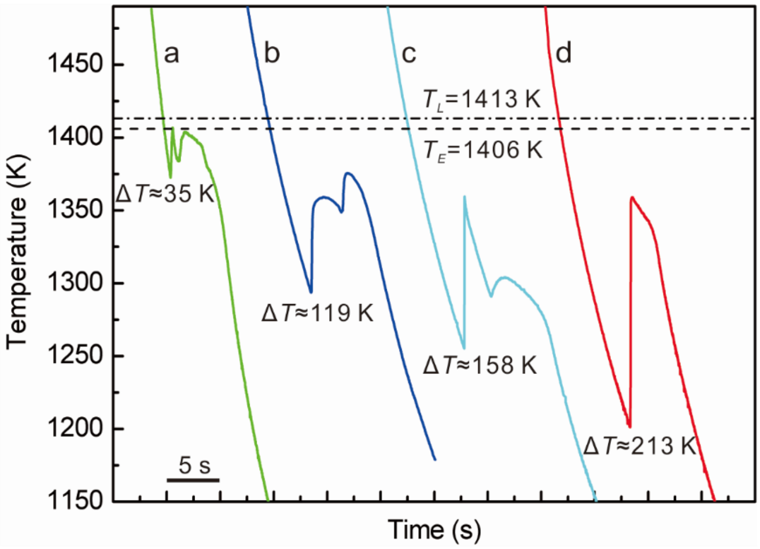

Fig. 3.2. Cooling histories of rapid solidification of the Co-20at.%B hypoeutectic alloys with different undercooling: (a) ΔT≈35 K, (b) ΔT≈119 K, (c) ΔT≈158 K and (d) ΔT≈213 K. Two dashed lines show the liquidus temperature T_L and the eutectic temperature T_E. Both of them are taken from

a thermodynamic assessment of the Co-B phase diagram [74].

Fig. 3.3 shows the cooling histories of the undercooled Co-20at.%B alloy with controlled undercooling of $\Delta T \approx 80$ K. This experiment was carried out by pre-setting a temperature program, i.e. heating firstly with a rate of 40 K min^{-1} to 1570 K, holding therein for 10 min and then cooling down at a rate of 120 K min^{-1} to 1333 K. As shown in Fig. 3.3, the undercooled melt is rather stable[1]. After holding therein for a period, an abrupt increase of the temperature happens, i.e., recalescence (inset of Fig. 3.3). When the temperature decreases to the equilibrium solidus temperature, the power of the furnace is turned off and the sample is naturally cooled down. It should be pointed out that only one nucleation and one recalescence event can be found.

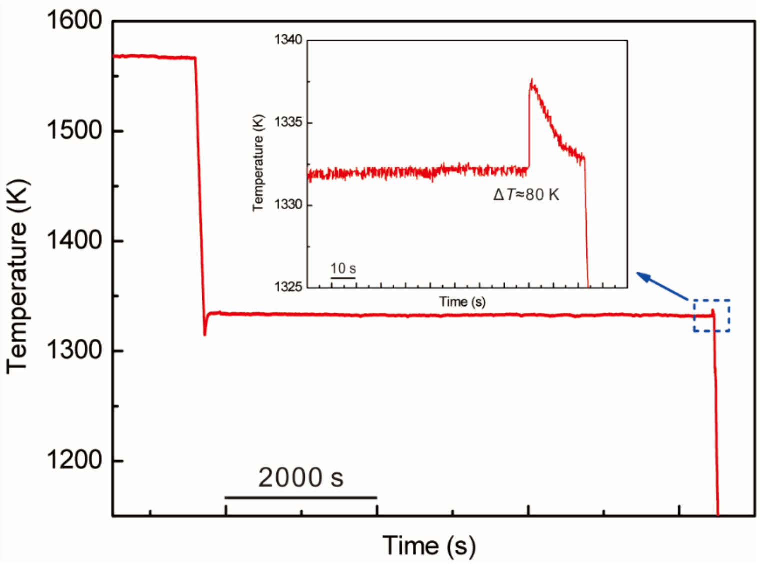

Fig. 3.3. Temperature-time profile of the Co-20at.%B hypoeutectic alloy with a controlled undercooling of $\Delta T \approx 80$ K. Inset shows the recalescence process of the undercooled melt.

3.3.3 Microstructures evolution

Fig. 3.4 shows the microstructures of spontaneous solidified samples with different undercooling. For $\Delta T \approx 35$ K, the primary directional dendritic structures of the β-Co$_3$B phase (dark block) are surrounded by the regular α-Co+β-Co$_3$B lamellar eutectics (grey region); see Fig. 3.4a. The primary β-Co$_3$B dendrites are finer than that of the master alloy (Fig. 3.1a). When ΔT increases

---

[1] Depending on the alloy itself and the heating history, the incubation time can be very long, e.g., for several hours.

to about 119K (Fig. 3.4b), the above hypereutectic microstructure is replaced by a hypoeutectic microstructure with the α-Co phase as the primary phase (light grey block), being similar to the undercooled Co-17at.%B hypoeutectic alloy [18]. Such a transition from the primary β-Co_3B phase to the α-Co phase is supported by the XRD results and the principle of atomic numbers and crystallographic contrast images [122]. Experiments using different batches of samples lead to identical results and an analysis of the overall alloy composition shows no significant deviation. Therefore it can be inferred that a large undercooling makes the alloy melts far away from the equilibrium condition and strongly influences the microstructures. As a result, there is competition between the α-Co and the β-Co_3B phase. Besides, the eutectics in the inter-dendritic regions are refined remarkably into nano-eutectics and a small amount of rod-like eutectics surrounding the primary α-Co phase can be found. A similar microstructure was found in the laser re-melting of Ni-30wt%Sn alloys [123]. In the case of $\Delta T \approx 158$ K, the primary α-Co phase becomes more equiaxed, whereas, the inter-granular eutectics do not suffer any discernible change; see Fig. 3.4c. At the maximal undercooling obtained in the present work $\Delta T \approx 213$ K, although only one recalescence event can be found in the cooling history (Fig. 3.2d), two transformation processes can be distinguished from the solidification microstructures, i.e., the primary solidification of the α-Co phase and the second eutectic solidification of the α-Co and β-Co_3B phases. Furthermore, the anomalous eutectics are predominant and the primary α-Co phase is further refined; see Fig. 3.4d. The anomalous eutectics can be classified into two types, i.e. the coarse anomalous eutectics containing micron-sized α-Co particles and the fine-grained anomalous eutectic containing submicron-sized α-Co particles.

Since the solidification microstructure changes from a hypereutectic structure to a hypoeutectic structure as the increase of undercooling, it is rational to assume that there is a critical undercooling for the transition. Regarding the fact that the undercooling caused by spontaneous nucleation sometimes is not easy to obtain a desired undercooling, controlled solidification should be carried out. Fig. 3.5 shows the microstructure of the sample processed by controlled solidification with an undercooling of $\Delta T \approx 80$ K. The microstructure is dominated by anomalous eutectics in which the granular α-Co grains are uniformly distributed within the β-Co_3B matrix; a similar microstructure was found in the Ni-Sn eutectic alloys [124].

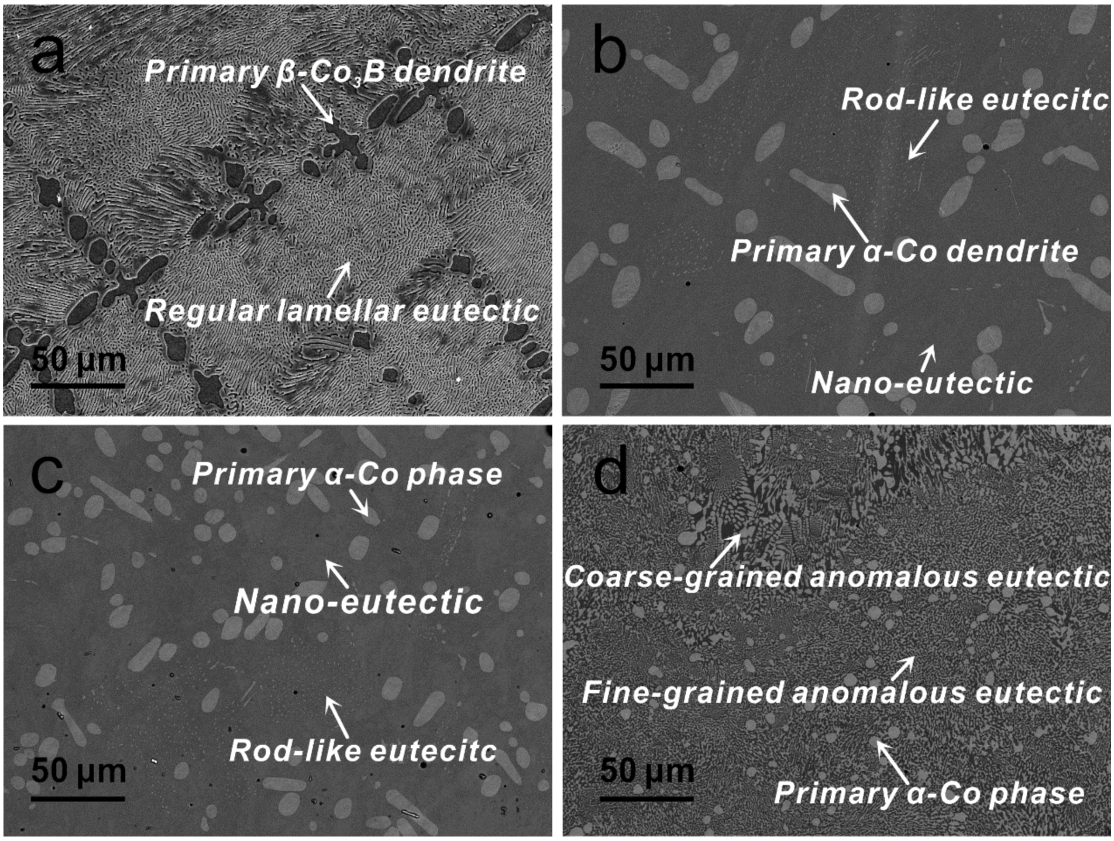

Fig. 3.4. Sectional microstructures of the samples processed by spontaneous solidification with different undercooling: (a) $\Delta T \approx 35$ K, (b) $\Delta T \approx 119$ K, (c) $\Delta T \approx 158$ K and (d) $\Delta T \approx 213$ K.

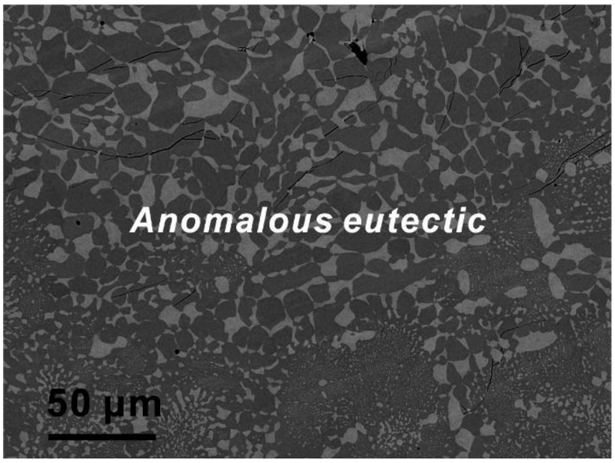

Fig. 3.5. Microstructures of the sample processed by controlled solidification with an undercooling of $\Delta T \approx 80$ K.

3.3.4 EBSD analysis

In order to show the grain orientations upon microstructure evolutions and achieve more evidence for phase selection, EBSD analysis was carried out to index four phases, i.e., β-Co_3B, α-

Co, ε-Co and Co_2B. It should be noted that the ε-Co and Co_2B phases are formed by partial solid-state phase transformations of the α-Co and β-Co_3B phases.

The EBSD orientation maps and the {100}/{0001} pole figures (PFs) of the Co-20at.%B hypoeutectic alloy solidified at $\Delta T\approx35$K are shown in Figs. 3.6a-3.6h. Three main orientations can be found for the β-Co_3B phase, even though the differences between the orientations are not that large (Figs. 3.6a and 3.6b). Because the dendrite and the surrounding regular lamellar of β-Co_3B phase share the same orientation, the lamellar eutectics should be formed by an epitaxial growth mechanism. For the lamellar eutectics whose constituent phases grow cooperatively, the eutectic orientation might be fixed and thus the three main orientations of the β-Co_3B phase should correspond to the three main orientations of α-Co, which however is not the case; see Figs. 3.6c and 3.6d. The gain orientations of the α-Co phase are much multiple, indicating that a fixed eutectic orientation between the α-Co and β-Co_3B phases is not fulfilled. For the precipitated ε-Co (Figs. 3.6e and 3.6f) and Co_2B (Figs. 3.6g and 3.6h) phases, no preferred orientations can be found. The random orientations of ε-Co and Co_2B suggest that there is no prefer orientation between the precipitation and the parent phase. Since the ε-Co and Co_2B phases resulted from the partial solid-state phase transformation of the α-Co and β-Co_3B phases have nothing to do with phase selection upon rapid solidification, only the grain orientations of the α-Co and β-Co_3B phases are shown as follows.

Fig. 3.7 shows the EBSD orientation maps and the {100} PFs for the case of $\Delta T\approx119$ K. From the EBSD analysis, it can be found intuitively that the above hypereutectic structure is replaced by a hypoeutectic structure with α-Co as the primary phase. In terms of the colors of the β-Co_3B phase, more than six eutectic colonies can be discerned in the indexed EBSD map of Fig. 3.7a. The β-Co_3B phase of the individual colonies appears continuous and is considered to be the matrix [125]. The PF of Fig. 3.7b shows that the β-Co_3B phases are oriented along four major poles. On the other hand, the globular α-Co particles are oriented by more scattered poles and often have similar orientations for the neighboring grains, indicating that they are formed by the same primary α-Co dendrites, see Fig. 3.7d.

Fig. 3.8 shows the EBSD orientation maps and the {100} PFs for the case of $\Delta T\approx80$ K processed by controlled solidification. There are several alternative coarse-grained and fine-grained anomalous eutectic colonies indexed by a rich variety of colors; see Fig. 3.8a. In the EBSD map indexed by the α-Co phase only (Fig. 3.8c), the α-Co phase has only one main orientation besides some random orientations (Fig. 3.8d). It is not easy to distinguish the primary phase from both the morphologies and the grain orientations. According to the growth-controlled mechanism between the α-Co phase and the β-Co_3B phase as verified by the dendrite growth model in the following Section, the primary phase for the case of ΔT≈80 K might be the β-Co_3B phase.

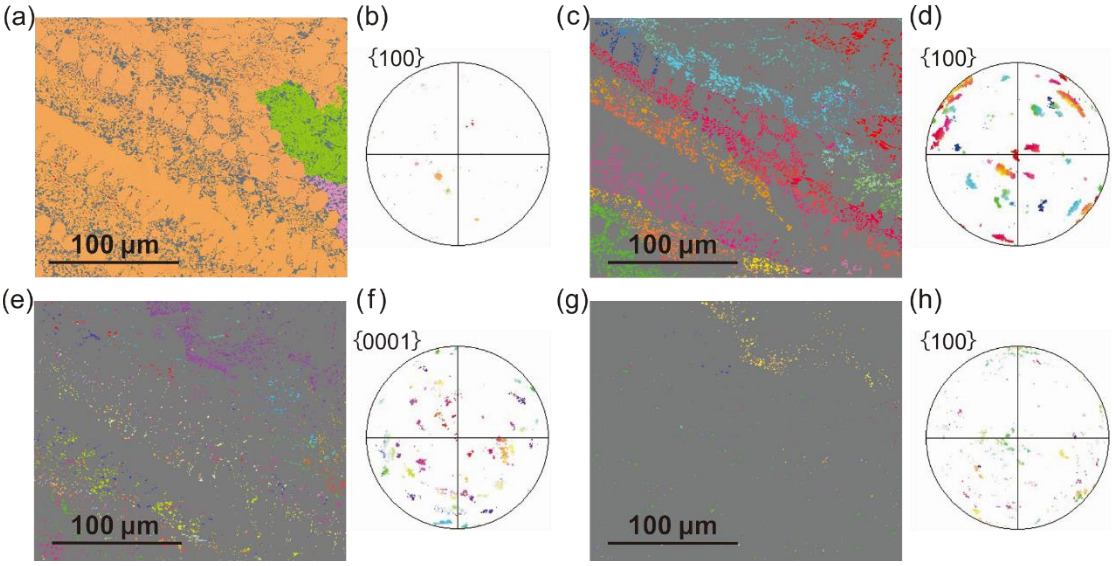

Fig. 3.6. EBSD analysis of the primary β-Co_3B dendrite and the regular lamellar eutectic microstructure of the Co-20at.%B hypereutectic alloy with an undercooling of ΔT≈35 K. (a) EBSD orientation map and (b) {100} pole figure of the β-Co_3B phase. (c) EBSD orientation map and (d) {100} pole figure of the α-Co phase. (e) EBSD orientation map and (f) {0001} pole figure of the ε-Co phase. (g) EBSD orientation map and (h) {100} pole figure of the Co_2B phase.

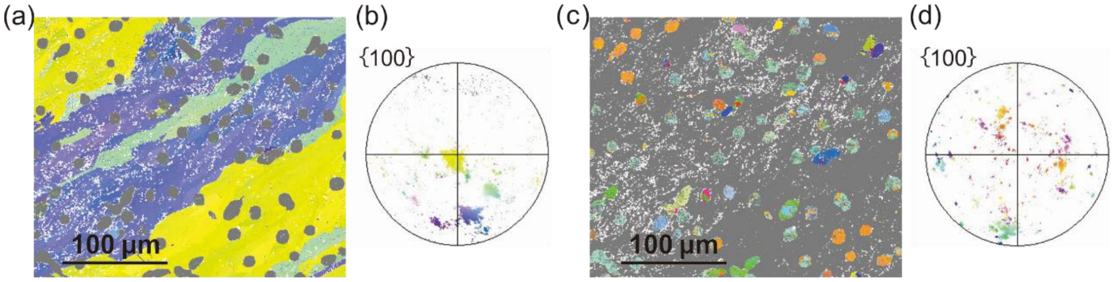

Fig. 3.7. EBSD analysis of the primary α-Co phase surrounding by the nano-eutectic structure and rod-like eutectic of the Co-20at.%B hypereutectic alloy with an undercooling of ΔT≈119 K. (a) EBSD orientation map and (b) {100} pole figure of the β-Co_3B phase. (c) EBSD orientation map and (d) {100} pole figure of the α-Co phase.

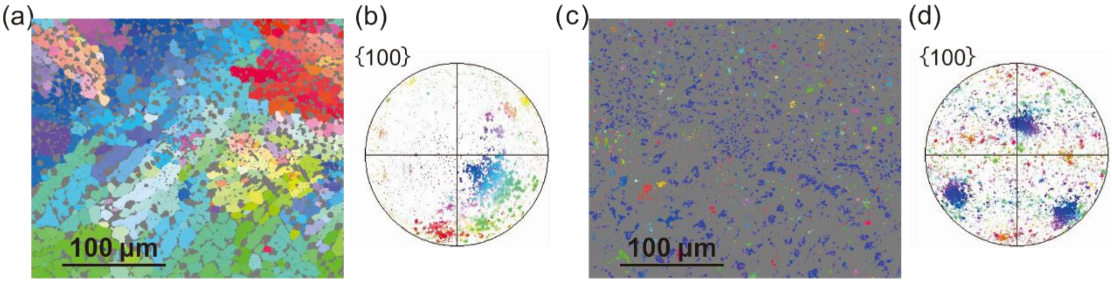

Fig. 3.8. EBSD analysis of the two kinds of anomalous eutectic structures of the Co-20at.%B hypereutectic alloy with an undercooling of ΔT≈80 K. (a) EBSD orientation map and (b) {100} pole figure of the β-Co_3B phase. (c) EBSD orientation map and (d) {100} pole figure of the α-Co phase.

3.4 Phase selection

3.4.1 Mechanism of phase selection

In the undercooled Co-20at.%B hypereutectic alloy, the primary phase with the increase of undercooling changes from the β-Co_3B phase to the α-Co phase, i.e., phase selection. According to Li et al. [110], the nucleation-controlled mechanism determines the primary phase in an undercooled melt when the competing phases share the same crystalline characteristics and have comparable interface kinetic coefficients. The growth-controlled mechanism occurs when the interface kinetic coefficients for the competing phases are different by two or three orders. The interface kinetic coefficient, μ can be given as [110]:

$$\mu = \frac{\Delta H_f V_s}{R_g T_L^2} \tag{3.1}$$

where R_g is the gas constant, V_s is the speed of sound in the liquid, ΔH_f and T_L are the heat of fusion and the liquidus temperature, respectively.

For solidification of ordered intermetallic compounds, the atoms must sort themselves onto various sub-lattices. This process requires diffusion, therefore, the sound speed in the liquid, V_s, should be replaced by the diffusion speed, V_D. Regarding that V_s is about 1-10 km s^{-1} and V_D is about 1-10 m s^{-1} for typical metallic alloys [126], V_s =2000 m s^{-1} and V_D =10 m s^{-1} are chosen for the α-Co solid solution and the β-Co_3B intermetallic compound, respectively. Substituting them and the parameters in Table 3.1 into Eq. (3.1), μ of the two phases can be calculated, i.e. $\mu_{\alpha\text{-Co}}$=1.236 m s^{-1}

K^{-1} and $\mu_{\beta\text{-Co3B}}$=0.039 m s^{-1} K^{-1}. The value of μ based on V_D for the β-Co_3B intermetallic compound is two orders smaller than the value based on V_s for the α-Co solid solution, indicating that the growth-controlled mechanism should be responsible for phase selection. In order to present more evidences for the phase selection mechanism in the undercooled Co-20at.%B hypereutectic alloy, a quantitative analysis was carried out as follows for both competitive nucleation and competitive growth.

Table 3.1

Physical parameters used for calculating the interface kinetic coefficients of the α-Co solid-solution phase and the β-Co_3B intermetallic compound.

Property	Symbol	Unit	α-Co	β-Co_3B	Ref.
Heat of fusion	ΔH_f	J mol^{-1}	16060	65738.8	[119, 121]
Melting point	T_m	K	1768	1431	[74]

3.4.2 Competitive nucleation

Nucleation of a specific crystallographic phase is characterized by the activation energy (ΔG^*) for forming a nucleus of critical size in the undercooled melt. The nucleation barrier is the interface energy ($\sigma_{S/L}$) between the crystal nucleus and the undercooled melt [105]. According to the classical nucleation theory [127], the critical work for forming of a cap-like nucleus on a flat substrate can be expressed by:

$$\Delta G^* = \frac{16\pi\sigma_{S/L}^3}{3\Delta G_V^2} f(\theta) \tag{3.2}$$

Here ΔG_V is the difference of volume free energy between the solid phase and the liquid phase, which is determined using a linear approximation proposed by Turnbull [128]:

$$\Delta G_V = \Delta H_f \frac{T_m - T}{T_m} \tag{3.3}$$

where T_m is the melt temperature, $f(\theta)$ is the catalytic potency factor in the case of heterogeneous nucleation which is dependent on the wetting angle θ.

The interfacial energy $\sigma_{S/L}$ can be estimated by the negentropic model of Spaepen and Meyer [129]:

$$\sigma_{S/L} = \alpha \frac{\Delta S_f}{N_A^{1/3} V_m^{2/3}} T \tag{3.4}$$

where ΔS_f is the entropy of fusion, N_A is the Avogadro's number, V_m is the mole volume, and α is a factor depending on the structure of the nucleus, e.g., α=0.71 for the BCC phase and α=0.86 for the FCC or HCP phase [98].

Due to the uncertainty in the distribution and characteristic of heterogeneous sites within the sample, $f(\theta)$ is rarely documented and thus is always taken to be a fitting parameter [107]. Therefore, ΔG^*s of the two phases for homogeneous nucleation (i.e. $f(\theta)=1$) was first calculated as a function of ΔT; see the solid lines in Fig. 3.9. The other parameters used are listed in Table 3.2. Using an assumption of identical $f(\theta)$ for both the α-Co and the β-Co_3B phase, ΔG^* of the α-Co phase is always larger than that of the β-Co_3B and the curves of ΔG^* for the two phases have no intersections in the whole measured range of ΔT. Noting from Eq. (3.2) that varying $f(\theta)$ only moves the curve of ΔG^* upward or downward (e.g., the case of $f(\theta)=0.1$ shown as the dashed lines in Fig. 3.9). One can conclude safely that the β-Co_3B phase has a priority in nucleation invariably as compared to the α-Co phase.

If nucleation-controlled is the case, the β-Co_3B phase should be favored over the α-Co phase over the whole measured range of ΔT because of its lower value of ΔG^*. From the present experiments, however, a transition of the primary phase from the β-Co_3B phase to the α-Co phase happens at high undercooling; see Fig. 3.4. One should be noted that the successful formation of an effective nucleus does not mean that micronucleus can definitely grow into a macro crystal [102]. For example, in the peritectic $Y_3Fe_5O_{12}$ (YIG) [130] system, even though the seeding needles made by YIG can supply a good substrate for nucleation, direct growth of YIG cannot be found whereas the competing phase with a higher growth kinetic coefficient, i.e., $YFeO_3$, can be observed throughout the entire sample below the peritectic temperature. Nagashio et al. [130] attributed it to the high complexity of the structure of the intermetallic compound that prevents their successive development from the well-matched as-nucleated substrate. In this sense, a description of the growth kinetics becomes inevitable.

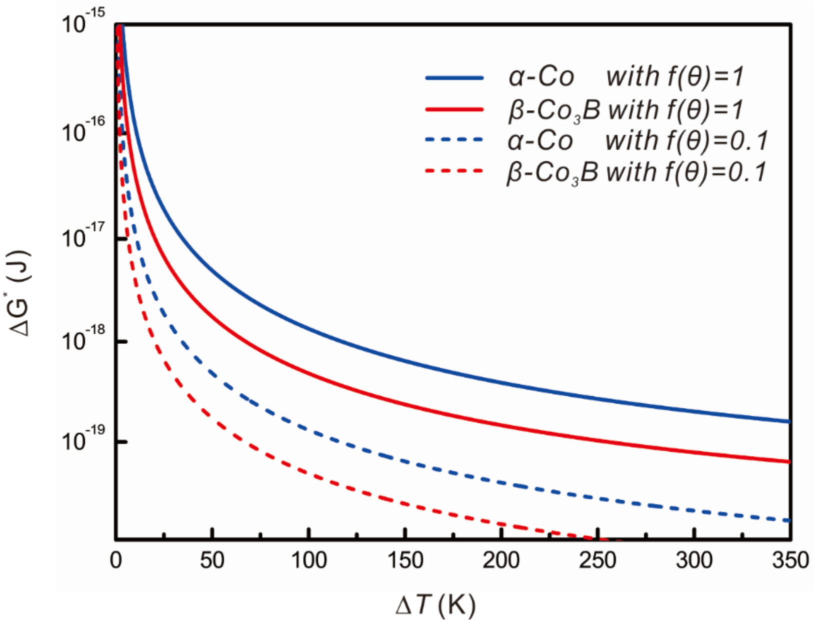

Fig. 3.9. Critical work for nucleation of the α-Co solid-solution phase (blue lines) and the β-Co_3B intermetallic compound (red lines) in the undercooled Co-20at.%B hypereutectic alloy.

Table 3.2

Physical parameters used for calculating the critical work for nucleation of the α-Co solid-solution phase and the β-Co_3B intermetallic compound.

Property	Symbol	Unit	α-Co	β-Co3B	Ref.
Mole volume	V_m	$cm^3\ mol^{-1}$	6.63	24.3	[119, 131]
Stuctural factor	α	-	0.71	0.86	[98]
Wetting factor	$f(\theta)$	-	0.1, 1	0.1, 1	Present work

3.4.3 Competitive growth

According to the LKT/BCT dendrite growth model [132], the total undercooling at the dendrite tip is consisted by four contributions:

$$\Delta T = \Delta T_t + \Delta T_c + \Delta T_r + \Delta T_k \tag{3.5}$$

Here ΔT_t, ΔT_c, ΔT_r and ΔT_k are the thermal undercooling, the solute undercooling, the curvature undercooling and the kinetic undercooling, respectively, which can be given as follows:

$$\begin{aligned}
\Delta T_t &= \frac{\Delta H_f}{C_p} I_V\left(P_t\right) \\
\Delta T_c &= m_L C_0\left(1-\frac{1}{1-(1-k) I_V\left(P_c\right)}\right) \\
\Delta T_r &= \frac{2\Gamma}{R} \\
\Delta T_k &= \frac{V}{\mu}
\end{aligned} \tag{3.6}$$

where C_p is the specific heat of the liquid, $P_t = VR/2\alpha'$ is the thermal Peclet number, R is the radius of curvature at the dendrite tip, V is the growth velocity, α' is the thermal diffusivity, I_V is the so-called Ivantsov function, m_L is the slope of *liquidus*, C_0 is the initial alloy composition, $P_c = VR/2D_L$ is the chemical Peclet number, D_L is the diffusion coefficient of the solute in the liquid, k is the partition coefficient and $\Gamma = \sigma/\Delta S_f$ is the Gibbs-Thomson coefficient, coefficient.

To take into account the solute trapping effect, the velocity dependent partition coefficient proposed by Aziz [133] is adopted:

$$k \approx k\left(V\right) = \frac{k_e + a_0 V/D_L}{1 + a_0 V/D_L} \tag{3.7}$$

where k_e is the equilibrium partition coefficient and a_0 is the atomic spacing. The physical parameters used are listed in Table 3.3. A detailed description of the LKT/BCT model calculation is available in Refs. [134].

Accordingly, the crystal growth velocities of the α-Co and β-Co_3B phases in the undercooled Co-20at.%B hypereutectic alloy are calculated as a function of undercooling (see Fig. 3.10). Obviously, with the increase of undercooling, the growth velocities of the two phases increases quickly and they are nearly equal at low undercooling. In fact, the growth velocity of the β-Co_3B phase is slightly larger than that of the α-Co phase when the undercooling is smaller than 122 K. Nevertheless, when the undercooling is higher than 122 K, the growth velocity of the α-Co phase becomes larger than that of β-Co_3B phase. This can be used to explain the transition from hypereutectic to hypoeutectic in the undercooled Co-20at.%B hypereutectic alloy. At low undercooling, the growth velocity (the critical work of nucleation) of the β-Co_3B phase is slightly larger (much smaller) than that of the α-Co phase and the growth-controlled (nucleation-controlled) mechanism choose the β-Co_3B phase as the primary phase. At high undercooling, the growth velocity of the α-Co phase can be much larger than that of the β-Co_3B phase and the primary phase according to the growth-controlled mechanism is the α-Co phase; see Fig. 3.4b-3.4d. In one word, phase-selection in the undercooled Co-20at.%B hypereutectic alloy is growth-controlled.

Table 3.3

Physical parameters used for calculating the crystal velocities of α-Co and β-Co_3B phases in the undercooled Co-20at.%B hypereutectic alloy.

Property	Symbol	Unit	Value	Ref.
Specific heat of liquid	C_p	J mol^{-1} K^{-1}	30.6	Calculate from [131]
Thermal diffusion coefficient	α'	m^2 s^{-1}	1.961×10^{-6}	Present work
Equilibrium solute partition coefficient	$k_e\left[\alpha\text{-Co}\right]$	-	0.02	Calculate from [135]
Equilibrium solute partition coefficient	$k_e\left[\beta\text{-}Co_3B\right]$	-	1.35	Calculate from [135]
Atomic spacing	a_0	m	3×10^{-10}	Present work
Slope of equilibrium liquidus	$m_L\left[\alpha\text{-Co}\right]$	K $(at\%)^{-1}$	-20.81	Calculate from [74]
Slope of equilibrium liquidus	$m_L\left[\beta\text{-}Co_3B\right]$	K $(at\%)^{-1}$	6	Calculate from [74]
Solute diffusion coefficient	D_L	m^2 s^{-1}	5×10^{-9}	[101]

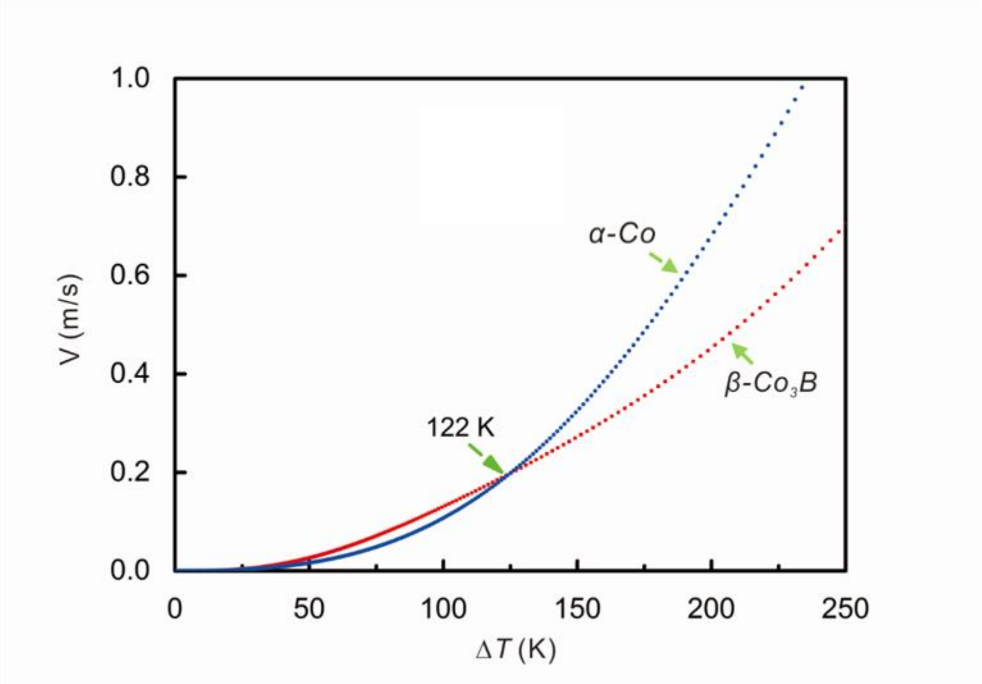

Fig. 3.10. Crystal growth velocities of the *α*-Co and *β*-Co_3B phases in undercooled Co-20at.%B hypereutectic alloy as a function of undercooling predicted by the LKT/BCT model.

The fact that the microstructure is entirely eutectics at intermediate undercooling but is the primary *β*-Co_3B (*α*-Co) dendrites with inter-dendritic eutectics form at modest (high) undercooling indicate that a skewed coupled eutectic zone exists in the Co-B alloy system. This commendably reflects the growth difficulty associated with the faceted *β*-Co_3B phase as compared to the solid-solution *α*-Co phase. The coupled zone in the Co-B system should be skewed to the faceted *β*-Co_3B phase. The high growth velocity leads to the formation of the primary *α*-Co dendrites even for the Co-20at.%B hypereutectic alloy.

3.5 Summary

Microstructure evolution and phase selection in the undercooled hypereutectic Co-20at.%B alloy have been investigated by the melt fluxing technique. The as-solidified microstructures were analyzed by EBSD. The phase selection mechanism was discussed by competitive nucleation and competitive growth. Our main conclusions are as follows:

(1) A transition from hypereutectic to hypoeutectic was found at a critical undercooling of 119 K, i.e., phase election between the α-Co and the β-Co_3B phase occurs in the undercooled Co-20at.%B hypereutectic alloy. When ΔT<119 K, the morphologies of the undercooled Co-20at.%B alloy are characterized by a primary directional dendritic structure of β-Co_3B phase surrounded by the α-Co+β-Co_3B regular lamellar eutectics. When ΔT>119 K, the above hypereutectic microstructure is replaced by the hypoeutectic microstructure with the α-Co phase as the primary phase.

(2) From the calculation results of the critical works for nucleation of the α-Co and β-Co_3B phase in the Co-20at.%B hypereutectic alloy, the critical work for nucleation of the β-Co_3B phase is always smaller than that of the α-Co phase, indicating that the β-Co_3B phase should be the preferred nucleation phase over the whole range of undercooling. The successful formation of an effective nucleus, however, does not mean that micronucleus can definitely grow into a macro crystal.

(3) The growth velocities of the α-Co and β-Co_3B phases in the undercooled Co-20at.%B hypereutectic alloy have been calculated according to the LKT/BCT model. It was found that the preferred nucleation phase is not always the faster growing phase with the increase of undercooling. The β-Co_3B phase has a prior nucleation over that of α-Co phase at low undercooling. However, the growth velocity of the β-Co_3B phase is far lower than that of α-Co phase when ΔT>122 K, indicating that phase selection between the α-Co and β-Co_3B phases is growth-controlled.

3.5 Résumé

L'évolution de la microstructure et la sélection de phase dans l'alliage hypereutectique sous-refroidi Co-20at.%B ont été étudiées par la technique de l'encapsulation vitreuse. Les microstructures de solidification ont été analysées par EBSD. Le mécanisme de sélection des phases a été discuté en terme de compétition entre nucléation et croissance. Nos principales conclusions sont les suivantes :

(1) Une transition de l'hypereutectique à l'hypoeutectique a été observée avec un sous-refroidissement critique de 119 K, c'est-à-dire que le choix de phase entre la phase α-Co et la phase β-Co_3B se produit dans l'alliage hypereutectique Co-20at.%B sous refroidi. Lorsque $\Delta T<119$ K, les morphologies de l'alliage Co-20at.%B sous-refroidi sont caractérisées par une structure dendritique directionnelle primaire de phase β-Co_3B entourée par l'eutectique lamellaire régulier α-Co+β-Co_3B. Lorsque $\Delta T>119$ K, la microstructure hypereutectique ci-dessus est remplacée par la microstructure hypoeutectique avec la phase α-Co comme phase primaire.

(2) D'après les résultats des calculs des énergies critiques de nucléation des phases α-Co et β-Co_3B dans l'alliage hypereutectique Co-20at.%B, l'énergie critique de nucléation de la phase β-Co_3B est toujours inférieure à celle de la phase α-Co, indiquant que la phase β-Co_3B devrait être la meilleure phase de nucléation sur la gamme de température du sous-refroidissement. La formation réussie d'un noyau critique ne signifie toutefois pas que le micro-noyau peut définitivement se transformer en macro-cristal.

(3) Les vitesses de croissance des phases α-Co et β-Co_3B dans l'alliage hypereutectique Co-20at.%B sous-refroidi ont été calculées selon le modèle LKT/BCT. On a constaté que la phase de nucléation préférée n'est pas toujours la phase de croissance plus rapide avec l'augmentation du sous-refroidissement. La phase β-Co_3B a une nucléation antérieure à celle de la phase α-Co à faible

sous-refroidissement. Cependant, la vitesse de croissance de la phase β-Co_3B est bien inférieure à celle de la phase α-Co lorsque $\Delta T > 122$ K, indiquant que la sélection de phase entre les phases α-Co et β-Co_3B est contrôlée par la vitesse de croissance.

Chapter 4 Temperature induced structure transition above *liquidus*

4.1 Introduction

Liquid polymorphism [59], a liquid characterized by constantly rearranging configurations, could exist in distinct modifications (phases and states) which are the same in composition but different in local structure and thermodynamic properties [136], is one of the long-standing issues due to its importance for understanding the fundamental nature of liquid and amorphous states. There are growing experimental and theoretical supports for the existence of liquid-liquid structure transitions and liquid-state anomalies, for instance, in H_2O [137], P [20], Ca [26], Te [27], $Ge_2Sb_2Te_5$ [60] and other liquids including multicomponent bulk metallic glass-forming systems [35, 136]. Controlling the liquid states, based on the L-LSTs, has been confirmed to be effective in regulating the subsequent solidification processes, microstructures and properites [138, 139]. Yu et al. [36] found that the solidification behaviours of $Bi_2Te_{3-x}Se_x$ alloys are strongly related to their parent liquid states. The samples that experienced L-LST show that the solidification undercooling degree is increased and the crystal growth time is shortened. As a result, the solidified lamellae are refined and homogenized, the prevalence of low-angle grain boundaries between these lamellae is increased, and the Vicker Hardness is enhanced.

4.2 Overheating dependent undercooling

Nucleation in an undercooled melt is the process with which the formation of new phases begins and is one of the most important fundamental processes in solidification [106, 140]. In general, nucleation can be classified into homogeneous nucleation [141] and heterogeneous nucleation [142]. The latter is an extrinsic process that is dominated by the experimental conditions, whereas the former is an intrinsic process that depends on the properties of the system [143]. By avoiding heterogeneous nucleation, the melt can be solidified at a temperature below its melting temperature or liquidus temperature, i.e., solidification of undercooled melts [97]. Undercooling as is well known is a physical quantity that is sensitive to the structure of liquids, e.g., even very tiny intrinsic un-melted crystals in the liquids can act as the growth nuclei and may reduce considerably undercooling [66, 144]. Since undercooling depends strongly on the liquid structures, the undercooled melt should be an ideal system to study the liquid structures and L-LST.

In this section, cyclic superheating and cooling were carried out for the undercooled hypereutectic Co-20at.%B, eutectic Co-18.5at.%B and hypoeutectic Co-17at.%B alloys. The critical overheating temperature was found to be existent in but different for all the three alloys. DSC measurements show that there is a thermal absorption peak in the heating process above the melting temperature or the *liquidus* temperature that corresponds to L-LST. In other words, L-LST does occur when the overheating temperature is above the critical overheating temperature and it should relate highly to nucleation in the undercooled Co-B eutectic melts. The effect of structure transitions on the nucleation temperature was analyzed in-depth by the recent nucleation theory that considers the structure of overheated melts and the alloy composition-dependent overheating temperature was ascribed to the change of local favored structures.

4.2.1 Experimental

Samples with a mass of about 2 g were cut form the ingot to precede the undercooling experiments. The sample was placed first into the quartz crucible together with the flux of boron oxide. After that the sample was melted and cyclically superheated and undercooled. The samples were heated to a series of temperatures, e.g., regarding that the melting point of eutectic $Co_{81.5}B_{18.5}$ alloy is 1133 ℃, and the overheating temperatures were set to be 1200, 1300, 1350, 1370, 1380, 1400, 1450, and 1500 ℃; the details are shown in Table 4.1. After heating the sample to the pre-set overheating temperature, the melt was held therein for 5 min and then naturally cooled down to 800 ℃. The detailed information on the undercooling experiments is given in Chapter 2. The undercooling in each cycle may vary considerably especially in the first several cycles. Afterwards, the melts become uniform and stable with very light fluctuation, thus the undercooling becomes almost constant. The cyclic of melting and solidification was executed until the undercooling can be stable for at least 10 cycles (i.e. the deviation of undercooling is within 5 ℃). In this case, the undercooled melts are considered to be in a relatively stable state and the mean undercooling is evaluated from the 10 consecutive cycles.

The thermodynamic behavior of the Co-B alloys was measured by DSC (NETZSCH, STA449C). The samples of DSC experiments with a mass within 35 mg were cut from the original ingot. The sample was placed in a corundum crucible, heated and cooled in an argon atmosphere. It was heated up firstly to 1500 ℃ at a rate of 20 ℃/min and then cooled down to the room temperature at the same rate.

Table 4.1. The overheating temperature for heating and solidfication of the Co-B eutectic alloys

Alloy	the overheating temperature T^o, ℃							
$Co_{80}B_{20}$	1300	1325	1350	1360	1380	1400	1450	1500
$Co_{81.5}B_{18.5}$	1200	1300	1350	1365	1380	1400	1450	1500
$Co_{83}B_{17}$	1300	1350	1375	1380	1390	1400	1450	1500

4.2.2 Dependence of undercooling on the overheating temperature

Fig. 4.1 shows the mean undercooling of Co-B eutectic alloys with different overheating temperatures. The undercooling is defined as the difference between the nucleation temperature (T_n) and the melting temperature (T_m) for the eutectic $Co_{81.5}B_{18.5}$ or the difference between the nucleation temperature (T_n) and the *liquidus* temperature (T_l) for the hypereutectic $Co_{80}B_{20}$ and hypoeutectic $Co_{83}B_{17}$ alloys. One can see that for all the three alloys, there is a critical overheating temperature T_c^o at which there is a sharp increase of the mean undercooling, i.e. below T_c^o, the mean undercooling is about 80 ℃, whereas above T_c^0, the mean undercooling is about 200 ℃. The critical overheating temperature is 1360 ℃ for the hypereutectic $Co_{80}B_{20}$ alloy (Fig. 4.1a), 1380 ℃ for the eutectic $Co_{81.5}B_{18.5}$ alloy (Fig. 4.1b) and 1390 ℃ for the hypoeutectic $Co_{83}B_{17}$ alloy (Fig. 4.1c). It should be pointed out that the mean undercooling here is not obtained for all the cycles but the cycles when the undercooled melt becomes stable.

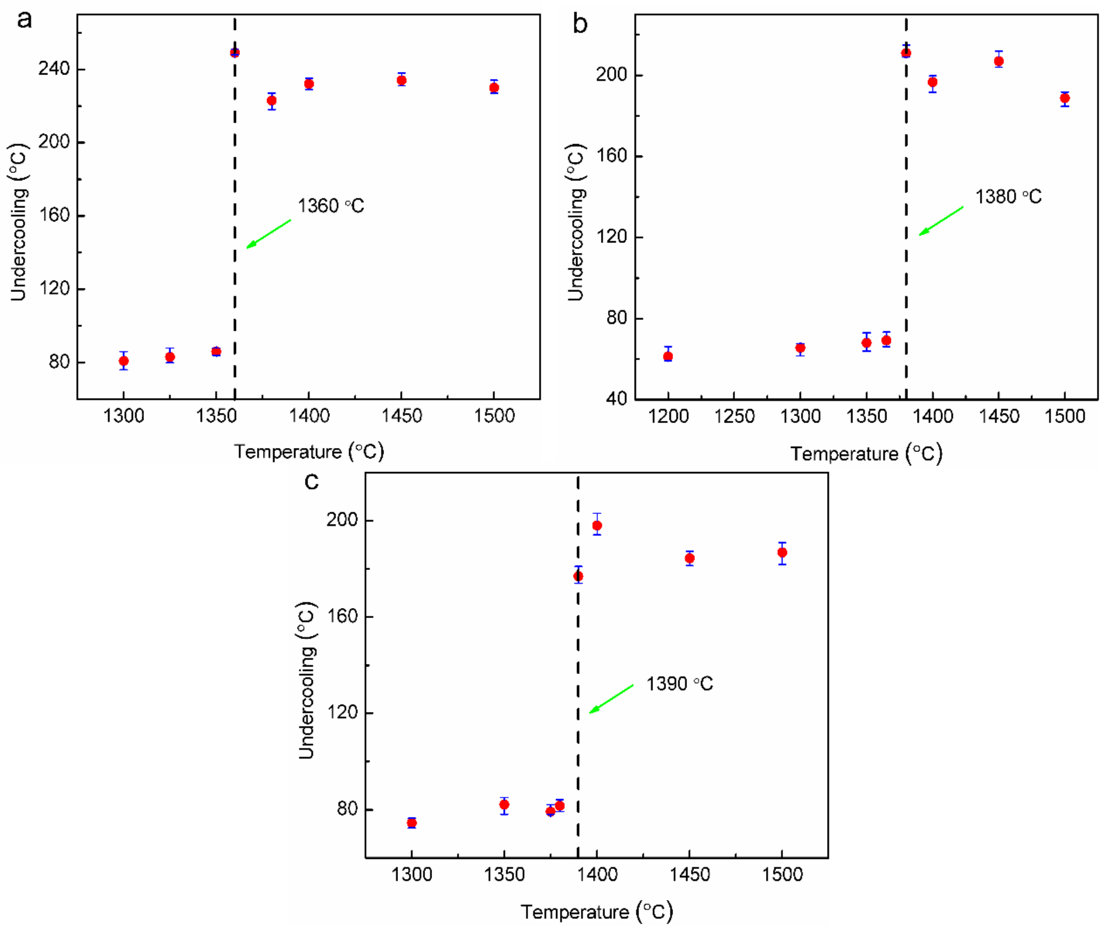

Fig. 4.1. The mean undercooling of eutectic Co-B alloys with different overheating temperatures: (a) hypereutectic $Co_{80}B_{20}$; (b) eutectic $Co_{81.5}B_{18.5}$; (c) hypoeutectic $Co_{83}B_{17}$.

The structure transition in the overheating melt corresponds to the breakage of previous atomic bonds and the formation of new atomic bonds. Because of the difference in the bonding energy between atoms, L-LST is inevitably accompanied by the thermal effect. On this basis, a series of DSC measurements were carried out to show the temperature-induced L-LST in the overheating Co-B melts (see Fig. 4.2). For all the hypereutectic $Co_{80}B_{20}$, eutectic $Co_{81.5}B_{18.5}$ and hypoeutectic $Co_{83}B_{17}$ alloys, there is a thermal absorption peak in the heating process above T_m or T_l but not in the cooling process. The peak temperature is about 1363.4 ℃ for the hypereutectic $Co_{80}B_{20}$ alloy (Fig. 4.2a), 1382.7 ℃ for the eutectic $Co_{81.5}B_{18.5}$ alloy (Fig. 4.2b) and 1392.1 ℃ for the hypoeutectic

$Co_{83}B_{17}$ alloy (Fig. 4.2c). The consistency between the peak temperatures in the DSC curve and the critical overheating temperatures (e.g. the temperature difference is less than 4 ℃) indicates that the temperature-induced L-LST does occur when the overheating temperature is above the critical overheating temperature and nucleation in the undercooled Co-B eutectic melts is highly related to L-LST. To show whether such peak temperatures are heating rate dependent or not, another DSC test, shown in Fig. 4.2d, with a heating and cooling rate of 10 ℃/min was carried out for the eutectic $Co_{81.5}B_{18.5}$ alloy. One can see that the peak temperature is still at about 1383.4 ℃, being consistent with result 1382.7 ℃ in Fig. 4.2b. In other words, L-LST is not that dependent on the heating and cooling rate.

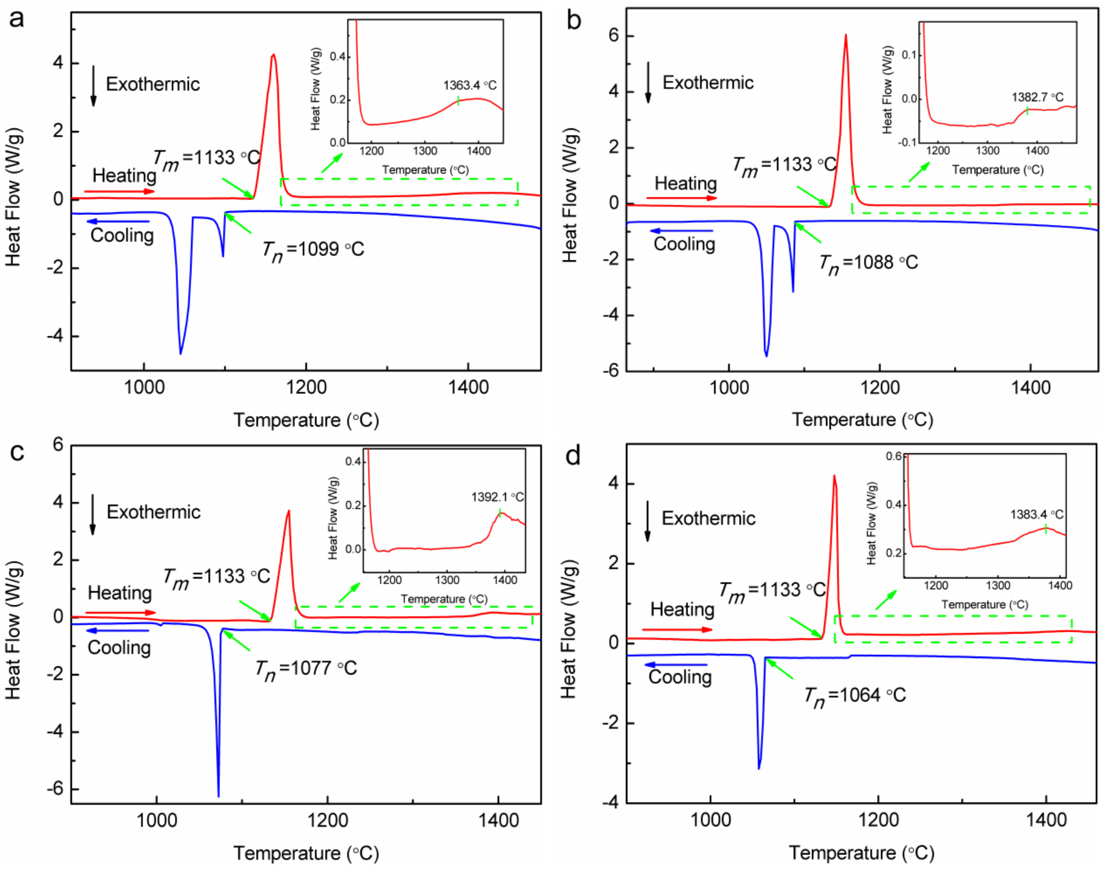

Fig. 4.2. DSC curves of the Co-B eutectic alloys: (a) hypereutectic $Co_{80}B_{20}$ with the heating and cooling rate as 20 ℃/min; (b) eutectic $Co_{81.5}B_{18.5}$ with the heating and cooling rate as 20 ℃/min; (c) hypoeutectic $Co_{83}B_{17}$ with the heating and cooling rate as 20 ℃/min; (d) eutectic $Co_{81.5}B_{18.5}$ with the heating and cooling rate as 10 ℃/min.

In all the DSC tests, there are no apparent peaks in the liquid state during the cooling process (see Fig. 4.2), indicating L-LST in Co-B melts is irreversible. To show this point further, superheating and cooling of eutectic $Co_{81.5}B_{18.5}$ alloy was carried out with different overheating temperature, shown in Fig. 4.3, in which only the cooling histories of the last four cycles are shown. In this case, the undercooling can hold stable after eighteen cycles when the overheating temperature is larger than the critical overheating temperature which is in line with the result in Fig. 4.1b. The large undercooling holds even when the overheating temperature is smaller than the critical overheating temperature (e.g. for 24th and 25th cycles). After that, the undercooling becomes small (e.g. for 26th cycle). If L-LST is reversible, the large undercooling cannot be obtained once the overheating temperature is smaller than the critical overheating temperature.

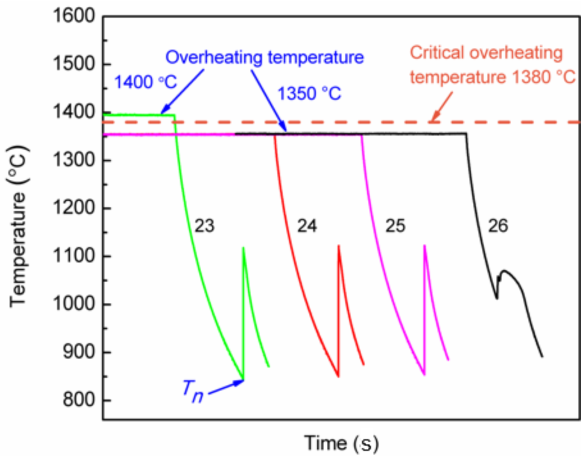

Fig. 4.3. Nucleation temperatures of the $Co_{81.5}B_{18.5}$ alloy at different cycles and with different overheating temperatures.

4.2.3 Liquid-liquid structure transition vs. nucleation

It is generally believed that the atomic bonds of crystals are only partly broken upon melting and there are a lot of short-range ordering domains that correspond to the solid crystal in the melts within a wide temperature range above T_m or T_l [145]. Thus, the structures of melts are micro-heterogeneous in the continuous heating procedure and many micro-domains (even unsolved particles) exist in the melt [10]. The micro-heterogeneous structure, that changes with the overheating temperature, is metastable or thermodynamically non-equilibrium. Because different overheating temperatures correspond to different melt states, the structures and properties of many materials are related to the thermal history of their original melts, e.g. the microstructure of amorphous alloys is much more homogeneous if the precursor melts are more overheated [145].

The correlation between the solidified microstructures and the melt thermal history is attributed to different melt microstructures or different liquid states. The overheating temperature as one of the most essential processing parameter has a decisive influence on the liquid state. Thermodynamically, overheating prompts the transition between different liquid states and a critical overheating temperature may correspond to the transition point between the two distinct forms that can be detected.

Zu et al. [10, 17] assumed that L-LST is a transition from an inhomogeneous liquid state to a more uniformed liquid state. There are both chemical and topological short-range orders in the liquid alloys with negative excess enthalpy, e.g. both the chemical short-range domains with micro-structures similar to Co_3B and the residual short-range ordering of cube/hexagon solid Co co-exist in the molten Co-B eutectic alloys. These minor domains as the fluctuation of energy dissipate and engender with time and space, but they do not vanish with their statistical equilibrium structures, sizes and constituents. However, as long as the temperature reaches T_c^0, the inter-atomic bonds in the original domains are broken, the old domains are reduced, and at the same time, new domains form with a relatively more uniformed liquid structure state.

In this study, the melt is encapsulated in the molten glass slag that is close to the levitation melting condition and the impurities in the melt can be removed via electromagnetic stirring and the adhesion of slag. Consequently, the cavity induced heterogeneous nucleation mechanism [146] which is always used to describe the effect of overheating on the undercooling for the nucleation process of a melt on a second solid surface cannot be used. Magnetic field texturing has already shown the possible existence of intrinsic solid nuclei above the melting temperature T_m [147]. The clusters exist in the melt and act as the intrinsic growth nuclei, thus leading to nucleation in the cooling process. During solidification, the Co-B melt which did not experience L-LST has lots of relatively larger size micro-domains. Through fluctuations in structure and energy, these micro-domains can be easily extended to the critical size of the crystal nucleus at a low undercooling. However, when the melt experienced L-LST, it is harder to nucleate because of the smaller and more homogeneous short-range orders, and the melt needs a larger undercooling to nucleate as shown in Fig. 4.1.

After analyzing the experimental results of nucleation and growth in 38 elements, Tournier [66, 67, 148, 149] proposed an explanation by improving the classical nucleation theory. His idea is that the transfer of Δn conduction electrons equalizing the Fermi energies of a particle containing n free electrons and the melt creates an interface electrostatic energy $-\varepsilon_v$ per volume unit that stabilizes tiny crystals above T_m. These crystals act as the intrinsic nuclei in the undercooled melts and their presence reduces the critical energy barrier. All these tiny crystal are predicted to be survival up to a critical temperature $T_{m2} = 1.196T_m$. Therefore ε_v is taken to be part of the contributions to the volume free energy change ΔG_v and the total free energy change due to the formation of a nuclei with a radius R is:

$$\Delta G_{ls}\left(T\right) = \left(\Delta G_v - \varepsilon_v\right)4\pi\frac{R^3}{3} + 4\pi R^2\sigma_{ls} \tag{4.1}$$

where $\Delta G_V = \Delta H_m\theta / V_m$, $\sigma_{ls}(V_m / N_A)^{-1/3} = \alpha_{ls}\Delta H_m / V_m$, $\theta = T / T_m - 1$. Here σ_{ls} is the interface energy, V_m is the molar volume of liquid, ΔH_m is the enthalpy of fusion at the melting temperature. The critical radius R_{ls} for nucleation can be found if the partial derivation of ΔG_{ls} with respect to R is set to be zero, that is

$$\frac{\partial \Delta G_{ls}\left(T\right)}{\partial R} = 0 \tag{4.2}$$

Integrating Eq. (4.1) with Eq. (4.2) yields:

$$R_{ls} = -2\frac{\sigma_{ls}}{\Delta G_v - \varepsilon_v} = -2\frac{\alpha_{ls}}{\theta - \varepsilon_{ls}}\left(\frac{V_m}{N_A}\right)^{1/3} \tag{4.3}$$

If a non-dimensional parameter ε_{ls} is introduced to evaluate the contribution by ε_v, i.e. $\varepsilon_v = \varepsilon_{ls}\Delta H / V_m$, the critical radius R_{ls} is positive when $\theta < \varepsilon_{ls}$ and negative when $\theta > \varepsilon_{ls}$, indicating that a tiny crystal can be survival up to a second melting temperature $T_{m2} = (1 + \varepsilon_{ls})T_m$.

The nucleation rate I per unit volume and per second in an undercooled melt can be given as a function of the critical activation barrier $\Delta G_{ls}^*(T) / k_B T$ with k_B the Boltzmann's constant:

$$In(Ivt) = In(K_V vt) - \frac{\Delta G_2^*}{k_B T} = In(K_V vt) - \frac{16\pi\Delta S_m \alpha_{ls}^3}{3N_A k_B(\theta - \varepsilon_{ls})^2(1+\theta)} \tag{4.4}$$

The solidification can be initiated when one nucleation event occurs in the melt, i.e., $Ivt = 1$.

According to Tournier [66, 67, 148, 149], the relation between ε_{ls} and θ was obtained as:

$$\varepsilon_{ls} = 0.217(1 - 2.5\theta^2) \tag{4.5}$$

The so-called second melting temperature T_{m2} can then be calculated by integrating Eqs. (4.1)-(4.5) and summarized in Table 4.2. The consistency between T_{m2} and T_c^0 indicates that the re-melting of tiny crystals that can be survival above to T_{m2} is highly related to LLST. It should be pointed out that LLST in the liquid may alter the wetting angle due to the abrupt change of surface tension. When LLST occurs, the surface tension changes, thus resulting in the change of $f(\theta)$ and the increase of undercooling [12, 19]. Furthermore, the nucleation model of Tournier [66, 67, 148, 149] is actually proposed for pure elements, and it is plausible to be applied to the current Co-B alloys but at least it can explain satisfactorily the present experimental results.

Table 4.2

The calculation results of Co-B eutectic alloys using the modified classical nucleation-growth model.

Alloy	ΔT, ℃	T_m (or T_L), ℃	θ	E_{LS}	T_{m2}, ℃	T_c^0, ℃
$Co_{80}B_{20}$	230	1140	0.202	0.195	1362	1360
$Co_{81.5}B_{18.5}$	200	1133	0.177	0.214	1375	1380
$Co_{83}B_{17}$	190	1150	0.165	0.202	1382	1390

4.2.4 Critical overheating temperature vs. alloy composition

As mentioned above, the melts of Co-B eutectic alloys are mainly consist of micro-structure similar to Co_3B and the residual short-range ordering of cube/hexagon solid Co within a certain range above T_m or T_l. When the overheating temperature is up to T_c^0, the kinetic energy of the atoms becomes high enough to overcome the energy barrier so that the Co-Co or Co-B atomic bonds are continuously broken. During LLST, through the adjustment of atomic bonds and the structural rearrangement, the size of short-range orders becomes smaller, and the liquid structures are completely different to the original ones and become more homogeneous. It should be pointed out that T_c^0 is different for different alloys and increases with the composition of Co (Fig. 4.3). In the liquid, there are locally favored structures [16] such as Co-rich domains and Co_3B-rich domains at the temperature not far from the T_m or T_l, the type, amount and size of which change with the composition and temperature as has been evidenced by the magnetization variations of the liquids [18, 28]. Hence, it is reasonable to conclude that the dependence of T_c^0 on the alloy composition is due to the change of local favored structures.

4.3 Temperature induced LLST studied by in-situ measuring the magnetization

The finding of magnetic order in liquid superfluid ^{3}He [150] and amorphous magnet [151] proves the existence of magnetic ordering in disordered systems. By in-situ measuring the magnetization, the increasing magnetization in supercooled Co [82] and $Co_{80}Pd_{20}$ [152] is observed when close to the Curie temperature. That is to say, it will be quite efficient way to use magnetization as a physical parameter to detect the structure changes in liquids of some alloys since magnetic susceptibility of different structures will be different. Structure transition is shown to be available in many liquid systems and many clusters or orderings can be exist in liquids which can be enhanced when the melts comes into undercooled state [28]. Thus it will be quite interesting to directly monitor this transition via magnetization measurement from overheating above *liquidus* to supercooled state. In this section, an investigation is extended to binary Co-B alloys, by in-situ measuring the magnetization, a temperature-induced L-LST is observed.

4.3.1 Magnetic field intensity dependent characteristic transition temperature

Fig. 4.4a shows the magnetization and temperature of the $Co_{81.5}B_{18.5}$ alloy measured in a 1.56 T magnetic field. The sample is heated at constant rate of 20 K/min to about 1753 K and after holding therein for 20 min, it was cooled down to 1103 K at 20 K/min. By in-situ magnetization measurement, the melting point (i.e., eutectic temperature, marked as T_m, 1406 K in Fig. 4.4b) and nucleation point (marked as T_N, 1176 K in Fig. 4.4c) are clearly evidenced. The nucleation temperature is far below the melting point, indicating a large undercooling before solidification.

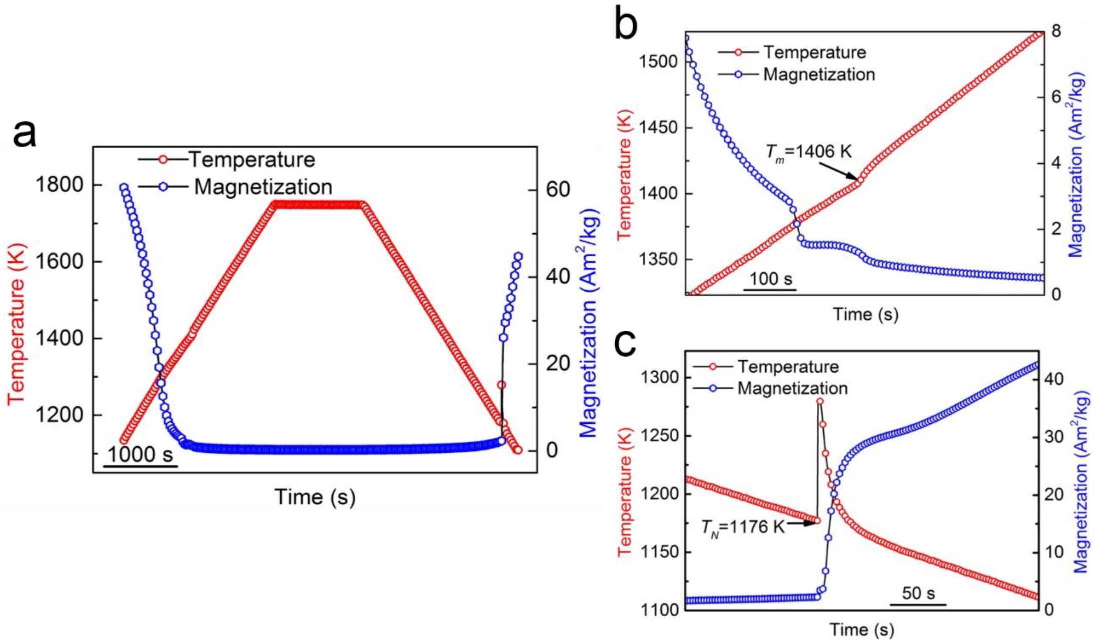

Fig.4.4. (a) The temperature and magnetization curve of $Co_{81.5}B_{18.5}$ alloy. The enlarged areas show the ranges around (b) the melting point and (c) the nucleation temperature. The field intensity and gradient at the sample position are 1.56 T and 23.235 T/m, respectively.

In Fig. 4.5, the magnetization of the $Co_{81.5}B_{18.5}$ alloy is plotted against temperature. During the heating process, the magnetization first decreases rapidly with the increasing temperature, especially when approaching the T_C of the ferromagnetic α-Co phase around 1250 K. Afterwards, an abnormal second drop of magnetization occurs around 1380 K, just below the T_C of pure Co (1394 K [82]). Considering the α-Co phase is the sole ferromagnetic phase (T_c of the other phases are very low [153] and therefore their contribution can be neglected), the variance of solid solubility of boron in the α-Co phase can lead to an "inhomogeneity". The soluble boron concentration in the primary or subsequently α-Co phase formed during eutectic decomposition could be different because of the non-equilibrium solidification process [154]. The α-Co phase is easy to precipitate as a primary phase in the solidification of undercooled Co-based near eutectic alloys, especially under strong magnetic field [81, 120].

Above T_m, the magnetization decreases rapidly due to melting of the alloy. During the cooling process (see Fig. 4.5), the magnetization of the liquid first follows the heating path and no distinct inflection point arises when going over T_m. The magnetization of the undercooled liquid below T_m follows the same trend until an abrupt increase of the temperature at the point T_N, showing the onset of nucleation. Then solidification takes place quickly and the magnetization increases rapidly. Shortly afterwards, a turning point determined around 1150 K from the slope variation can be found during the cooling process, which should correspond to the solid-solid transition, i.e., $Co_3B \rightarrow Co_2B + \alpha\text{-}Co$ [155].

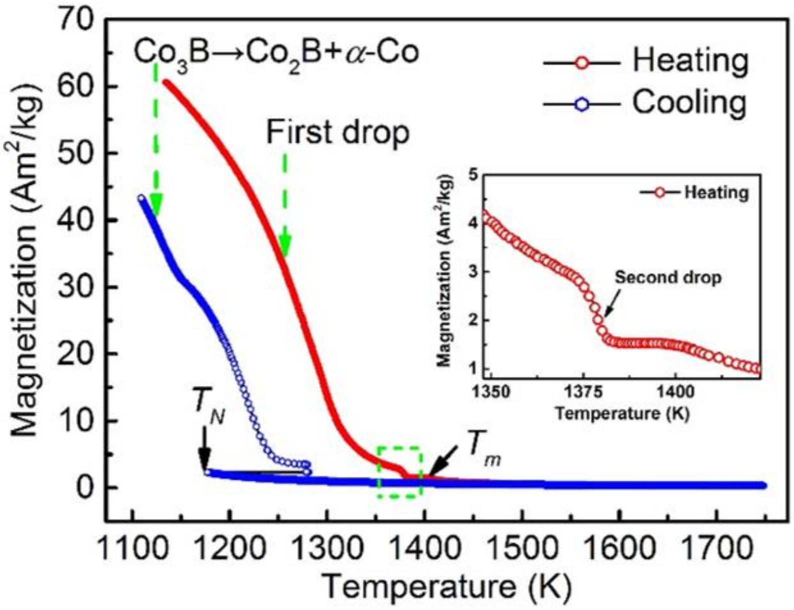

Fig.4.5. Temperature dependence of magnetization for $Co_{81.5}B_{18.5}$ alloy measured in the field of 1.56 T where the field gradient is 23.235 T/m. The inset figure is the enlarged area (dashed square) showing the second drop of magnetization during heating.

The susceptibility of the paramagnetic liquid $Co_{81.5}B_{18.5}$ alloy obeys the Curie-Weiss law:

$$\chi = \frac{C}{T - \theta_p} \tag{4.6}$$

where χ, C, and θ_p are the magnetic susceptibility, the Curie constant and the paramagnetic Curie temperature (approximately to be equal to T_C), respectively. Integrating $M=\chi H$ with equation (1) yields:

$$\frac{1}{M} = \frac{T - \theta_p}{HC} \tag{4.7}$$

Accordingly, θ_p can be obtained by plotting the $1/M$-T curve (Fig. 4.6) and extrapolating the curve where $1/M$ equals to zero. During heating, a distinct crossover is observed at T_0 (~1553 K). During cooling, the $1/M$-T curve nearly overlaps with the heating curve above T_0 but remains incessant with the identical slope below T_0. By extrapolating the two linear ranges, two paramagnetic Curie temperatures, corresponding to $\theta_p(\mathrm{L_I})$ (~1098 K) during heating and $\theta_p(\mathrm{L_{II}})$ (~1303 K) during cooling are determined. Two different slopes of $1/M$ correspond to two different magnetic states, i.e. different structures. The crossover observed at T_0 can be interpreted as being related to the magnetism of Co ions in the melt and the change in their coupling. Hence, the crossover at T_0 during heating demonstrably indicates that a temperature-induced LLST in the overheated $\mathrm{Co_{81.5}B_{18.5}}$ alloy.

By the method above, the LLST temperature (T_0), paramagnetic Curie temperatures ($\theta_p(\mathrm{L_I})$, $\theta_p(\mathrm{L_{II}})$) at different field intensities 0.52 T, 1.56 T and 2.6 T are determined. The results are shown in Table 1. Within the limits of error, T_0 (~1553 K) can be considered constant independent of the field intensity. $\theta_p(\mathrm{L_{II}})$ (~1093 K) decreases slightly with the increasing field intensity and $\theta_p(\mathrm{L_I})$ shifts to lower temperature with the increasing field intensity. This could be due to the differences of the origin solid state before melting. For each field value, the samples were processed reproductively several times. The measurement at a given field then corresponds to a sample already solidified at the same field value. As it was already observed, magnetic field promotes the precipitation of primary α-Co phase [81]. The liquid may keep the memory of the previous solid state since the atomic bonds of crystals are only partly broken upon melting [145], therefore, the locally favored structures such as Co-rich domains after melting may be different under different magnetic field, which is the probable explanation for the magnetic field intensity dependence of $\theta_p(L_I)$. A more in depth analysis of the structure and stability will be required to confirm this assumption.

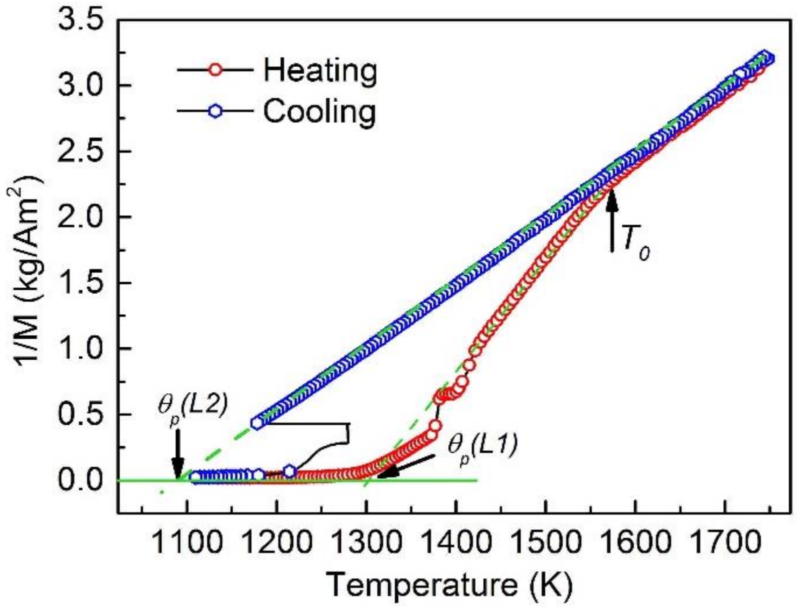

Fig.4.6. Inverse magnetization (1/*M*) as a function of temperature curve of $Co_{81.5}B_{18.5}$ alloy measured in 1.56 T magnetic field where the field gradient is 23.235 T/m.

Table 4.3 Determined results of the related parameters (T_0, $\theta_p(L_I)$, $\theta_p(L_{II})$).

Field intensity	T_0, K	$\theta_p(L_I)$, K	$\theta_p(L_{II})$, K
0.52 T	1551±3	1328.5±0.3	1099±0.2
1.56 T	1552.5±7.3	1304.5±1.4	1096.5±0.4
2.6 T	1553.1±9.4	1279.5±2.6	1090.4±0.3

4.3.2 Composition dependent characteristic transition temperatures

The chemical composition may have a significant influence on the structural motifs in liquids

[156]. In the work of Zou et al. [48], the temperature dependent density of Ni-Ti melts was studied. Unexpectedly, a nonlinear dependence of density on temperature was found in the $Ni_{50}Ti_{50}$ melt but not in the $Ni_{45}Ti_{55}$ and $Ni_{55}Ti_{45}$ melts, indicating that the LLST is highly dependent on the composition. For the Co-B eutectic melt [51], a non-Curie-Weiss behavior that corresponds to a tempeature induced LLST was reported by in-situ measuring the magnetization. Because LLSTs are very important for modulating the liquid states, three alloys, i.e., hypereutectic $Co_{80}B_{20}$, eutectic $Co_{81.5}B_{18.5}$ and hypoeutectic $Co_{83}B_{17}$ (at.%) with similar compositions, were selected to verify whether such non-Curie-Weiss behavior is universal or not for the Co-B binary alloy system.

Fig. 4.7 shows the magnetization and temperature of the hypereutectic $Co_{80}B_{20}$ alloy measured under a magnetic field of 1.56 T. The sample is heated with a rate of 10 K min^{-1} to about 1740 K and holding therein for 10 min. Then, it is cooled down to 1140 K with the same rate. By in-situ measuring the temperature and magnetization, the melting behavior (the eutectic temperature T_E=1406 K, and the *liquidus* temperature T_L=1445 K), the solidication process (nucleation temperature T_N=1164 K and recalescence temperature also known as crystal growth temperture T_G=1352 K) and other possible transformations (e.g., the ferromagnetic transition) can be observed. A large undercooling of ΔT=281 K (=0.195T_L) is achieved before solidification. During heating, the magnetization diminishes rapidly with the temperature, especially when close to the Curie temperature of the ferromagnetic α-Co phase around 1250 K. When nucleation happens, recalescence makes the magnetization decrease. After that, solidication takes place quickly and the magnetization increases rapidly. The hysteresis of magnetization at the moment of nucleation is due to the response delay of the blance.

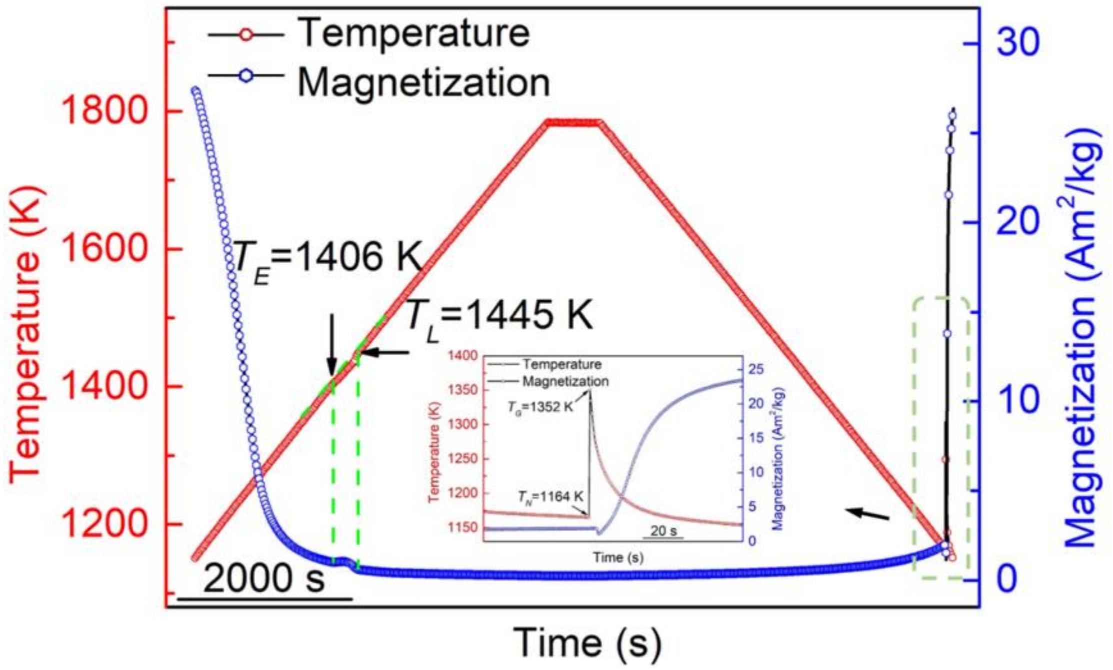

Fig. 4.7. The temperature and magnetization as a function of time for the $Co_{80}B_{20}$ alloy. The insert figure is the enlarged area (dashed square) showing the solidification process. The field intensity and gradient at the sample position are 1.56 T and 23.235 T m^{-1}, respectively.

Above T_L, the sample turns to be a fully paramagnetic liquid. As mentioned above, its susceptibility obeys the Curie-Weiss law, i.e., eq. (4.7). Accordingly, θ_p can be determined from the 1/M versus T curve by extrapolating the curve to where 1/M equals to zero. The slope of the curve is inversely proportional to the Curie constant (In SI unit, the Curie constant can be expressed as $C=\frac{\rho}{H\cdot slope}$, where ρ=8900 kg m^{-3} is the density of Co-B alloys). Fig. 4.8a shows the plot of 1/M versus T of the $Co_{80}B_{20}$ alloy. During heating, a distinct crossover dividing the curve into two linear segments with different slopes is observed at T_0 (=1522 K). During cooling, the 1/M versus T curve coincides with the heating curve above T_0 and the tendency continues below T_0 until nucleation happens. Two diverse paramagnetic Curie temperatures corresponding to two distinct forms of liquids are found, i.e., high-magnetization liquid (HML) I and low-magnetization liquid (LML) II. By extrapolating the two linear ranges, θ_p=1279 K and C=0.7611 K for liquid I, and

θ_p=1056 K and C=1.4738 K for liquid II are determined. This strongly indicates that a temperature-induced L-LST, which is interpreted as being related to the magnetism of Co ions in the melt and the change in their coupling, in the overheated $Co_{80}B_{20}$ alloy. In addition, the plot of 1/M versus T does not exhibit a change in the slope until the temperature reaches a critical value of T_0, indicating that this L-LST is a thermal-activation process.

The atomic bonds of crystals are only partly broken at temperatures not far above the *liquidus* temperature. As a result, the liquid structures are normally inhomogeneous, e.g., containing solid-like, topologically short-range ordered and/or chemically short-range ordered clusters [36]. Local structures characterized by the coexistence of metallic and covalent characters survive to some extent in the Co-B melt. As the temperature is within a critical scope, the interatomic bonds in the original clusters break, thus engendering new clusters with smaller size. This is responsible for the phenomenon of overheating dependent undercooling [65]. The Curie constant C can be expressed as [157]:

$$C = 2N_A \mu_p^2 D k_B^{-1} \tag{2}$$

N_A is Avogadro’s number, μ_p is the paramagnetic moment, D is a dimensionless number (D=0.7221) and k_B is Boltzmann’s constant. The value of C is dependent on μ_p. The covalent bond generally quenches the magnetic contribution for μ_p [157]. Therefore, the value of μ_p for the HML is smaller than the LML due to the survived covalent bonds. This is in line with the results obtained for the Curie constant.

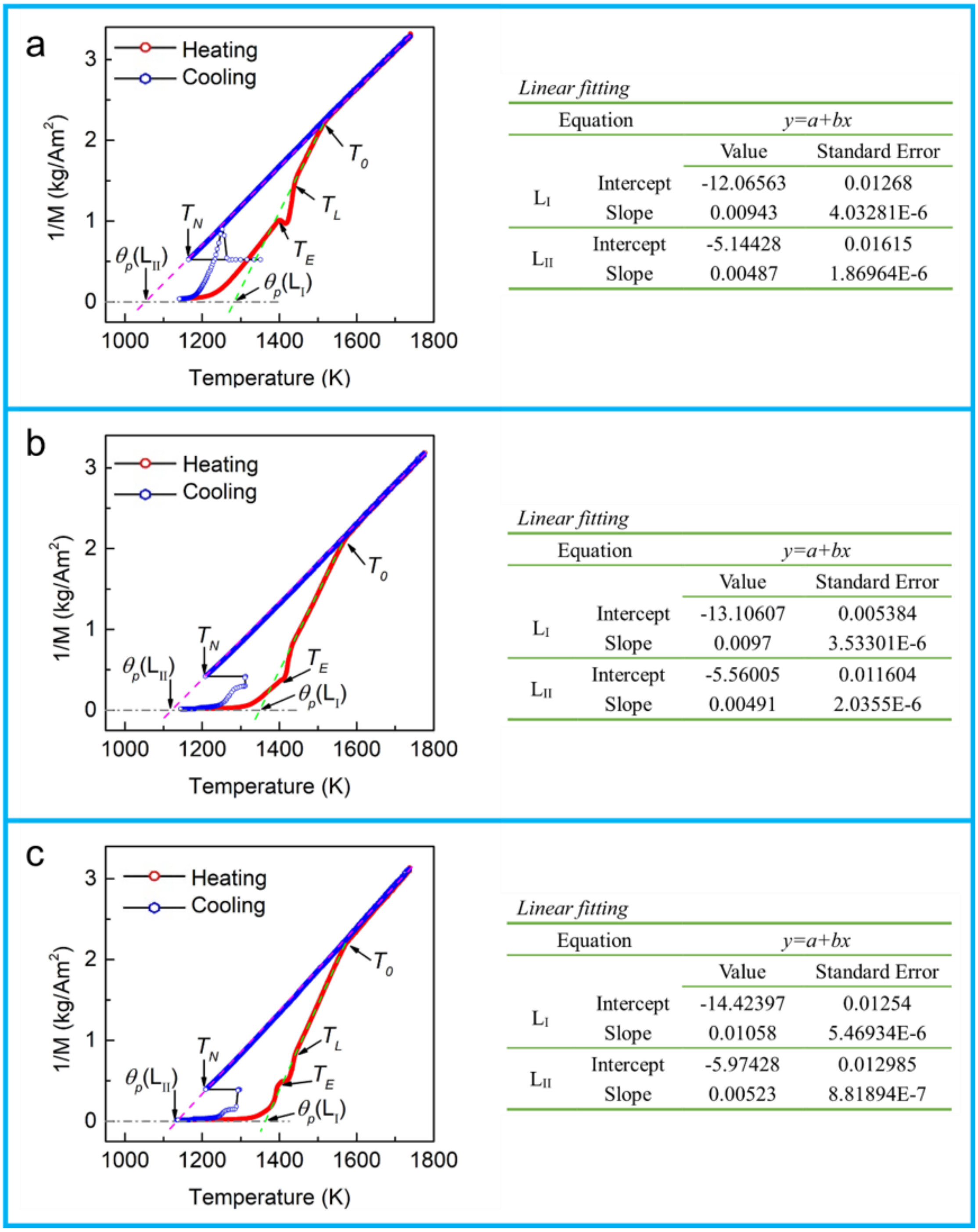

Linear fitting

Equation		$y=a+bx$	
		Value	Standard Error
L_I	Intercept	-12.06563	0.01268
	Slope	0.00943	4.03281E-6
L_{II}	Intercept	-5.14428	0.01615
	Slope	0.00487	1.86964E-6

Linear fitting

Equation		$y=a+bx$	
		Value	Standard Error
L_I	Intercept	-13.10607	0.005384
	Slope	0.0097	3.53301E-6
L_{II}	Intercept	-5.56005	0.011604
	Slope	0.00491	2.0355E-6

Linear fitting

Equation		$y=a+bx$	
		Value	Standard Error
L_I	Intercept	-14.42397	0.01254
	Slope	0.01058	5.46934E-6
L_{II}	Intercept	-5.97428	0.012985
	Slope	0.00523	8.81894E-7

Fig. 4.8. The inverse magnetization as a function of temperature for the Co-B alloys during the heating and cooling processes: (a) hypereutectic $Co_{80}B_{20}$, (b) eutectic $Co_{81.5}B_{18.5}$, and (c) hypoeutectic $Co_{83}B_{17}$. The green and magenta dashed lines are drawn as guides to the eyes, which correspond to linear fits according to the Curie-Weiss law for the two linear ranges corresponding to two distinct forms of liquids, i.e., HML I and LML II. The dash-dot line marks the auxiliary line of 1/M=0. The corresponding linear fitting functions and the standard errors for each composition are given in the tables.

In order to further confirm whether this liquid-state anomality is a universal formula for the Co-B binary alloy system or not, $Co_{81.5}B_{18.5}$ [51] and $Co_{83}B_{17}$ alloys were studied. Similar non-Curie-Weiss behavior but with different values of characteristic parameters were observed in the overheated state; see Figs. 4.8b and 4.8c. The variation tendency of these parameters with the incresing content of Co are shown in Fig. 4.9. The specific values of the parameters are listed in Table 4.4. The location of the critical point of L-LST (LLCP, T_0) and paramagnetic Curie temperatures (θ_p) for liquids I and II shift to higher temperature with the increasing content of Co. The type, amount and size of the locally favoured structures, e.g., the Co-rich domains and Co_3B-like configuration of Co-B pairs, vary with the composition. The magnetic moment of Co_3B motif 1.12 μ_B [153] is less than that of Co^{2+} 3.7 μ_B [158]. So the increase of Co^{2+} with the increasing Co content increases the net magnetic moment, which directly induces the increase of the Curie temperature. On the other hand, compared to the orthorhombic Co_3B-like motifs, the clusters that are similar to the solid structure of fcc-Co have tighter structure. Thus they have higher Curie temperature due to the magnetic moments reacting to their neighbouring electron spins and the effects become stronger when closer together [159]. Likewise, this leads to a lower value of μ_p and thereby a decrease of the Curie constant.

More attention should be paid to the increase tendency of these characteristic parameters with the increasing Co content. The increments of T_0, $\theta_p(L_I)$ and $\theta_p(L_{II})$ are 51 K, 72 K and 76 K from $Co_{80}B_{20}$ to $Co_{81.5}B_{18.5}$ while the increments are just 6 K, 12 K and 10 K from $Co_{81.5}B_{18.5}$ to $Co_{83}B_{17}$, even the change of composition is the same. This maybe due to the difference in the solid solubility of boron in the Co phase. For the $Co_{80}B_{20}$ and $Co_{81.5}B_{18.5}$ alloys, the Co phase are mainly formed during eutectic decomposition (there is a small number of primary Co phase for the $Co_{81.5}B_{18.5}$ alloy with large undercooling). However, there are a large amount of primary Co phase for the $Co_{83}B_{17}$ alloy. The amount of soluble boron in the primary Co phase and the Co phase formed during eutectic decomposition could be different because of the non-equilibrium solidification process [154]. The soluble boron concentration in the primary Co phase is larger than that in the Co phase formed during eutectic decomposition [51]. These small size interstitial boron atoms in the primary Co phase could decrease the Curie temperature, because the fluctuations of electron spins could become more prominent and result in disorder in magnetic moments [160]. Therefore, the increments of the magnetic properties from $Co_{81.5}B_{18.5}$ to $Co_{83}B_{17}$ are not comparable to the those from $Co_{80}B_{20}$ to $Co_{81.5}B_{18.5}$.

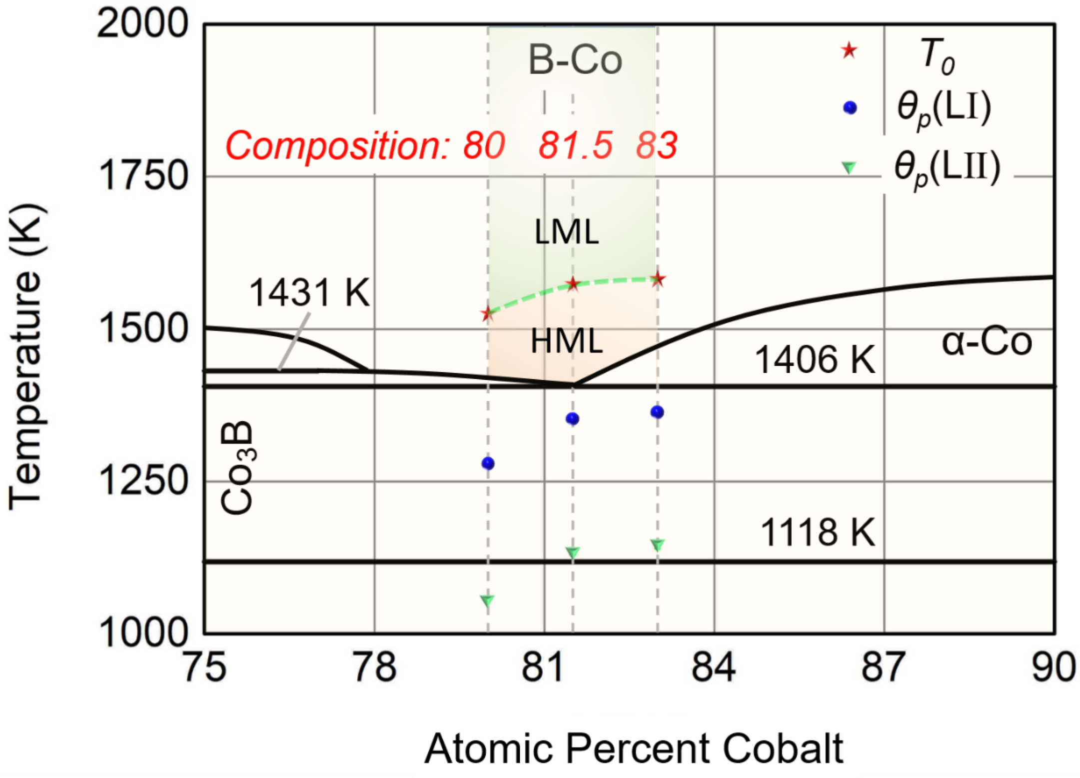

Fig. 4.9. Co-rich region of the Co-B phase diagram [155]. The symbols are the points for determining the characteristic parameters. The green dashed line is drawn as guides to the eyes, which represents the estimated increase tendency of the relevant data of different compositions for

T_0. With the help of this line, the region above the *liquidus* in the phase diagram is divided into two parts with different properties, i.e., HML in the low temperature region and LML in the high temperature region.

Table 4.4

Calculated results from the fitting functions given in Fig.4.8.

Alloy	T_0, K	$\theta_p(\mathrm{L_I})$, K	$\theta_p(\mathrm{L_{II}})$, K	$C(\mathrm{L_I})$, K	$C(\mathrm{L_{II}})$, K
$Co_{80}B_{20}$	1518 ±8	1279 ±1.9	1056 ±3.7	$0.7611^{+0.0004}_{-0.0003}$	$1.4738^{+0.0006}_{-0.0006}$
$Co_{81.5}B_{18.5}$	1575 ±5	1351 ±1.2	1132 ±2.8	$0.7399^{+0.0003}_{-0.0002}$	$1.4618^{+0.0006}_{-0.0006}$
$Co_{83}B_{17}$	1579 ±7	1363 ±2	1142 ±2.7	$0.6784^{+0.0003}_{-0.0004}$	$1.3724^{+0.0002}_{-0.0003}$

Furthermore, phase diagrams of ordinary alloys do not show any line above *liquidus* [7]. Based on the LLCP, a defined line corresponding to the estimated increase tendency of T_0 with composition can be drawn in the Co-B phase diagram roughly; see Fig. 4.9. With the help of this guideline [161], the region above the *liquidus* in the phase diagram is divided into two parts with different properties, i.e., HML in the low temperature region and LML in the high temperature region. The solidification behaviors with different thermal histories, i.e., overheating temperature above/below this line, are shown in Fig. 4.10. For the first cycle, with an overheating temperature above the defined line, the sample solidified from the parent liquid of LML shows that the nucleation undercooling degree is conspicuously enlarged. Whereas, for the second cycle, with an overheating temperature below the defined line, the sample solidified from the parent liquid of HML is very easy to nucleate. When the sample solidified from the HML region, the nucleation barrier is smaller since the liquid is more magnetic and the size of survived clusters are larger compared with the sample solidified from the LML region. This demonstrated the alteration of the solidification behavior due to different thermal histories is ascribed to their different liquid state. Therefore, this defined line has some guidance significances to the practical melt treatment.

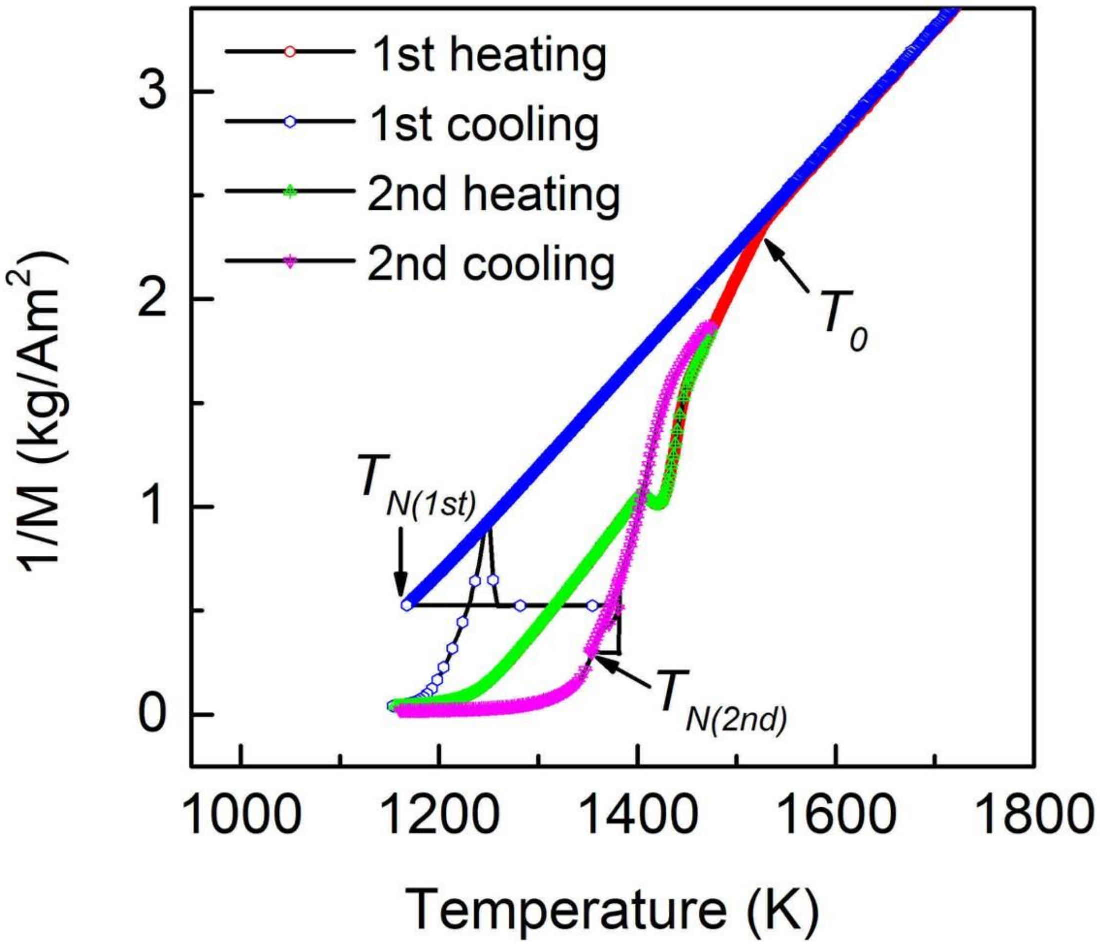

Fig. 4.10. The 1/*M*-*T* curves for the $Co_{80}B_{20}$ alloys during the heating and cooling processes in two adjacent cycles with different overheating temperatures. For sake of simplicity, the two adjacent cycles are named as the first cycle and the second cycle. The selected overheating temperatures are 1750 K (above T_0) for the first cycle and 1475 K (below T_0) for the second cycle.

4.4 Summary

Cyclic superheating and cooling as well as DSC measurements were carried out for the hypereutectic $Co_{80}B_{20}$, eutectic $Co_{81.5}B_{18.5}$ and hypoeutectic $Co_{83}B_{17}$ alloys. For each alloy, there is a critical overheating temperature T_c^0 at which there is a sharp increase of the mean undercooling, i.e. below (above) T_c^0, the mean undercooling is about 80 ℃ (200 ℃). The critical overheating temperature is 1360 ℃ for the hypereutectic $Co_{80}B_{20}$ alloy, 1380 ℃ for the eutectic $Co_{81.5}B_{18.5}$ alloy and 1390 ℃ for the hypoeutectic $Co_{83}B_{17}$ alloy.

DSC measurements show that there is a thermal absorption peak in the heating process above the melting temperature or the liquidus temperature, the peak temperature of which is nearly equal to the overheating temperature, indicating that the temperature-induced L-LST does occur when the overheating temperature is above the critical overheating temperature and it should relate highly to nucleation in the undercooled Co-B eutectic melts. L-LST is not dependent on the heating and cooling rates and is irreversible.

The effect of L-LST on nucleation is interpreted by the recent nucleation theory that considers the structure of overheated melts, according to which the second melting temperature T_{m2} can be calculated and is nearly equal to the critical overheating temperature T_c^0, indicating that the tiny crystals that can be survival above to T_{m2} is highly related to L-LST. This work provides further evidences for L-LST and is helpful for our understanding of solidification in undercooled melts.

The structure transition inside liquid $Co_{81.5}B_{18.5}$ alloy have been studied by in-situ magnetization measurement. The magnetic field independent L-LST temperature at ~1553 K is evidenced in the overheated $Co_{81.5}B_{18.5}$ alloy. Two paramagnetic Curie temperatures ($\theta_p(L_I)$, $\theta_p(L_{II})$) corresponding to the two different structures of the liquids are determined. $\theta_p(L_{II})$ is ~1093 K and decreases only slightly with the increasing magnetic field intensity, whereas, $\theta_p(L_I)$ shifts to lower temperature with the increasing magnetic field intensity.

Investigations were conducted to two other alloys, i.e., $Co_{81.5}B_{18.5}$ and $Co_{83}B_{17}$, and the results indicated that this anomalous behavior is a universal formula for the Co-B binary alloy system. With the increasing Co content, T_0, $\theta_p(L_I)$ and $\theta_p(L_{II})$ shift to higher temperatures and the Curie constants for the Liquid I and Liquid II decrease. Based on the LLCP, a defined guideline is drawn above the *liquidus* in the Co-B phase diagram, which has some guidance significances to the practical melt treatment.

4.4 Résumé

Des mesures de surchauffe et de refroidissement cycliques ainsi que des mesures DSC ont été effectuées pour les alliages hypereutectiques $Co_{80}B_{20}$, eutectiques $Co_{81.5}B_{18.5}$ et hypoeutectiques $Co_{83}B_{17}$. Pour chaque alliage, il y a une température critique de surchauffe T_c^0 à laquelle il y a une brutale augmentation du sous-refroidissement moyen, c'est-à-dire passant de 80 ℃ pour une surchauffe inférieure T_c^0, à 200 ℃ pour une surchauffe supérieure à T_c^0. La température critique de surchauffe est de 1360 ℃ pour l'alliage hypereutectique $Co_{80}B_{20}$, 1380 ℃ pour l'alliage eutectique $Co_{81.5}B_{18.5}$ et 1390 ℃ pour l'alliage hypoeutectique $Co_{83}B_{17}$.

Les mesures DSC montrent qu'il y a un pic d'absorption thermique dans le processus de chauffage au-dessus de la température de fusion ou de la température du liquidus, dont la température maximale est presque égale à la température critique de surchauffe, ce qui indique que la transition structurale liquide-liquide induite par la température se produit lorsque la température de surchauffe est supérieure à la température critique de surchauffe et que celle-ci doit être étroitement liée à la nucléation dans les liquides eutectiques Co-B sous refroidies. Cette transition structurale liquide-liquide ne dépend pas des vitesses de chauffage et de refroidissement et est irréversible.

L'effet de la transition structurale liquide-liquide sur la nucléation est interprété par la théorie récente de la nucléation qui considère la structure des métaux liquides surchauffés, selon laquelle la seconde température de fusion T_m^2 peut être calculée et est presque égale à la température critique de surchauffe T_c^0, indiquant que la survie de petits cristaux au-dessus de T_m^2 est fortement liée à la transition structurale liquide-liquide. Ce travail fournit d'autres preuves de la transition structurale liquide-liquide et est utile pour notre compréhension de la solidification dans les métaux liquides sous-refroidis.

La transition structurale dans l'alliage liquide $Co_{81.5}B_{18.5}$ a été étudiée par des mesures d'aimantation in-situ. Une température de transition struturale liquide-liquide, indépendante du champ magnétique à ~1553 K, est mise en évidence dans l'alliage surchauffé $Co_{81.5}B_{18.5}$.

Deux températures paramagnétiques de Curie ($\theta p(L_I)$, $\theta p(L_{II})$), correspondant aux deux structures différentes des liquides sont déterminées. $\theta p(L_{II})$ est ~1093 K et ne diminue que très légèrement avec l'intensité croissante du champ magnétique, tandis que $\theta p(L_I)$ passe à une température inférieure avec l'intensité croissante du champ magnétique.

Des études ont été menées sur deux autres alliages, $Co_{81.5}B_{18.5}$ et $Co_{83}B_{17}$, et les résultats indiquent que ce comportement anormal est une règle universelle pour le système d'alliage binaire Co-B. Avec l'augmentation de la teneur en Co, T0, θp(LI) et θp(LII) passent à des températures plus élevées et les constantes de Curie pour le liquide I et le liquide II diminuent. Sur la base du des coordonnées du point de transition structural liquid-liquide, une ligne guide est tracée au-dessus du liquidus dans le diagramme de phase Co-B, qui aura des implications significatives pour une mise en œuvre concrète de la fusion.

Chapter 5 Magnetic-field-induced chain-like assemblies of the primary phase during non-equilibrium solidification of a Co-B eutectic alloy: Experiments and modeling

5.1 Introduction

Processing metallic materials in an imposed strong magnetic field, as a cutting-edge technique, has attracted pronounced academic interest in the last few decades since a magnetic field of 10 T or higher becomes easily attainable with the development of superconducting technique [162]. A new research area called electromagnetic processing of materials has been considered to be a cutting-edge technique. When the material was processed under an imposed magnetic field, a variety of appealing phenomena, including magnetic orientation [147, 163, 164], levitation [165], strong magnetized liquid [82, 152], magneto-thermodynamics [76, 81], magneto-hydrodynamics [166], were reported. Furthermore, the magnetic field could be a powerful tool in tailoring the properties of materials by controlling the microstructure, grain size or even phase selection [167].

Xuan et al. [168] found that the formation of stray grains during directional solidification can be effectively suppressed by a high magnetic field, thus improving significantly the mechanical properties of the Ni-based single crystal superalloy. Hu et al. [169] reported that the magnetic field increases the macro segregation of primary silicon phase during direction solidification of a hypereutectic Al-Si alloy. Studies were conducted to show the effect of the high magnetic field on dendritic growth. The results indicated that the magnetic field significantly affected the orientation and destruction of the dendrites and even induced the transition from columnar to equiaxed dendrites [170-172]. These investigations [168-173] are focused on directional solidification.

Different from directional solidification, the heat and mass transportations are intrinsically different in the non-equilibrium process. The undercooled melt corresponds to a non-equilibrium state whose driving force for crystallization, i.e., the Gibbs free energy difference between the solid and liquid, increases with increasing undercooling. As a result, a number of possible solidification paths can occur due to the lower Gibbs free energy of metastable solids [174]. In this sense, the investigation of solidification of an undercooled melt with an imposed magnetic field is of tremendous importance from both the fundamental and practical points of view.

Hitherto, few studies have been carried out for non-equilibrium solidification of undercooled alloys under the magnetic field. Wei et al. [167] found that both undercooling and the magnetic field can affect the microstructures of the Cu-Co alloy. Without the magnetic field, the size of the spherical Co-rich phase increases with undercooling. Under a magnetic field of 6 T, the Co-rich particles are elongated along the direction of magnetic field and the volume fraction of the Co-rich phases reduces significantly. Wang et al. [174] reported that the mean undercooling of the undercooled Co-Sn melt is not altered by the homogeneous magnetic field but depressed by the gradient magnetic field. Furthermore, the critical undercooling for precipitation of the primary Co dendrite phase was found to be strongly affected by the external magnetic field [81].

The present work aims to investigate the effect of an external magnetic field of 4 T on the morphologies of the primary α-Co phase in undercooled Co-81.5at.%B eutectic alloy. The experiment results showed that the magnetic field had a great influence on the morphological alignment. Magnetic-field-induced chain-like assemblies of the primary α-Co phase were observed. A simple model was proposed to calculate the magnetic torque generated by an imposed magnetic field on a ferromagnetic body. The mechanism of morphological alignment was analyzed and discussed.

5.2 Experimental

Master alloys with a composition of Co-81.5at.%B were prepared by arc melting. The master alloy of about 25 g was machined into candidate samples with an average mass of about 1 g. One of them was analyzed by scanning electron microscope (SEM, VEGA II LMH) and X-ray diffraction (XRD, DX 2700) to show the microstructures for near-equilibrium solidification.

The undercooling experiments were conducted under a homogeneous magnetic field, where the field intensity is the maximum and no field gradient is present. More details on the experiments are available in chapter 2.

The as-solidified samples were prepared following standard metallographic procedures (i.e., hot mounting in resin, grinding in the sequence from 220# to 2000# sand papers and polishing). The microstructures were observed by a VEGA II LMH SEM instrument with the back-scattered electron (BSE) mode.

5.3 The effect of the magnetic field on the non-equilibrium solidification

5.3.1 Original microstructure and phase constituent

According to the phase diagram of the Co-B system [74], the Co-18.5at.%B alloy is at the equilibrium eutectic point and is constituted by the α-Co and β-Co_3B phases. Consequently, the master alloy used presently has a complete lamellar structure (Fig. 5.1a). Some of the α-Co phases are transformed into the ε-Co phases with a different crystal structure by a solid-state phase transformation, being consistent with the XRD patterns (Fig. 5.1b).

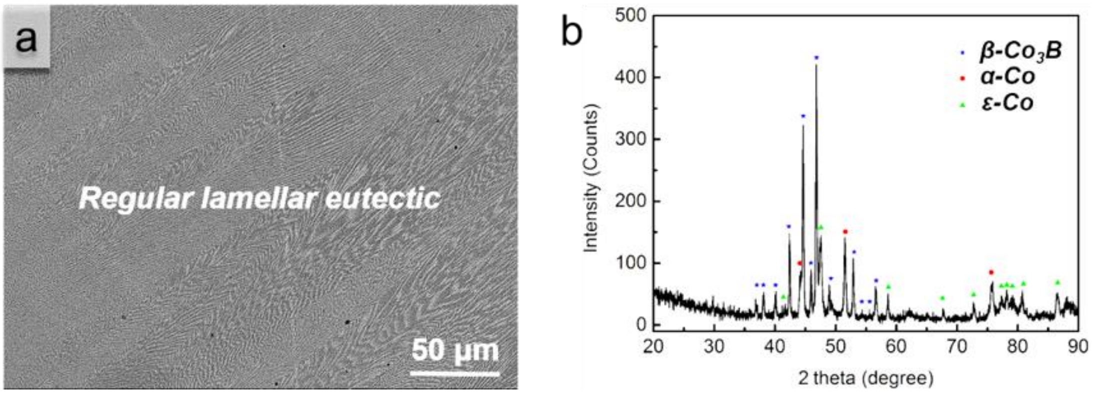

Fig. 5.1. (a) SEM image and (b) XRD patterns of the as solidified Co-81.5at.%B eutectic alloy.

5.3.2 Samples processed without an imposed magnetic field

Fig. 5.2 shows the microstructure of Co-81.5at.%B eutectic alloy solidified at various degree of undercooling. For ΔT=63 K, a small amount of coarse α-Co dendrites (light grey block) are surrounded by eutectic structures (grey region) and the lamellar eutectics are predominant; see Fig. 5.2a. In the case of ΔT=85 K, the volume fractions of primary α-Co dendrites and anomalous eutectics increase. However, the size of primary α-Co dendrites decreases slightly (Fig. 5.2b). When undercooling increases to about 110 K, the microstructure changes to a mixture of fine broken α-Co dendrites and anomalous eutectics; see Fig. 5.2c. The break of the primary dendrite can be attributed to re-melting during recalescence [175]. At the maximal undercooling obtained in the present work ΔT=204 K, fine anomalous eutectic colonies can be found (Fig. 5.2d). The edge of the eutectic colony is consisted by fine vermiculate α-Co crystals embedded in fine anomalous eutectic matrix, which is the same type of anomalous eutectic shown in Fig. 5.2c. A similar microstructure was found in the Co-20at.%Sn hypo-eutectic alloy [176].

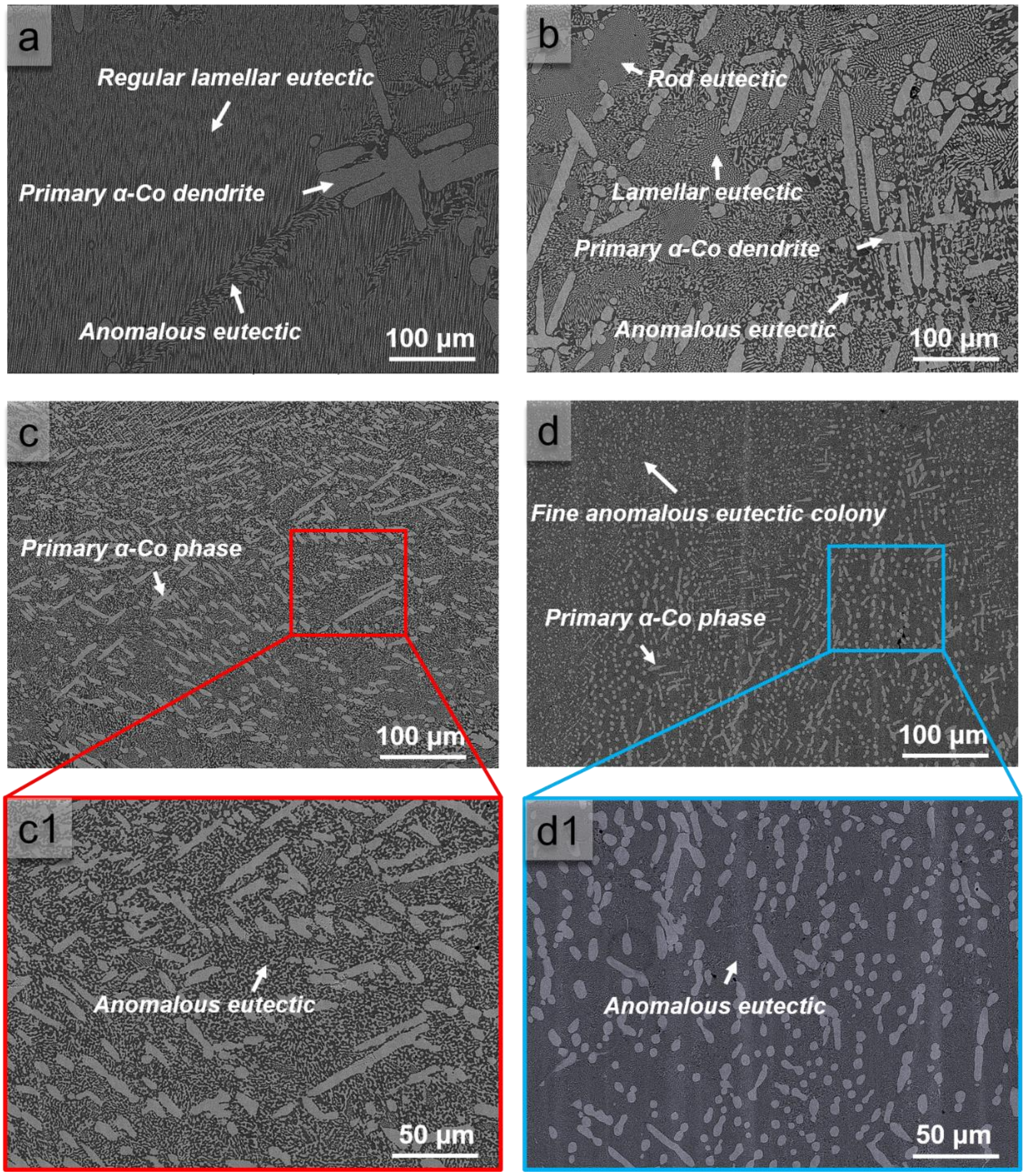

Fig. 5.2. Backscattered electron images of the Co-81.5at.%B eutectic alloys solidified with different undercooling: (a) ΔT=63 K, (b) ΔT=85 K, (c) ΔT=110 K and (d) ΔT=204 K. The magnified graphs corresponding to the square frames in Figs. 5.2c and 5.2d are shown in Figs. 5.2c1 and 5.2d1.

5.3.3 Samples processed under a magnetic field of 4T

Fig. 5.3 provides the representative backscattered electron images of undercooled Co-81.5at.%B eutectic alloys solidified under a magnetic field of 4 T. A clear alignment of the primary

α-Co phase is observed. Without a magnetic field, the primary α-Co phase (light grey block in Fig. 5.2) exhibits a disordered nature. After an application of a magnetic field of 4 T, the primary α-Co phase is aligned in such a way that the primary dendrite trunk of the α-Co phase is parallel to the magnetic field direction and tends to form a chain-like structure [177]; see Fig. 5.3a. With the increase of undercooling, part of the primary α-Co dendrites are broken and the magnetic field alignment is not remarkable (i.e., there is an angle difference between the primary dendrite trunk and the field direction); see Fig. 5.3c. As undercooling increases further, the primary α-Co dendrites are fully broken and the ellipsoidal primary α-Co particles are stacked as long chains along the direction of the applied magnetic field (Fig. 5.3e). Gaucherand et al. [80] observed a similar microstructure in the Co-B eutectic alloys with an external magnetic field of 3 T. At the maximal undercooling, ΔT=194 K, obtained in the present work, the morphology is not remarkably different from the sample solidified without the magnetic field (Fig. 5.2d), except that most of the primary α-Co particles within the anomalous eutectics colonies are self-organize as chain-like structures along the direction of external magnetic field; see Fig. 5.3g. Nevertheless, no clear alignment can be observed on the transverse sections, i.e., the primary α-Co phase distributes randomly through the whole samples, see Figs. 5.3b, 5.3d, 5.3f and 5.3h.

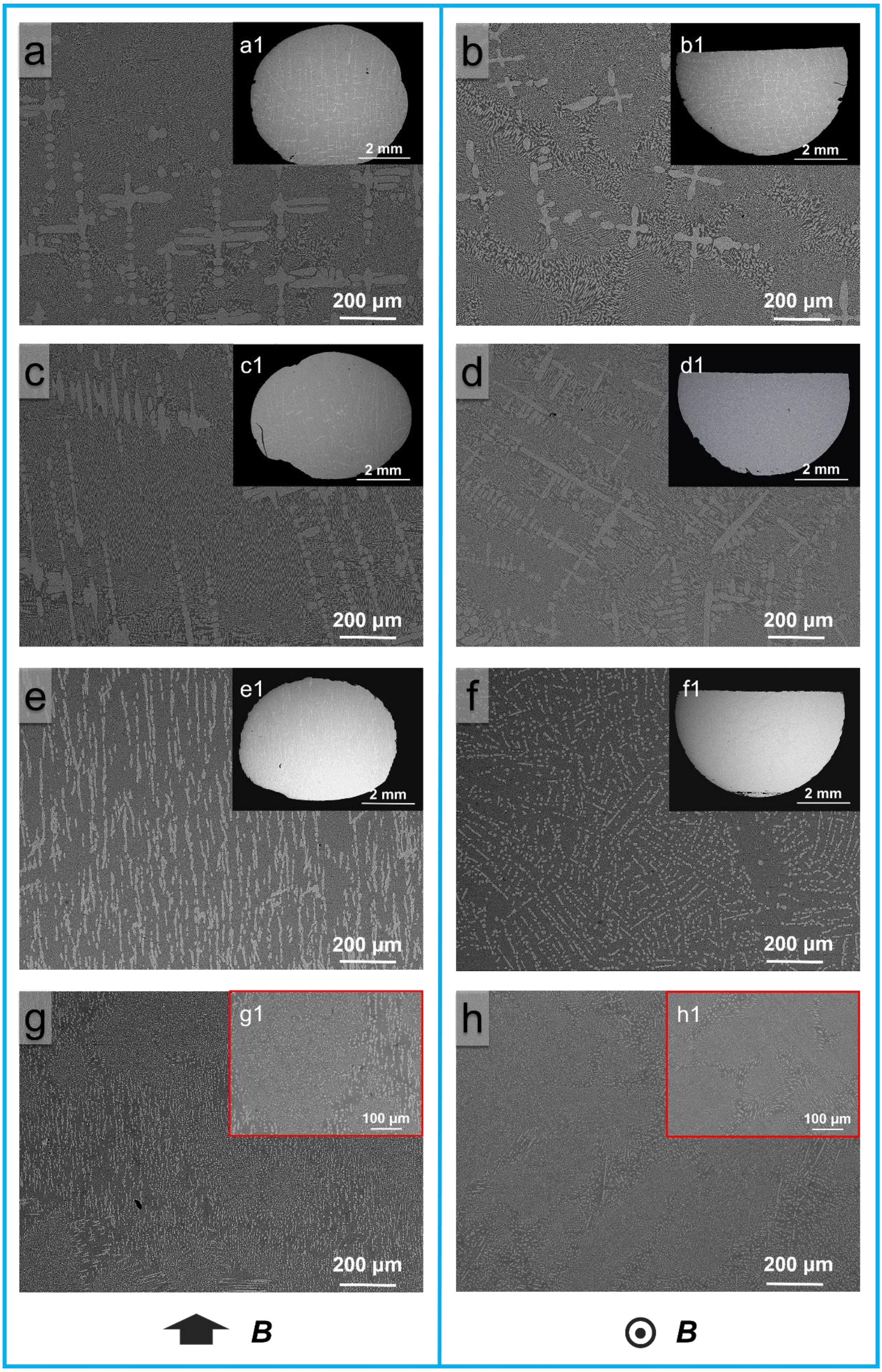

Fig. 5.3. Longitudinal (left, parallel to the direction of magnetic field) and transverse (right, perpendicular

to the direction of magnetic field) structures of Co-81.5at.%B eutectic alloys solidified under a magnetic field of 4 T with different undercooling: (a, b) ΔT=58 K, (c, d) ΔT=76 K, (e, f) ΔT=108 K and (g, h) ΔT=194 K. The corresponding macrostructures are shown as inserts Figs. 5.3a1-5.3f1. The inserts Figs. 5.3g1 and 5.3h1 are the magnified graphs of the fine anomalous eutectic colonies shown in Figs. 5.3g and 5.3h.

5.4 The mechanism of magnetic-field-induced chain-like assemblies of the primary phase

5.4.1 Magnetic alignment of the primary α-Co phase

To achieve magnetic alignment, a crystal needs to bear magnetic anisotropy. This means that the magnetic susceptibility is different in different crystal axes or dimensions [178]. The former, which corresponds to crystallographic alignment, is due to magneto crystalline anisotropy. The latter, which corresponds to morphological alignment, is ascribed to the shape anisotropy that results in the difference in the demagnetization factor [179]. When the anisotropic magnetic energy ΔE is higher than the thermal energy (i.e., $\Delta E > K_B T$, where K_B is the Boltzmann constant and T is the absolute temperature) [178], the magnetic torque exerted on this anisotropic crystal makes the crystal to follow a fixed orientation (e.g., the crystallite is aligned to their maximum magnetic susceptibility or the longest dimension parallel to the direction of the applied field), thus decreasing the magnetization energy [88].

The magnetization energy E for unit volume is given by [180]:

$$E = -\int_0^{H_a} \mu_0 M dH_a \tag{5.1}$$

where μ_0=4π·10^{-7} H m^{-1} is the magnetic constant, M is the magnetization and H_a is the imposed magnetic field.

For the non-magnetic materials ($|\chi| \ll 1$) such as diamagnetic ($\chi<0$) and paramagnetic ($\chi>0$) ones, the *M-H* curve is a linear one (see Fig. 5.4a) and the magnetization is related to the internal field by the susceptibility of the materials χ:

$$M=\chi H_i \tag{5.2}$$

The internal field H_i is consisted of the applied field H_a and the demagnetizing field H_d:

$$H_i = H_a + H_d \tag{5.3}$$

The demagnetizing field is related to the magnetization by a tensor n of demagnetization factors based on the body geometry:

$$H_d = -nM \tag{5.4}$$

Therefore, M can be expressed as:

$$M = \chi(1-n\chi)H_a \tag{5.5}$$

Then E is evaluated from Eqs. (5.1) and (5.5) as:

$$E_n = -\int_0^{H_a} \mu_0 \chi(1-n\chi)H_a dH_a = -\frac{1}{2}\mu_0\chi(1-n\chi)H_a^2 \tag{5.6}$$

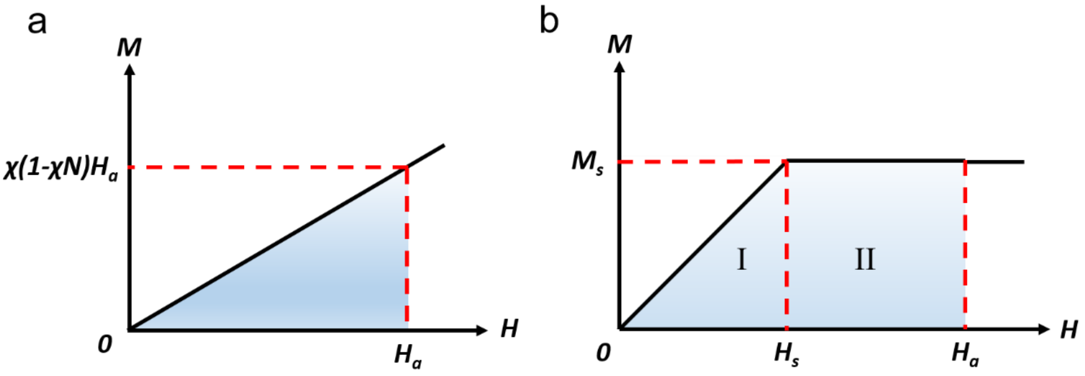

Fig. 5.4. *M-H* curves for (a) paramagnetic and (b) ferromagnetic material.

For the ferromagnetic materials ($|\chi| \gg 1$), the *M-H* curve is a non-linear one and the magnetization saturates at a certain magnetic intensity (see Fig. 5.4b). The magnetization curve can be divided into two distinct regions. In the first region (I), the magnetization grows non-linearly with the applied field until it reaches a saturation value. In the second region (II), the constant-magnitude saturated magnetization vector rotates toward to the applied field asymptotically as the field's strength increases. The approximate expression of E can be obtained by assuming that M is saturated at a certain magnetic intensity H_s, i.e., $H_S=nM_S$. And the magnetization M can be expressed as $M=H_a/n$ since the susceptibility $|\chi|\gg 1$. Therefore, E_f is given by:

$$\begin{aligned} E_f &= -\int_0^{H_a} \mu_0 M dH_a = -\int_0^{H_s} \mu_0 M dH_a - \int_{H_s}^{H_a} \mu_0 M_s dH_a \\ &= -\int_0^{H_s} \mu_0 \frac{H_a}{n} dH_a - \mu_0 M_s \left(H_a - H_s\right) \\ &= -\mu_0 \left(H_a - \frac{1}{2} n M_s\right) M_s \end{aligned} \tag{5.7}$$

According to a previous study [51], T_c of the α-Co phase in the near-equilibrium state for the Co-81.5at.%B eutectic alloys is about 1380 K, i.e., only 26 K smaller than the melting point T_m=1406 K. Consequently, the primary α-Co phases precipitated in this work are more likely to be in the ferromagnetic state rather than the paramagnetic state, even though T_c of the primary α-Co phase may decrease because the composition of soluble boron may increase with undercooling. To get direct evidences, magnetization during the heating and cooling processes is in-situ measured; see Fig. 5.5. It can be seen that for both cases (at modest and high undercooling), there is a significant increase in magnetization at the moment of nucleation, indicating that the precipitated primary α-Co phases are in the ferromagnetic state. Therefore, the anisotropic magnetic energy ΔE of the primary α-Co phases can be calculated using Eq. (5.7) as:

$$\Delta E = V\left|E_{f//} - E_{f\perp}\right| = \frac{1}{2}\mu_0 M_s^2 V\left|n_{//} - n_{\perp}\right| \tag{5.8}$$

where V is the volume of the primary crystal, $E_{f//}$ and $E_{f\perp}$ are the magnetization energy paralleling and perpendicular to the direction of applied field. To simplify the problem, the primary

α-Co phases are assumed to have the shape of an ellipsoid of revolution and the magnetization of them is saturated at the moment of nucleation under the magnetic field of 4 T. Assuming further $\left|n_{//}-n_{\perp}\right|$=1/2, the anisotropic magnetic energy ΔE can be estimated, i.e., $\Delta E = 5.24\times10^{-10}$ J, which is much larger than the thermal energy (K_BT is in a magnitude of 10^{-20} (SI unit)), indicating that magnetic alignment of the primary α-Co phases can be easily realized. The parameters used for the calculations are listed in Table 5.1.

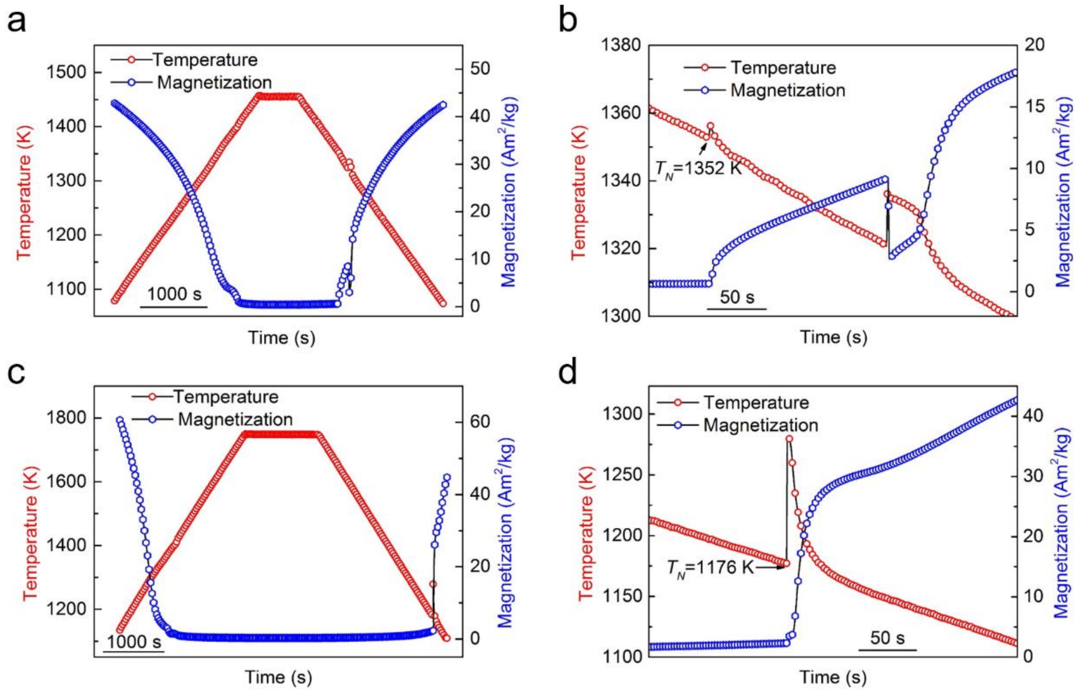

Fig. 5.5. The cooling and magnetization curves of Co-81.5at.%B eutectic alloy with different undercooling: (a) ΔT=54 K and (c) ΔT=230 K. Figs. 5.5b and 5.5d show the ranges around the nucleation temperature. The field intensity and gradient are 1.56 T and 23.235 T m^{-1}, respectively.

Table 5.1

Physical parameters used for calculating the anisotropic magnetic energy of the primary α-Co phases.

Property	Symbol	Si Unit	Value	Ref.
Saturation magnetization[2]	M_s	$Am^2\ kg^{-1}$	100	Evaluated from Fig. 5
Primary crystal volume	V	m^3	2.1×10^{-15}	Evaluated from Fig. 3
Density	ρ	$kg\ m^{-3}$	8.9×10^3	[181]

5.4.2 Rotation of the primary α-Co phase

The rotation of a crystal particle arises from the torque T caused by the imposed magnetic field. The general expression of T is [182]:

$$T = VM \times B \tag{5.9}$$

where B is the applied magnetic field. As mentioned above, for non-magnetic materials, the magnetization of the object is linearly related to the applied magnetic field intensity. Therefore, the resulting equation for the torque on the object in an applied field is straightforward. However, for the ferromagnetic materials, the magnetization is a nonlinear function of the applied magnetic field intensity, and the relation between the applied field and the resulting torque is nontrivial.

Hereinafter, the magnetic torque is taken into account by three different cases, i.e., an isotropic non-magnetic crystal in a homogeneous field, an anisotropic non-magnetic crystal in a homogeneous field and a ferromagnetic crystal in a homogeneous field.

For the isotropic non-magnetic particles, the torque is due to a non-uniform demagnetization

---

[2] The α-Co phase is the sole ferromagnetic phase (T_c of other phases are very low [153]) around the nucleation temperature range in this work, therefore the increase of the magnetization at the moment of nucleation (see Fig. 5.5) should come mainly from the nucleation of the α-Co phase. However, it should be noted that the magnetization shown in Fig. 5.5 is the average magnetization of the whole sample. Therefore, the mass fraction of the primary α-Co phases in the sample should be considered and the value is estimated around 5 % by analyzing the microstructures shown in Fig. 5.3. Then the saturation magnetization of the primary α-Co phase can be evaluated to be 20 times of the average magnetization shown in Fig. 5.5.

field and leads to the alignment of the longest dimension (which carries the maximum magnetization) along the direction of the applied field. The torque is given as [182]:

$$T = \frac{(1-3n)}{4}\chi^2 \frac{B^2}{\mu_0} V \sin(2\theta) \tag{5.10}$$

where θ is the angle between the principal axis of the cylinder and the direction of the applied magnetic field (see Fig. 5.6a). It should be noted that the demagnetization factors for general ellipsoidal bodies are constrained by the relation $n_x + n_y + n_z = 1$. For an axially symmetric body, the relation can be modified as $n_a + 2n_r = 1$. The axial demagnetization factor n_a for a prolate ellipsoid is given as [183]:

$$n_a = \frac{1}{R^2-1}\left(\frac{R}{2\sqrt{R^2-1}}\ln\left(\frac{R+\sqrt{R^2-1}}{R-\sqrt{R^2-1}}\right)-1\right) \tag{5.11}$$

where $R \geq 1$ is the ratio of long and short dimensions of the body.

For an anisotropic non-magnetic crystal, the direction, which carries the maximum magnetization (maximum magnetic susceptibility), aligns parallel with the direction of magnetic field. The torque is given by [182]:

$$T = \frac{1}{2}\Delta\chi \frac{B^2}{\mu_0} V \sin(2\theta) \tag{5.12}$$

where $\Delta\chi = \chi_1 - \chi_2$ (see Fig. 5.6b).

For a ferromagnetic crystal (see Fig. 5.6c), the magnetization of an ellipsoidal body is uniform throughout and always parallel to the direction of the internal field $\boldsymbol{H_i}$, which can be expressed as:

$$\begin{aligned} H_{ipara} &= H_a \cos\varphi - nM\cos\theta \\ H_{iprep} &= H_a \sin\varphi - \frac{1-n}{2} M \sin\theta \end{aligned} \tag{5.13}$$

When the field intensity is low enough such that $|M|<M_s$, i.e., $H_a<H_s$, the internal field $H_i=0$. Consequently, we have:

$$\tan\theta = \frac{2n}{1-n}\tan\varphi$$

$$M = H_a\sqrt{\left(\frac{\cos\varphi}{n}\right)^2 + \left(\frac{\sin\varphi}{(1-n)/2}\right)^2}$$

$$H_s = M_s \Big/ \sqrt{\left(\frac{\cos\varphi}{n}\right)^2 + \left(\frac{\sin\varphi}{(1-n)/2}\right)^2} \tag{5.14}$$

Therefore, the torque can be expressed analytically as:

$$\begin{aligned} T &= \mu_0 H_a M V \sin\alpha \\ &= \mu_0 H_a^2 V \sqrt{\left(\frac{\cos\varphi}{n}\right)^2 + \left(\frac{\sin\varphi}{(1-n)/2}\right)^2}\,\sin(\varphi-\theta) \\ &= \frac{1-3n}{2n(1-n)}\mu_0 H_a^2 V \sin 2\varphi \end{aligned} \tag{5.15}$$

The torque is quadratic in $|H_a|$, and is maximized when φ=45 °.

When the applied field is high enough such that $|M|=M_s$, i.e., $H_a \geq H_s$, the internal field $H_i>0$. As mentioned above, the magnetization $\boldsymbol{M}$ is always parallel to the direction of the internal field $\boldsymbol{H_i}$. Consequently, $\boldsymbol{M}\times\boldsymbol{H_i}=0$, i.e.,

$$\left(H_a\cos\varphi - nM_s\cos\theta\right)M_s\sin\theta - \left(H_a\sin\varphi - \frac{1-n}{2}M_s\sin\theta\right)M_s\cos\theta = 0 \tag{5.16}$$

Then, we have:

$$\sin\alpha = \frac{1-3n}{4}\frac{M_s}{H_a}\sin 2\theta \tag{5.17}$$

The torque can be expressed analytically as:

$$T = \frac{1-3n}{4}\mu_0 M_s^2 V \sin 2\theta \tag{5.18}$$

As can be seen from Eq. (5.17), the torque is not maximized when φ=45 °but when θ=45 °. The torque on the primary α-Co crystal can be calculated with a certain applied-field angle (e.g., φ=45 °) and a length-to-width ratio of R=4, which is evaluated from Fig. 5.3 (see Fig. 5.7a). In the low-field region ($H_a<H_s$), the torque increases with the magnetization vector until it saturates but the magnetization angle θ is locked. As the field increases beyond saturation ($H_a>H_s$), the magnitude of the torque saturates rapidly and the magnetization vector rotates toward to the applied field until it parallels to the direction of the applied field, i.e., $\theta \approx \varphi$ (see Fig. 5.7b).

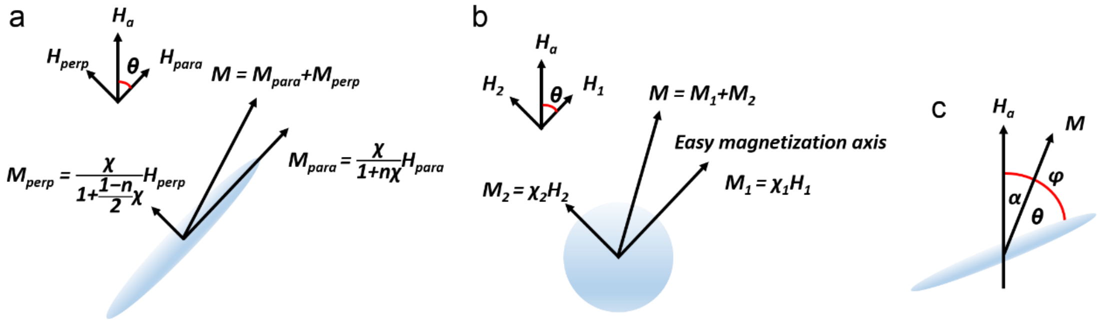

Fig. 5.6. Schematic diagrams of (a) an isotropic non-magnetic crystal in a homogeneous field, (b) an anisotropic non-magnetic crystal in a homogeneous field and (c) a ferromagnetic crystal in a homogeneous field.

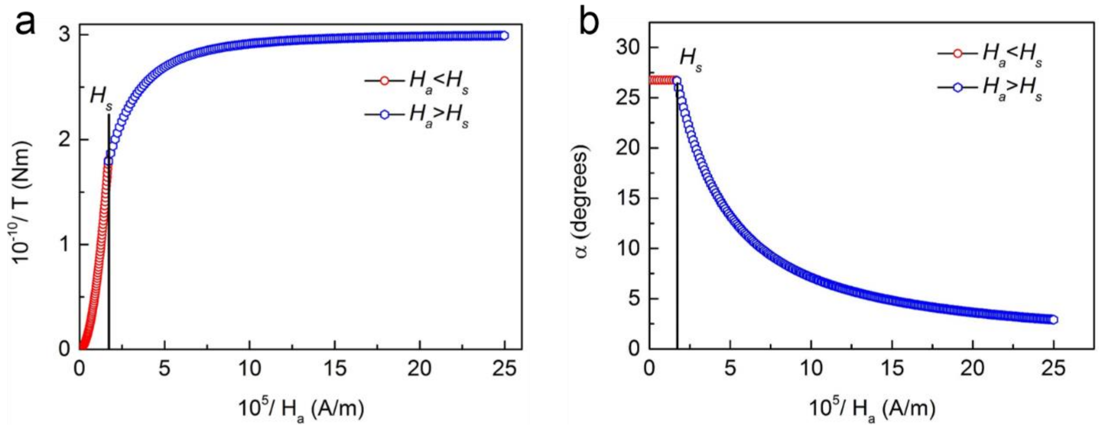

Fig. 5.7. (a) The magnetic torque of the primary α-Co crystal versus the applied filed intensity. (b) The angle between the applied field and the predicted magnetization versus the applied filed intensity.

When a particle rotates in a liquid, the liquid viscosity induces a rotating torque T_v that prevents its rotation, and T_v is proportional to the rotation speed [182]:

$$T_v = -\xi\left(d\alpha / dt\right) \tag{5.19}$$

For ellipsoid particles, ξ is given as [182]:

$$\xi = 2\pi\eta L^3 \big/ \left(6\ln R - 3\right) \tag{5.20}$$

where η is the viscosity of the fluid, L is the length of the particle. In the low-field region, the magnetization vector increases without rotation until it saturates. As the field increases to a critical value, the magnetization vector rotates toward to the applied field. The rotation time t in the high-field region ($H_a > H_s$) can be expressed as:

$$t = \tau \ln\left(\tan\left(\frac{\alpha_0}{2}\right) \Big/ \tan\left(\frac{\alpha}{2}\right) \right) \tag{5.21}$$

where α_0 is the starting angle, α is the angle at time t and τ is a characteristic orientation time. In this case, τ is found to be:

$$\tau = \xi / \mu_0 M_s H_a V \tag{5.22}$$

The rotation time t defined as the interval time that it takes for the particle to rotate from α_0=89 °to α=1 ° are shown in Fig. 5.8. The parameters used are listed in Table 5.2. The time needed for a saturated α-Co particle to rotate is negligible as compared with the crystallization time (see Fig. 5.5), indicating that magnetic alignment can be easily realized.

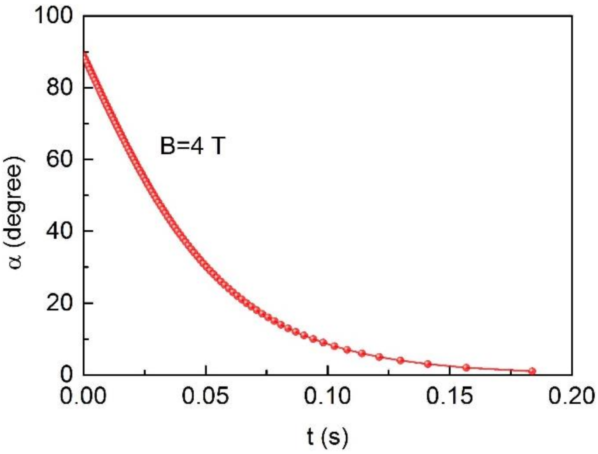

Fig. 5.8. Rotation of the saturated α-Co particles. The angle between the applied magnetic field and the magnetization vector is plotted as a function of time.

Table 5.2

Physical parameters used for calculating the rotation time of a saturated α-Co particle.

Property	Symbol	Si Unit	Value	Ref.
Viscosity	η	Pa s	1.35×10^{-2}	[184]
Length	L	m	8×10^{-5}	Evaluated from Fig. 5.3

5.4.3 Formation of the chain-like structures for the primary α-Co phase

Under a strong magnetic field, the primary α-Co particle in the liquid matrix is magnetized. If the magnetization is strong enough, large magnetic forces may develop at the tip and hence make the solidifying Co to form as long needles [88]. The magnetization results (see Fig. 5.5) indicate that the primary α-Co phases are strongly magnetized and could form small magnets, which are similar with the axial magnets, with an imposed magnetic field. This will generate attractive force along the field direction and repulsive force in the direction perpendicular to the field direction between neighboring α-Co phases [177]. With the aid of these two interactions, the α-Co particles attracted and repelled each other and tend to trap other α-Co particles on either top or bottom magnetic pole, i.e., to self-organize as chain-like stacking. In addition, as the most energetically favorable particles distribution, the chain-like stacking (for which n=0) has the minimal demagnetizing energy ($\mu_0 n M^2/2$ per unit volume) [80].

In order to better understand the phenomenon that the primary α-Co particles self-organize as chain-like stacking, a quantitative analysis was carried out. The force created by a moment m_1 (one α-Co particle) on the moment m_2 (another α-Co particle) at a distance r_{12} is given as [185]:

$$\vec{F}_{1\to2}=\frac{\mu_0}{4\pi}\left[\frac{3(\vec{m}_2\cdot\vec{r}_{12})\cdot\vec{m}_1+3(\vec{m}_1\cdot\vec{r}_{12})\cdot\vec{m}_2+3(\vec{m}_1\cdot\vec{m}_2)\cdot\vec{r}_{12}}{r_{12}^5}-\frac{15(\vec{m}_1\cdot\vec{r}_{12})(\vec{m}_2\cdot\vec{r}_{12})\cdot\vec{r}_{12}}{r_{12}^7}\right] \tag{5.23}$$

With all moments paralleling to the direction of the applied magnetic field and having the same value, the force expression is simplified using the polar coordinates system:

$$\vec{F}_{1\to 2}=\frac{3m^2\mu_0}{4\pi}\left[\frac{\sin(2\omega)\vec{\mu}_\theta+(1-3\cos^2(\omega))\vec{\mu}_r}{r_{12}^4}\right] \tag{5.24}$$

where ω is the angle between the magnetic field direction and the inter-particle vector. $\vec{\mu}_r$ is a unit vector in the direction of r and $\vec{\mu}_\theta$ is a unit vector normal to the direction of r. The magnetic moment m is given as:

$$m = MV \tag{5.25}$$

In the present case, the α-Co particles are approximated as spheres in order to simplify the calculations. Dependence of the forces on the radial and angular components is plotted in Fig. 5.9a, and on the vectorial equivalent is shown in Fig. 5.9b. As shown in Fig. 5.9b, a saturated α-Co particle tends to attract the two closest particles, leading to an aligned chain-like stacking since the maximum force is located in the line that goes though the particle and parallel to the magnetic field direction. The force generated perpendicular to the magnetic field direction makes two particles repel each other. The calculation results are consistent with the experiment ones (see Fig. 5.3), i.e., the primary α-Co phases are stacked as long divided chains along the applied field.

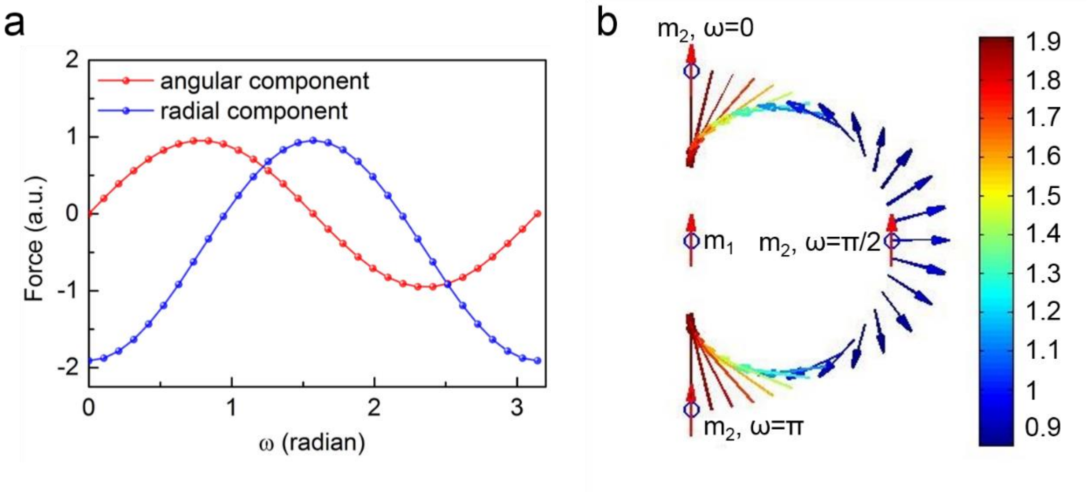

Fig. 5.9. Angular dependence of dipole-dipole force: (a) the blue line represents the radial component and the red line represents the angular component, and (b) the force is plotted with

different position of the second particle. The color-bar denotes the relative magnitude of the force.

However, to self-organize as chain-like stacking, the α-Co particles need to move through the viscous melt. According to the Stokes's law [186], a fluid drag force will produce by the viscous melt and opposes the movement. The force is given as:

$$F = 6\pi\eta rv \tag{5.26}$$

where r is the radius of the spherical particle and v is the flow velocity relative to the particle. The dependence of the velocity v on the angular ω and distance r_{12} are shown in Fig. 5.10. For a saturated α-Co particle, the neighbor saturated α-Co particles are much easier to migrate to either the top or bottom of the particle, i.e., to self-organize as chain-like stacking.

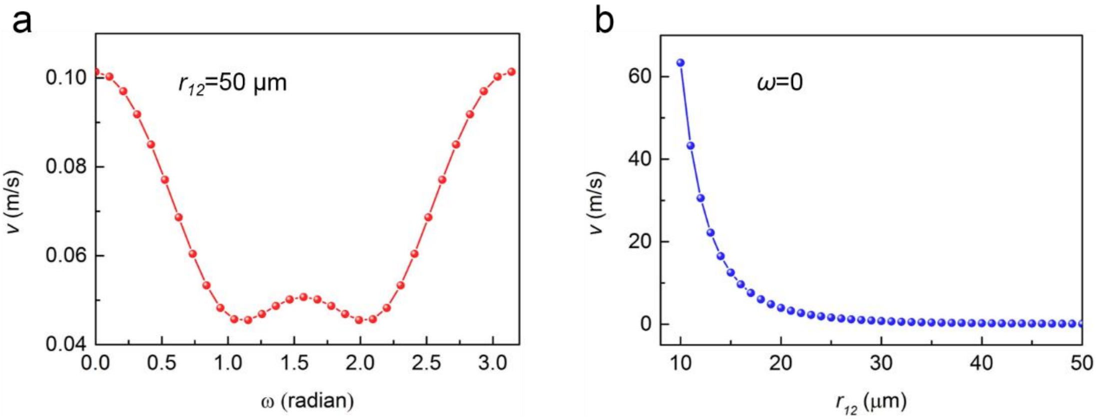

Fig. 5.10. The dependence of the velocity v on the angular ω and distance r_{12}. The radius of the particle is set to be r=13 μm.

5.4.4 Favored morphology of the primary α-Co phase

As shown in Figs. 5.2 and 5.3, the appearance of the primary α-Co phases are rod-like and spherical at relatively high undercooling, and the application of magnetic field is more conducive to obtain such kind of α-Co phases. Without the magnetic field, the primary α-Co dendrites are still visible at ΔT=110 K, even though some of them are ruptured because of re-melting during recalescence; see Fig. 5.2c. Under an imposed magnetic field, only rod-like and spherical primary α-Co phases can be found at similar undercooling, see Figs. 5.3e and 5.3f. Li et al. [187] investigated the nucleation and growth behaviors of the primary Al_2Cu phases in the Al-Cu hypereutectic alloy under a magnetic field by differential thermal analysis. The obtained microstructures solidified with and without magnetic fields showed a similar discipline. Typical dendrite morphologies of primary Al_2Cu phases were observed for the case without magnetic field, whereas, the appearance of primary Al_2Cu phases were inclined to be rod-like and spherical for the case with an imposed magnetic field. The tendency of the primary Al_2Cu phases to be rod-like and spherical became more obvious with the increase of the magnetic field intensity, indicating that the morphology of the precipitated phase can be altered when a magnetic field is applied.

When a magnetic body is placed in a uniform magnetic field, a demagnetizing magnetic field will generate inside. The direction of the demagnetizing magnetic field is opposite to the direction of the applied field [188]. The appearance of the primary α-Co phases tends to be rod-like and spherical in order to reduce the demagnetizing energy ($\mu_0 n M^2 / 2$). For a sphere, n=1/3. For a long cylinder, $n = 0$ when $\overrightarrow{M}$ is along length, and n=1/2 when $\overrightarrow{M}$ is along the width.

In addition, the thermoelectric magnetic forces (TEMF) [189] produced by the interaction between the thermoelectric currents and the applied magnetic field may also attribute to the fragmentation of the primary α-Co dendrites. Lu et al. [170] attributed the destruction of the primary dendrite to the TEMF by measuring the Seebeck voltage near the liquid-solid interface. TEMF in the solid Al_2Cu column was simulated by Wang et al. [190], and the results indicated that a torque can form on the column due to the TEMF. This torque would fragment the continuously grown column and respond to the refinement. Therefore, compare with the case without the magnetic field, the primary α-Co dendrites under a magnetic field are more apt to fragment and hence to be rod-like and spherical.

5.5 Summary

Effect of a high magnetic field on the morphology and alignment of the primary phase in the Co-81.5at.%B eutectic alloy during non-equilibrium solidification has been investigated experimentally. The following conclusions can be drawn.

(1) The field-cooled samples exhibit long primary Co-dendrites with their primary dendrite trunk aligned parallel to the magnetic field at relative low undercooling and ellipsoidal primary Co particles with their long axis aligned parallel to the applied field at relative high undercooling. The shape effect should be responsible for this morphological alignment.

(2) The Co particles are stacked as long chains along the applied field, however, randomly dispersed in the zero field solidified samples. This chain-like stacking structure is a consequence of the particle to particle interactions.

(3) The favored appearance of the primary α-Co phases are rod-like or spherical at relatively high undercooling, and the application of magnetic field is more conducive to obtain such kind of α-Co phases.

5.5 Résumé

L'effet d'un champ magnétique intense sur la morphologie et l'alignement de la phase primaire de l'alliage eutectique Co-81.5at.%B pendant la solidification hors équilibre a été étudié expérimentalement. Les conclusions suivantes peuvent être tirées.

(1) Les échantillons refroidis sous champ présentent des dendrites primaires de Cobalt

allongées avec leur tronc de dendrite primaire aligné parallèlement au champ magnétique pour un sous-refroidissement relativement faible, et des particules primaires de Co ellipsoïdales avec leur axe long aligné parallèlement au champ appliqué pour un sous-refroidissement relativement élevé. L'effet de forme devrait être responsable de cet alignement morphologique.

(2) Les particules de Co sont empilées en longues chaînes le long du champ appliqué, mais dispersées au hasard dans les échantillons solidifiés sous champ nul. Cette structure d'empilement en chaîne est due aux interactions de particule à particule.

(3) L'aspect préférentiel des phases primaires de Cobalt α est en forme de tige ou sphérique avec un sous-refroidissement relativement élevé, et l'application d'un champ magnétique favorise la formation de ces phases de Cobalt α.

Chapter 6 Conclusions and Perspectives

6.1 Conclusions

In the present work, a thorough investigation has been conducted on the Co-B alloys in terms of the microstructure evolution during non-equilibrium solidification with/without magnetic field and the temperature induced liquid-liquid structure transition. From the experimental and calculation results of the present work, following main conclusions can be drawn:

Microstructure evolution and phase selection in the undercooled hypereutectic Co-20at.%B alloy

A transition from hypereutectic to hypoeutectic was found at a critical undercooling of 119 K, i.e., phase selection between the α-Co and the β-Co_3B phase occurs in the undercooled Co-20at.%B hypereutectic alloy. When ΔT <119 K, the morphologies of the undercooled Co-20at.%B alloy are characterized by a primary directional dendritic structure of β-Co_3B phase surrounded by the α-Co+β-Co_3B regular lamellar eutectics. When ΔT >119 K, the above hypereutectic microstructure is replaced by the hypoeutectic microstructure with the α-Co phase as the primary phase.

From the calculation results of the critical works for nucleation of the α-Co and β-Co_3B phase in the Co-20at.%B hypereutectic alloy, the critical work for nucleation of the β-Co_3B phase is always smaller than that of the α-Co phase, indicating that the β-Co_3B phase should be the preferred nucleation phase over the whole range of undercooling. The successful formation of an effective nucleus, however, does not mean that micronucleus can definitely grow into a macro crystal.

The growth velocities of the α-Co and β-Co_3B phases in the undercooled Co-20at.%B hypereutectic alloy have been calculated according to the LKT/BCT model. It was found that the preferred nucleation phase is not always the faster growing phase with the increase of undercooling. The β-Co_3B phase has a prior nucleation over that of α-Co phase at low undercooling. However, the growth velocity of the β-Co_3B phase is far lower than that of α-Co phase when ΔT>122 K, indicating that phase selection between the α-Co and β-Co_3B phases is growth-controlled.

Temperature induced liquid-liquid structure transition in Co-B alloys

Through utilizing the cyclic superheating and cooling as well as DSC measurements, the overheating dependent undercooling in the Co-B alloys were studied. For each alloy, there is a critical overheating temperature T_c^0 at which there is a sharp increase of the meaning undercooling, i.e., below (above) T_c^0; the mean undercooling is about 80 ℃ (200 ℃). The critical overheating temperature is 1360 ℃ for the hypereutectic $Co_{80}B_{20}$ alloy, 1380 ℃ for the eutectic $Co_{81.5}B_{18.5}$ alloy, and 1390 ℃ for the hypoeutectic $Co_{83}B_{17}$ alloy.

DSC measurements show that there is a thermal absorption peak in the heating process above the melting temperature or the *liquidus* temperature, the peak temperature of which is nearly equal to the overheating temperature, indicating that the temperature-induced L-LST does occur when the overheating temperature is above the critical overheating temperature and it should relate highly to nucleation in the undercooled Co-B eutectic melts. L-LST is not dependent on the heating and cooling rates and is irreversible.

The effect of L-LST on nucleation is interpreted by the recent nucleation theory that considers the structure of overheated melts, according to which the second melting temperature T_{m2} can be calculated and is nearly equal to the critical overheating temperature T_c^0, indicating that the tiny crystals that can be survival above to T_{m2} is highly related to L-LST. This work provides further evidences for L-LST and is helpful for our understanding of solidification in undercooled melts.

By in-situ measuring the magnetization, the temperature induced liquid-liquid structure transition was further investigated. A magnetization anomaly in term of the non-Curie-Weiss temperature dependence of magnetization was observed in the overheated state, demonstrating a temperature induced liquid-liquid structure transition. This anomalous behavior was found to be a universal formula for the Co-B binary alloy system. A transition point (T_0) and two paramagnetic Curie temperatures ($\theta(\mathrm{L_I})$, $\theta(\mathrm{L_{II}})$) corresponding to two different structures of the liquids are determined. The effects of magnetic field intensity on the liquid-liquid structure transition and paramagnetic Curie temperatures are studied. T_0 and $\theta(\mathrm{L_{II}})$ are found not sensitive to the field intensity, whereas, $\theta(\mathrm{L_I})$ shifts to lower temperatures with the increasing magnetic field intensity. With the increased concentration of Co, T_0, $\theta(\mathrm{L_I})$ and $\theta(\mathrm{L_{II}})$ shift to higher temperatures and the Curie constants for the liquid I and liquid II decrease. Based on the location of T_0, a guideline was drawn above the *liquidus* in the Co-B phase diagram, which could provide a significant guidance to the practical melt treatment.

Magnetic-field-induced chain-like assemblies of the primary phase during non-equilibrium solidification

The field-cooled samples exhibit long primary Co-dendrites with their primary dendrite trunk aligned parallel to the magnetic field at relative low undercooling and ellipsoidal primary Co particles with their long axis aligned parallel to the applied field at relative high undercooling. The shape effect should be responsible for this morphological alignment.

The Co particles are stacked as long chains along the applied field, however, randomly dispersed in the zero field solidified samples. This chain-like stacking structure is a consequence of the particle to particle interactions.

The favored appearance of the primary α-Co phases are rod-like and spherical at relatively high undercooling, and the application of magnetic field is more conducive to obtain such kind of α-Co phases.

6.2 Perspectives

In this PhD work, a thoroughly study was conducted on the Co-B alloys in terms of the microstructure evolution during non-equilibrium solidification with/without magnetic field. Meanwhile, the temperature induced liquid-liquid structure transition behavior was characterized. Comprehensive information concerning these fundamental issues was obtained for the Co-B alloys, opening new perspectives on further investigations of this alloy system and can be summarized as follows:

1) For the temperature induced liquid-liquid structure transition, the present work mainly focused on the detection and characterization of the transition behavior, the effects of the magnetic field intensity on the LLST and paramagnetic curie temperatures and the composition dependent characteristic transition temperatures. However, a more in depth analysis of the locally favored structures and their stability and transition process still need to be explored.

2) The present work shows the microstructure evolution processes are affected by magnetic field depending on the field intensity and undercooling. With stronger magnetic field up to 25 T, the thermal and solute convection in the melt are influenced more drastically. Therefore, the microstructure evolution processes must be different and need to be studied to improve our knowledge.

6.3 Conclusions et perspectives

Dans le cadre du présent travail, une étude approfondie a été menée sur les alliages Co-B en termes d'évolution de la microstructure lors d'une solidification hors équilibre avec/sans champ magnétique et de la transition liquide-liquide induite par la température. Les résultats expérimentaux et numériques permettent de tirer les principales conclusions suivantes :

Evolution de la microstructure et sélection de phase dans l'alliage hypereutectique sous-refroidi Co-20at.%B

Une transition de l'hypereutectique à l'hypoeutectique a été observée à un sous-refroidissement critique de 119 K: une sélection de phase entre la phase α-Co et la phase β-Co_3B se produit dans l'alliage hypereutectique Co-20at.%B sous refroidi. Lorsque ΔT <119 K, les morphologies de l'alliage Co-20at.%B sous-refroidi sont caractérisées par une structure dendritique directionnelle primaire de phase β-Co_3B entourée par l'eutectique lamellaire régulier α-Co+β-Co_3B. Lorsque ΔT >119 K, la microstructure hypereutectique ci-dessus est remplacée par la microstructure hypoeutectique avec la phase α-Co comme phase primaire.

D'après les résultats des calculs des travaux critiques pour la nucléation de la phase α-Co et β-Co_3B dans l'alliage hypereutectique Co-20at.%B, le travail critique pour la nucléation de la phase β-Co_3B est toujours inférieur à celui de la phase α-Co, indiquant que la phase β-Co_3B devrait être la phase de nucléation préférentielle sur toute la plage du sous refroidissement. La formation réussie d'un noyau critique ne signifie toutefois pas que ce micro-noyau puisse se transformer en macro-cristal. Les vitesses de croissance des phases α-Co et β-Co_3B dans l'alliage hypereutectique Co-20at.%B sous-refroidi ont été calculées selon le modèle LKT/BCT. On a constaté que la phase de nucléation préférentielle n'est pas toujours la phase de croissance plus rapide avec l'augmentation du sous-refroidissement. La phase β-Co_3B a une nucléation antérieure à celle de la phase α-Co à faible sous-refroidissement. Cependant, la vitesse de croissance de la phase β-Co_3B est bien inférieure à celle de la phase α-Co lorsque ΔT>122 K, indiquant que la sélection de phase entre les phases α-Co et β-Co_3B est contrôlée par la vitesse de croissance.

Transition structurale liquide-liquide induite par la température dans les alliages Co-B

En utilisant les mesures de surchauffe et de refroidissement cycliques ainsi que les mesures DSC, on a étudié la dépendance du sous-refroidissement en fonction de la surchauffe dans les alliages Co-B. Pour chaque alliage, il y a une température critique de surchauffe T_c^0 au-dessus de laquelle il y a une brusque augmentation du sous-refroidissement moyen, c'est-à-dire passant de 80 °C pour une surchauffe inférieure T_c^0, à 200 °C pour une surchauffe supérieure à T_c^0. La température critique de surchauffe est de 1360 °C pour l'alliage hypereutectique $Co_{80}B_{20}$, 1380 °C pour l'alliage eutectique $Co_{81.5}B_{18.5}$ et 1390 °C pour l'alliage hypoeutectique $Co_{83}B_{17}$.

Les mesures DSC montrent qu'il y a un pic d'absorption thermique dans le processus de chauffage au-dessus de la température de fusion ou de la température du liquidus, dont la température maximale est presque égale à la température de surchauffe, ce qui indique que la transition structurale liquide-liquide induite par la température se produit lorsque la température de surchauffe est supérieure à la température critique de surchauffe et que celle-ci doit être étroutement liée à la nucléation dans les liquides eutectiques Co-B sous refroidis. Cette transition structurale liquide-liquide ne dépend pas des vitesses de chauffage et de refroidissement et est irréversible.

L'effet de la transition structurale liquide-liquide sur la nucléation est interprété par la théorie récente de la nucléation qui considère la structure des métaux liquides surchauffés, selon laquelle une seconde température de fusion T_m^2 peut être calculée et est presque égale à la température critique de surchauffe T_c^0, indiquant que la survie de petits cristaux au-dessus de T_m^2 est fortement liée à la transition structurale liquide-liquide. Ce travail fournit d'autres preuves de la transition structurale liquide-liquide et est utile pour notre compréhension de la solidification dans les métaux liquides sous-refroidis.

En mesurant in situ l'aimantation, la transition de la structure liquide-liquide induite par la température a été étudiée plus en détail. Une anomalie d'aimantation, en termes de non dépendance en température de la loi de Curie-Weiss a été observée à l'état surchauffé, ce qui démontre une transition structurale liquide-liquide induite par la température. Ce comportement anormal s'est avéré être une règle universelle pour le système binaire Co-B. Un point de transition (T_0) et deux températures paramagnétiques de Curie ($\theta(L_I)$, $\theta(L_{II})$) correspondant à deux structures différentes des liquides sont déterminés. Les effets de l'intensité du champ magnétique sur la transition liquide-liquide et les températures paramagnétiques de Curie sont étudiés. T_0 et $\theta(L_{II})$ ne sont pas sensibles à l'intensité du champ, tandis que $\theta(L_I)$ passe à des températures plus basses avec l'intensité croissante du champ magnétique. Avec l'augmentation de la concentration en Cobalt, T_0, $\theta(L_I)$ et $\theta(L_{II})$ passent à des températures plus élevées et les constantes de Curie pour le liquide I et le liquide II diminuent. En se basant sur l'emplacement de T_0, une ligne directrice a été tracée au-dessus du liquidus dans le diagramme de phase Co-B, ce qui pourrait fournir une aide importante pour le traitement pratique de la fusion.

Assemblages en chaîne induits par champ magnétique de la phase primaire pendant la solidification hors équilibre

Les échantillons refroidis sous champ présentent des co-dendrites primaires longues avec leur tronc de dendrite primaire aligné parallèlement au champ magnétique pour un sous-refroidissement relativement faible et des particules primaires de Co ellipsoïdales avec leur axe long aligné parallèlement au champ appliqué pour un sous-refroidissement relativement élevé. L'effet de forme devrait être responsable de cet alignement morphologique.

Les particules de Cobalt sont empilées en longues chaînes le long du champ appliqué, mais dispersées au hasard dans les échantillons solidifiés en champ nul. Cette structure d'empilement en chaîne est une conséquence des interactions de particule à particule.

L'aspect préférentiel des phases primaires de α-Co est en forme de tige ou sphérique pour un sous-refroidissement relativement élevé, et l'application d'un champ magnétique favorise l'obtention de ce type de phases de Cobalt α.

Dans ce travail de thèse, une étude approfondie a été menée sur les alliages Co-B en termes d'évolution de la microstructure lors d'une solidification hors équilibre avec ou sans champ magnétique. Le comportement de transition de la structure liquide-liquide induite par la température a été caractérisé. Des informations complètes sur ces questions fondamentales ont été obtenues pour les alliages Co-B, ouvrant de nouvelles perspectives pour les études ultérieures de ce système d'alliages et peuvent être résumées comme suit:

1) Pour la transition de structure liquide-liquide induite par la température, le présent travail s'est principalement concentré sur la détection et la caractérisation du comportement de transition, les effets de l'intensité du champ magnétique sur les températures de transition structurale liquide-liquide et les lois de Curie paramagnétique ainsi que sur la dépendance en températures de ces transitions. Toutefois, une analyse plus approfondie des structures locales privilégiées, de leur stabilité et de leur processus de transition doit encore être explorée.

2) Le présent travail montre que les processus d'évolution de la microstructure sont influencés par le champ magnétique et dépendent de l'intensité du champ et du sous-refroidissement. Avec un

champ magnétique intense jusqu'à 25 T, la convection thermique et la convection du soluté dans l'alliage fondu sont plus fortement influencées. Par conséquent, les processus d'évolution de la microstructure sont certainement différents et doivent être étudiés pour améliorer notre connaissance du système.

References

[1] M. Stolpe, I. Jonas, S. Wei, Z. Evenson, W. Hembree, F. Yang, A. Meyer, R. Busch, Structural changes during a liquid-liquid transition in the deeply undercooled $Zr_{58.5}Cu_{15.6}Ni_{12.8}Al_{10.3}Nb_{2.8}$ bulk metallic glass forming melt, Physical Review B 93(1) (2016) 014201.

[2] J. Russo, H. Tanaka, Crystal nucleation as the ordering of multiple order parameters, The Journal of Chemical Physics 145(21) (2016) 211801.

[3] S. Lan, M. Blodgett, K.F. Kelton, J.L. Ma, J. Fan, X.-L. Wang, Structural crossover in a supercooled metallic liquid and the link to a liquid-to-liquid phase transition, Applied Physics Letters 108(21) (2016) 211907.

[4] M. Kobayashi, H. Tanaka, The reversibility and first-order nature of liquid-liquid transition in a molecular liquid, Nature communications 7 (2016) 13438.

[5] M. Li, P. Jia, R. Liu, H. Geng, S. Du, M. Wang, H. Luo, S. Lu, The Effect of Melt Overheating on the Melt Structure Transition and Solidified Structures of Al-La Alloy, JOM 67(5) (2015) 948-954.

[6] K. Georgarakis, L. Hennet, G.A. Evangelakis, J. Antonowicz, G.B. Bokas, V. Honkimaki, A. Bytchkov, M.W. Chen, A.R. Yavari, Probing the structure of a liquid metal during vitrification, Acta Materialia 87 (2015) 174-186.

[7] M.J. Caturla, J.-Z. Jiang, E. Louis, J.M. Molina, Some Issues in Liquid Metals Research, Metals 5(4) (2015) 2128-2133.

[8] N. Mauro, M. Blodgett, M. Johnson, A. Vogt, K. Kelton, A structural signature of liquid fragility, Nature communications 5 (2014) 4616.

[9] K.F. Kelton, G.W. Lee, A.K. Gangopadhyay, R.W. Hyers, T.J. Rathz, J.R. Rogers, M.B. Robinson, D.S. Robinson, First X-Ray Scattering Studies on Electrostatically Levitated Metallic Liquids: Demonstrated Influence of Local Icosahedral Order on the Nucleation Barrier, Physical review letters 90(19) (2003) 195504.

[10] F.-Q. Zu, J. Chen, X.-F. Li, L.-N. Mao, Y.-C. Liu, A new viewpoint to the mechanism for the effects of melt overheating on solidification of Pb-Bi alloys, Journal of Materials Research 24(07) (2011) 2378-2384.

[11] J.J.Z. Li, W.K. Rhim, C.P. Kim, K. Samwer, W.L. Johnson, Evidence for a liquid-liquid phase transition in metallic fluids observed by electrostatic levitation, Acta Materialia 59(5) (2011) 2166-2171.

[12] X. Li, F. Zhang, F. Zu, X. Lv, Z. Zhao, D. Yang, Effect of liquid-liquid structure transition on solidification and wettability of Sn-0.7Cu solder, Journal of Alloys and Compounds 505(2) (2010) 472-475.

[13] H. Geng, G. Zhang, Z. Wang, Y. Deng, H. Qin, Density-temperature properties of Ga-Sb alloy melt, Applied Physics A 98(1) (2010) 227-232.

[14] G. Li, Q. Wang, D. Li, X. Lü, J. He, Structure evolution during the cooling and coalesced cooling processes of Cu-Co bimetallic clusters, Physics Letters A 372(45) (2008) 6764-6769.

[15] R.F. Tournier, Predicting glass-to-glass and liquid-to-liquid phase transitions in supercooled water using classical nucleation theory, Chemical Physics 500 (2018) 45-53.

[16] H. Tanaka, General view of a liquid-liquid phase transition, Physical Review E 62(5) (2000) 6968-6976.

[17] F.-Q. Zu, Temperature-Induced Liquid-Liquid Transition in Metallic Melts: A Brief Review on

the New Physical Phenomenon, Metals 5(1) (2015) 395-417.

[18] J. Wang, Y. He, J. Li, R. Hu, H. Kou, E. Beaugnon, Overheating dependent undercooling in a hypoeutectic Co-B alloy, Materials Chemistry and Physics 149-150 (2015) 17-20.

[19] X. Qiu, J. Li, J. Wang, T. Guo, H. Kou, E. Beaugnon, Effect of liquid-liquid structure transition on the nucleation in undercooled Co-Sn eutectic alloy, Materials Chemistry and Physics 170 (2016) 261-265.

[20] Y. Katayama, T. Mizutani, W. Utsumi, O. Shimomura, M. Yamakata, K.-i. Funakoshi, A first-order liquid-liquid phase transition in phosphorus, Nature 403(6766) (2000) 170-173.

[21] S. Zhang, L. Wang, X. Zhang, L. Qi, S. Zhang, M.Z. Ma, R. Liu, Polymorphism in glassy silicon: Inherited from liquid-liquid phase transition in supercooled liquid, Scientific reports 5 (2015) 8590.

[22] K.-i. Murata, H. Tanaka, Microscopic identification of the order parameter governing liquid-liquid transition in a molecular liquid, Proceedings of the National Academy of Sciences 112(19) (2015) 5956-5961.

[23] J. Mosses, C.D. Syme, K. Wynne, Order Parameter of the Liquid-Liquid Transition in a Molecular Liquid, The Journal of Physical Chemistry Letters 6(1) (2015) 38-43.

[24] G. Zhao, Y.J. Yu, X.M. Tan, Nature of the first-order liquid-liquid phase transition in supercooled silicon, The Journal of Chemical Physics 143(5) (2015) 054508.

[25] C.J. Wu, J.N. Glosli, G. Galli, F.H. Ree, Liquid-Liquid Phase Transition in Elemental Carbon: A First-Principles Investigation, Physical review letters 89(13) (2002) 135701.

[26] S.A. Khan, X.D. Wang, Q.P. Cao, D.X. Zhang, J.Z. Jiang, Structural evolution in liquid calcium under pressure, Journal of Non-Crystalline Solids 472 (2017) 25-30.

[27] M. Inui, Y. Kajihara, S. Hosokawa, K. Matsuda, Y. Tsuchiya, S. Tsutsui, A.Q.R. Baron, Dynamical sound speed and structural inhomogeneity in liquid Te studied by inelastic x-ray scattering, Journal of Non-Crystalline Solids: X 1 (2019) 100006.

[28] J. Wang, J. Li, R. Hu, H. Kou, E. Beaugnon, Evidence for the structure transition in a liquid Co-Sn alloy by in-situ magnetization measurement, Materials Letters 145 (2015) 261-263.

[29] K. Koga, H. Tanaka, X. C Zeng, First-order transition in confined water between high-density liquid and low-density amorphous phases, Nature 408 (2000) 564-567.

[30] W. Wu, L. Zhang, S. Liu, H. Ren, X. Zhou, H. Li, Liquid-Liquid Phase Transition in Nanoconfined Silicon Carbide, Journal of the American Chemical Society 138(8) (2016) 2815-2822.

[31] S.-J. Cheng, X.-F. Bian, J.-X. Zhang, X.-B. Qin, Z.-H. Wang, Correlation of viscosity and structural changes of indium melt, Materials Letters 57(26) (2003) 4191-4195.

[32] L. Wang, X. Bian, J. Liu, Discontinuous structural phase transition of liquid metal and alloys (1), Physics Letters A 326(5-6) (2004) 429-435.

[33] L. Wang, J. Liu, Discontinuous structural phase transition of liquid metal and alloys (2), Physics Letters A 328(2) (2004) 241-245.

[34] Y. Wu, X. Bian, Q. Meng, Y. Zhao, T. Mao, Y. Zhang, A critical transition state in liquid metals, Materials Letters 61(11) (2007) 2434-2438.

[35] W. Xu, M.T. Sandor, Y. Yu, H.-B. Ke, H.-P. Zhang, M.-Z. Li, W.-H. Wang, L. Liu, Y. Wu, Evidence of liquid-liquid transition in glass-forming $La_{50}Al_{35}Ni_{15}$ melt above liquidus temperature, Nature communications 6 (2015) 7696.

[36] Y. Yu, Z. Wu, O. Cojocaru-Mirédin, B. Zhu, X.-Y. Wang, N. Gao, Z.-Y. Huang, F.-Q. Zu, Dependence of Solidification for $Bi_2Te_{3-x}Se_x$ Alloys on Their Liquid States, Scientific reports 7(1)

(2017) 2463.

[37] L. Xiong, X. Wang, Q. Yu, H. Zhang, F. Zhang, Y. Sun, Q. Cao, H. Xie, T. Xiao, D. Zhang, Temperature-dependent structure evolution in liquid gallium, Acta Materialia 128 (2017) 304-312.

[38] T.H. Kim, K.F. Kelton, Structural study of supercooled liquid transition metals, The Journal of chemical physics 126(5) (2007) 054513.

[39] W.Y. Wang, J.J. Han, H.Z. Fang, J. Wang, Y.F. Liang, S.L. Shang, Y. Wang, X.J. Liu, L.J. Kecskes, S.N. Mathaudhu, X. Hui, Z.K. Liu, Anomalous structural dynamics in liquid $Al_{80}Cu_{20}$: An ab initio molecular dynamics study, Acta Materialia 97 (2015) 75-85.

[40] T. Iwashita, ., D.M. Nicholson, T. Egami, Elementary excitations and crossover phenomenon in liquids, Physical Review Letters 110(20) (2013) 205504.

[41] F. Demmel, A. Fraile, D. Szubrin, W.C. Pilgrim, C. Morkel, Experimental evidence for a dynamical crossover in liquid aluminium, Journal of Physics: Condensed Matter 27(45) (2015) 455102.

[42] D. Le Coq, A. Bytchkov, V. Honkimäki, B. Beuneu, E. Bychkov, Neutron and X-ray diffraction studies of TeCl 4 and TeBr 4 liquids, Journal of Non-Crystalline Solids 354(2) (2008) 259-262.

[43] D. Holland-Moritz, T. Schenk, P. Convert, T. Hansen, D.M. Herlach, Electromagnetic levitation apparatus for diffraction investigations on the short-range order of undercooled metallic melts, Measurement Science and Technology 16(2) (2005) 372-380.

[44] H. Kimura, M. Watanabe, K. Izumi, T. Hibiya, D. Holland-Moritz, T. Schenk, K.R. Bauchspieß, S. Schneider, I. Egry, K. Funakoshi, M. Hanfland, X-ray diffraction study of undercooled molten silicon, Applied Physics Letters 78(5) (2001) 604-606.

[45] G.N. Greaves, M.C. Wilding, S. Fearn, F. Kargl, L. Hennet, W. Bras, O. Majérus, C.M. Martin,

Liquid-liquid transitions, crystallization and long range fluctuations in supercooled yttrium oxide-aluminium oxide melts, Journal of Non-Crystalline Solids 355(10) (2009) 715-721.

[46] D. Lahiri, S. Sharma, A. Verma, V. Bathula, G. Dey, G. Schumacher, T. Scherb, H. Riesemeier, U. Reinholz, M. Radtke, S. Banerjee, Investigation of short-range structural order in $Zr_{69.5}Cu_{12}Ni_{11}Al_{7.5}$ and $Zr_{41.5}Ti_{41.5}Ni_{17}$ glasses, using X-ray absorption spectroscopy and ab initio molecular dynamics simulations, Journal of Synchroton Radiation 21 (2014) 1296-1304.

[47] F. Schmückle, P. Lamparter, S. Steeb, EXAFS Spectroscopy with Amorphous Transition Metal-Metalloid Alloys, Zeitschrift Für Naturforschung A 37(6) (1982) 572-580.

[48] P.F. Zou, H.P. Wang, S.J. Yang, L. Hu, B. Wei, Anomalous temperature dependence of liquid state density for $Ni_{50}Ti_{50}$ alloy investigated under electrostatic levitation state, Chemical Physics Letters 681 (2017) 101-104.

[49] G.A. Breaux, C.M. Neal, B. Cao, M.F. Jarrold, Melting, Premelting, and Structural Transitions in Size-Selected Aluminum Clusters with around 55 Atoms, Physical review letters 94(17) (2005).

[50] F.Q. Zu, Z.G. Zhu, L.J. Guo, B. Zhang, J.P. Shui, C.S. Liu, Liquid-liquid phase transition in Pb-Sn melts, Physical Review B 64(18) (2001) 180203.

[51] Y. He, J. Li, J. Wang, E. Yildiz, S. Pairis, E. Beaugnon, Temperature-induced structure transition in a liquid Co-B eutectic alloy, Materials Letters 234 (2019) 351-353.

[52] R. Liu, P. Jia, M. Li, H. Geng, J. Leng, Structure transition of $Sn_{57}Bi_{43}$ melt and its thermodynamic and kinetic characteristics, Materials Letters 145 (2015) 108-110.

[53] J.J. Li, W. Rhim, C. Kim, K. Samwer, W. Johnson, Evidence for a liquid-liquid phase transition in metallic fluids observed by electrostatic levitation, Acta Materialia 59(5) (2011) 2166-2171.

[54] C. Zhou, L. Hu, Q. Sun, J. Qin, X. Bian, Y. Yue, Indication of liquid-liquid phase transition in

CuZr-based melts, Applied Physics Letters, 103(17) (2013) 171904.

[55] J. Wang, Y. He, J. Li, R. Hu, H. Kou, E. Beaugnon, Experimental platform for solidification and in-situ magnetization measurement of undercooled melt under strong magnetic field, The Review of scientific instruments 86(2) (2015) 025102.

[56] F. Smallenburg, L. Filion, F. Sciortino, Erasing no-man's land by thermodynamically stabilizing the liquid-liquid transition in tetrahedral particles, Nature physics 10(9) (2014) 653-657.

[57] W. Wang, Y. Wu, L. Li, W. Zhai, X. Zhang, B. Wei, Liquid-liquid phase separation of freely falling undercooled ternary Fe-Cu-Sn alloy, Scientific reports 5 (2015).

[58] J.C. Palmer, F. Martelli, Y. Liu, R. Car, A.Z. Panagiotopoulos, P.G. Debenedetti, Metastable liquid-liquid transition in a molecular model of water, Nature 510(7505) (2014) 385-388.

[59] Y. He, H. Li, Y. Jiang, X. Li, X. Bian, Liquid-liquid phase transition and structure inheritance in carbon films, Scientific reports 4 (2014) 3635.

[60] C. Qiao, Y.R. Guo, J.J. Wang, H. Shen, S.Y. Wang, Y.X. Zheng, R.J. Zhang, L.Y. Chen, C.Z. Wang, K.M. Ho, Pressure induced short-range structural changes in supercooled liquid $Ge_2Sb_2Te_5$, Journal of Non-Crystalline Solids 503-504 (2019) 382-388.

[61] E.S. Tasci, M.H.F. Sluiter, A. Pasturel, P. Villars, Liquid structure as a guide for phase stability in the solid state: Discovery of a stable compound in the Au-Si alloy system, Acta Materialia 58(2) (2010) 449-456.

[62] C. Massobrio, F. Van Roon, A. Pasquarello, S. De Leeuw, Breakdown of intermediate-range order in liquid GeSe2 at high temperatures, Journal of Physics: Condensed Matter 12(46) (2000) L697.

[63] K. Kelton, A. Greer, D. Herlach, D. Holland-Moritz, The influence of order on the nucleation

barrier, MRS bulletin 29(12) (2004) 940-944.

[64] X. Li, F. Zu, W. Gao, X. Cui, L. Wang, G. Ding, Effects of the melt state on the microstructure of a Sn-3.5%Ag solder at different cooling rates, Applied Surface Science 258(15) (2012) 5677-5682.

[65] Y. He, J. Li, J. Wang, H. Kou, E. Beaugnon, Liquid-liquid structure transition and nucleation in undercooled Co-B eutectic alloys, Applied Physics A 123(6) (2017) 391.

[66] R.F. Tournier, Presence of intrinsic growth nuclei in overheated and undercooled liquid elements, Physica B: Condensed Matter 392(1-2) (2007) 79-91.

[67] R.F. Tournier, Crystallization of Supercooled Liquid Elements Induced by Superclusters Containing Magic Atom Numbers, Metals 4(3) (2014) 359-387.

[68] X. Li, F. Zu, J. Yu, B. Zhou, Effect of liquid–liquid transition on solidification of Bi-Sb10 wt% alloy, Phase Transitions 81(1) (2008) 43-50.

[69] M. Li, Y. Zhang, C. Wu, H.J.A.P.A. Geng, Effect of liquid-liquid structure transition on solidification of $Sn_{57}Bi_{43}$ alloy, Applied Physics A: Materilas Science & Processing 122(3) (2016) 171.

[70] P. Jia, X. Li, J. Zhang, K. Zhang, X. Teng, X. Hu, C. Yang, D. Zhao, Liquid-liquid structure transition and its effect on the solidification behaviors and microstructure of $Sn_{75}Bi_{25}$ alloy, Journal of Molecular Liquids 263 (2018) 218-227.

[71] X. Zhou, H. Kou, J. Wang, J. Li, L. Zhou, Crystallization and compressive behaviors of $Ti_{40}Zr_{25}Ni_{8}Cu_{9}Be_{18}$ BMG cast from different liquid states, Intermetallics 28 (2012) 45-50.

[72] Z. Hao Chen, W. Zheng, F.Q. Zu, X. Bing Zhu, Y. Feng Sun, Influence of Liquid Structure Change on Microstructure and Properties of SnZnBi Solder Alloy, Advanced Materials Research

463-464 (2012) 489-493.

[73] Q. Hu, H.C. Sheng, M.W. Fu, X.R.J.J.o.M.S. Zeng, Influence of melt temperature on the Invar effect in $(Fe_{71.2}B_{24}Y_{4.8})_{96}Nb_4$ bulk metallic glass, 49(20) (2014) 6900-6906.

[74] B. Predel, B - Co (Boron - Cobalt), 12B (2012) 30-33.

[75] S. Asai, Recent development and prospect of electromagnetic processing of materials, Science and Technology of Advanced Materials 1(4) (2000) 191.

[76] T. Garcin, S. Rivoirard, C. Elgoyhen, E. Beaugnon, Experimental evidence and thermodynamics analysis of high magnetic field effects on the austenite to ferrite transformation temperature in Fe-C-Mn alloys, Acta Materialia 58(6) (2010) 2026-2032.

[77] D.A. Molodov, A.D. Sheikh-Ali, Effect of magnetic field on texture evolution in titanium, Acta Materialia 52(14) (2004) 4377-4383.

[78] X.Y. Xiong, T.R. Finlayson, Phase transformation sequence and magnetic properties of melt-spun SmCo-based alloy after isochronal heat treatment, Journal of Applied Physics 104(10) (2008) 103910.

[79] P. De Rango, M. Lees, P. Lejay, A. Sulpice, R. Tournier, M. Ingold, P. Germi, M. Pernet, Texturing of magnetic materials at high temperature by solidification in a magnetic field, Nature 349(6312) (1991) 770.

[80] F. Gaucherand, E. Beaugnon, Magnetic texturing in ferromagnetic cobalt alloys, Physica B: Condensed Matter 346-347 (2004) 262-266.

[81] J. Wang, J. Li, R. Hu, H. Kou, E. Beaugnon, Magnetic field enhanced phase precipitation in an undercooled Co-Sn alloy, Materials Letters 139 (2015) 288-291.

[82] J. Wang, J. Li, R. Hu, H. Kou, E. Beaugnon, Anomalous magnetism and normal field instability

in supercooled liquid cobalt, Applied Physics Letters 105(14) (2014) 144101.

[83] X. Li, Y. Fautrelle, Z. Ren, A. Gagnoud, R. Moreau, Y. Zhang, C. Esling, Effect of a high magnetic field on the morphological instability and irregularity of the interface of a binary alloy during directional solidification, Acta Materialia 57(5) (2009) 1689-1701.

[84] T. Liu, Q. Wang, A. Gao, H. Zhang, J. He, Effects of a high magnetic field on the phase equilibria of Mn-Sb system during solidification process, Journal of Alloys and Compounds 509(19) (2011) 5822-5824.

[85] Z. Ren, X. Li, Y. Sun, Y. Gao, K. Deng, Y. Zhong, Influence of high magnetic field on peritectic transformation during solidification of Bi-Mn alloy, Calphad 30(3) (2006) 277-285.

[86] E. Savitsky, R. Torchinova, S. Turanov, Effect of crystallization in magnetic field on the structure and magnetic properties of Bi-Mn alloys, Journal of Crystal Growth 52 (1981) 519-523.

[87] C. Li, Z. Ren, W. Ren, K. Deng, G. Cao, Y. Zhong, Y. Wu, Design and application of differential thermal analysis apparatus in high magnetic fields, Review of Scientific Instruments 80(7) (2009) 073907.

[88] F. Gaucherand, E. Beaugnon, Magnetic susceptibility of high-Curie-temperature alloys near their melting point, Physica B: Condensed Matter 294 (2001) 96-101.

[89] S. Rivoirard, T. Garcin, E. Beaugnon, F. Gaucherand, High temperature dilatation measurements by in situ laser interferometry under high magnetic field, Review of Scientific Instruments 80(10) (2009) 103901.

[90] H. Yasuda, I. Ohnaka, Y. Ninomiya, R. Ishii, S. Fujita, K. Kishio, Levitation of metallic melt by using the simultaneous imposition of the alternating and the static magnetic fields, Journal of Crystal Growth 260(3-4) (2004) 475-485.

[91] B.L. Morris, A. Wold, Faraday Balance for Measuring Magnetic Susceptibility, Review of Scientific Instruments 39(12) (1968) 1937-1941.

[92] D. Kashchiev, A. Borissova, R.B. Hammond, K.J. Roberts, Dependence of the Critical Undercooling for Crystallization on the Cooling Rate, The Journal of Physical Chemistry B 114(16) (2010) 5441-5446.

[93] J. Schroers, D. Holland-Moritz, D.M. Herlach, K. Urban, Growth kinetics of quasicrystalline and polytetrahedral phases of Al-Pd-Mn, Al-Co, and Al-Fe from the undercooled melt, Physical Review B 61(21) (2000) 14500-14506.

[94] D. Herlach, Crystal nucleation and dendrite growth of metastable phases in undercooled melts, Journal of Alloys and Compounds 509 (2011) S13-S17.

[95] S.S. Nayak, H.J. Chang, D.H. Kim, S.K. Pabi, B.S. Murty, Formation of metastable phases and nanocomposite structures in rapidly solidified Al-Fe alloys, Materials Science and Engineering: A 528(18) (2011) 5967-5973.

[96] Y. Wu, M.V. Lototsky, J.K. Solberg, V.A. Yartys, W. Han, S.X. Zhou, Microstructure and novel hydrogen storage properties of melt-spun Mg-Ni-Mm alloys, Journal of Alloys and Compounds 477(1-2) (2009) 262-266.

[97] D.M. Herlach, Solidification from undercooled melts, Materials Science and Engineering: A 226 (1997) 348-356.

[98] D.M. Herlach, J. Gao, D. Holland-Moritz, T. Volkmann, Nucleation and phase-selection in undercooled melts, Materials Science and Engineering: A 375-377 (2004) 9-15.

[99] K. Kuribayashi, S. Ozawa, K. Nagayama, Y. Inatomi, Crystallization kinetics in Si-1at%Sn during rapid solidification in undercooled melt, Journal of Crystal Growth 468 (2017) 73-78.

[100] K. Nagashio, K. Kuribayashi, Phase selection in the undercooled peritectic $Y_3Fe_5O_{12}$ melt, Acta Materialia 50(8) (2002) 1973-1981.

[101] W.J. Yao, N. Wang, B. Wei, Containerless rapid solidification of highly undercooled Co-Si eutectic alloys, Materials Science and Engineering: A 344(1-2) (2003) 10-19.

[102] M. Li, K. Kuribayashi, Phase selection in the containerless solidification of undercooled $CaO \cdot 6Al_2O_3$ melts, Acta Materialia 52(12) (2004) 3639-3647.

[103] T. Hashimoto, K. Fujito, R. Sharma, E.R. Letts, P.T. Fini, J.S. Speck, S. Nakamura, Phase selection of microcrystalline GaN synthesized in supercritical ammonia, Journal of Crystal Growth 291(1) (2006) 100-106.

[104] F. Zhang, C. Lai, J. Zhang, Y. Zhang, Q. Zhou, H. Wang, Anomalous eutectics in intermediately and highly undercooled Ni-29.8at.%Si eutectic alloy, Journal of Crystal Growth 495 (2018) 37-45.

[105] Y. Lu, T. Li, F. Yabo, S. Jianbo, L. Dawei, G. Yang, Y. Zhou, Phase selection during solidification of undercooled $Ni_{70.2}Si_{29.8}$ eutectic alloy, Progress in Natural Science 19(11) (2009) 1619-1624.

[106] M. Krivilyov, T. Volkmann, J. Gao, J. Fransaer, Multiscale analysis of the effect of competitive nucleation on phase selection in rapid solidification of rare-earth ternary magnetic materials, Acta Materialia 60(1) (2012) 112-122.

[107] Y.K. Zhang, J. Gao, M. Kolbe, S. Klein, C. Yang, H. Yasuda, D.M. Herlach, C.A. Gandin, Phase selection and microstructure formation in undercooled Co-61.8at.% Si melts under various containerless processing conditions, Acta Materialia 61(13) (2013) 4861-4873.

[108] C. Yang, F. Liu, G. Yang, Y. Zhou, Structure evolution upon non-equilibrium solidification of

bulk undercooled Fe-B system, Journal of Crystal Growth 311(2) (2009) 404-412.

[109] C. Lai, H. Wang, Q. Pu, T. Xu, J. Yang, X. Zhang, F. Liu, Phase selection and re-melting-induced anomalous eutectics in undercooled Ni-38 wt% Si alloys, Journal of Materials Science 51(24) (2016) 10990-11001.

[110] M. Li §, S. Ozawa, K. Kuribayashi, On determining the phase-selection principle in solidification from undercooled melts-competitive nucleation or competitive growth?, Philosophical Magazine Letters 84(8) (2004) 483-493.

[111] D. Zhang, J. Xu, F. Liu, In Situ Observation of the Competition Between Metastable and Stable Phases in Solidification of Undercooled Fe-17at. pctB Alloy Melt, Metallurgical and Materials Transactions A 46(11) (2015) 5232-5239.

[112] W. Kurz, Solidification Microstructure-Processing Maps: Theory and Application, Advanced Engineering Materials 3(7) (2001) 443-452.

[113] Y. Watanabe, S. Oike, Formation mechanism of graded composition in Al-Al_2Cu functionally graded materials fabricated by a centrifugal in situ method, Acta Materialia 53(6) (2005) 1631-1641.

[114] V. Orera, J. Pena, P. Oliete, R. Merino, A. Larrea, Growth of eutectic ceramic structures by directional solidification methods, Journal of Crystal Growth 360 (2012) 99-104.

[115] Y. Zhang, W. Xu, H. Tan, Y. Li, Microstructure control and ductility improvement of La-Al-(Cu, Ni) composites by Bridgman solidification, Acta materialia 53(9) (2005) 2607-2616.

[116] P. Gilgien, A. Zryd, W. Kurz, Microstructure selection maps for Al-Fe alloys, Acta Metallurgica et Materialia 43(9) (1995) 3477-3487.

[117] M. Pierantoni, M. Gremaud, P. Magnin, D. Stoll, W. Kurz, The coupled zone of rapidly solidified AlSi alloys in laser treatment, Acta metallurgica et materialia 40(7) (1992) 1637-1644.

[118] H. Jones, W. Kurz, Growth temperatures and the limits of coupled growth in unidirectional solidification of Fe-C eutectic alloys, Metallurgical Transactions A 11(8) (1980) 1265-1273.

[119] X.X. Wei, W. Xu, J.L. Kang, M. Ferry, J.F. Li, Metastable $Co_{23}B_6$ phase solidified from deeply undercooled $Co_{79.3}B_{20.7}$ alloy melt, Journal of Materials Science 51(13) (2016) 6436-6443.

[120] X.X. Wei, W. Xu, J.L. Kang, M. Ferry, J.F. Li, Phase Selection in Solidification of Undercooled Co-B Alloys, Journal of Materials Science & Technology 33(4) (2017) 352-358.

[121] M. Li, K. Nagashio, T. Ishikawa, A. Mizuno, M. Adachi, M. Watanabe, S. Yoda, K. Kuribayashi, Y. Katayama, Microstructure formation and in situ phase identification from undercooled Co-61.8at.% Si melts solidified on an electromagnetic levitator and an electrostatic levitator, Acta Materialia 56(11) (2008) 2514-2525.

[122] G.E. Lloyd, Atomic number and crystallographic contrast images with the SEM: a review of backscattered electron techniques, Mineralogical Magazine 51(359) (1987) 3-19.

[123] X. Lin, Y.-Q. Cao, Z.-T. Wang, J. Cao, L.-L. Wang, W.-D. Huang, Regular eutectic and anomalous eutectic growth behavior in laser remelting of Ni-30wt%Sn alloys, Acta Materialia 126 (2017) 210-220.

[124] C. Yang, J. Gao, Y.K. Zhang, M. Kolbe, D.M. Herlach, New evidence for the dual origin of anomalous eutectic structures in undercooled Ni-Sn alloys: In situ observations and EBSD characterization, Acta Materialia 59(10) (2011) 3915-3926.

[125] M. Li, K. Nagashio, T. Ishikawa, S. Yoda, K. Kuribayashi, Microtexture and macrotexture formation in the containerless solidification of undercooled Ni-18.7 at.% Sn eutectic melts, Acta Materialia 53(3) (2005) 731-741.

[126] M. Aziz, W. Boettinger, On the transition from short-range diffusion-limited to collision-

limited growth in alloy solidification, Acta metallurgica et materialia 42(2) (1994) 527-537.

[127] J.W. Christian, The theory of transformations in metals and alloys Part I, Newnes 2002.

[128] D. Turnbull, Formation of crystal nuclei in liquid metals, Journal of Applied Physics 21(10) (1950) 1022-1028.

[129] F. Spaepen, A structural model for the solid-liquid interface in monatomic systems, Acta Metallurgica 23(6) (1975) 729-743.

[130] K. Nagashio, K. Kuribayashi, Y. Takamura, Direct crystallization of $Y_3Fe_5O_{12}$ garnet by containerless solidification processing, Materials Transactions 42(2) (2001) 233-237.

[131] Y.Q. Liu, X.S. Zhao, J. Yang, J.Y. Shen, Thermodynamic optimization of the boron-cobalt-iron system, Journal of Alloys and Compounds 509(14) (2011) 4805-4810.

[132] J. Lipton, W. Kurz, R. Trivedi, Rapid dendrite growth in undercooled alloys, Acta Metallurgica 35(4) (1987) 957-964.

[133] M. Aziz, Model for solute redistribution during rapid solidification, Journal of Applied Physics 53(2) (1982) 1158-1168.

[134] K. Eckler, R. Cochrane, D. Herlach, B. Feuerbacher, Non-equilibrium solidification in undercooled Ni-B alloys, Materials Science and Engineering: A 133 (1991) 702-705.

[135] P.K. Liao, K.E. Spear, The B-Co (Boron-Cobalt) system, Bulletin of Alloy Phase Diagrams 9(4) (1988) 452-457.

[136] S. Wei, M. Stolpe, O. Gross, W. Hembree, S. Hechler, J. Bednarcik, R. Busch, P. Lucas, Structural evolution on medium-range-order during the fragile-strong transition in $Ge_{15}Te_{85}$, Acta Materialia 129 (2017) 259-267.

[137] M.J. Cuthbertson, P.H. Poole, Mixturelike behavior near a liquid-liquid phase transition in

simulations of supercooled water, Physical review letters 106(11) (2011) 115706.

[138] P. Jia, J. Zhang, X. Teng, D. Zhao, Y. Wang, S. Hu, J. Xiang, S. Zhang, X. Hu, Liquid phase transition of $Sn_{50}Bi_{50}$ hypereutectic alloy and its thermodynamic and kinetic aspects, Journal of Molecular Liquids 251 (2018) 185-189.

[139] M.Y. Xie, X.F. Li, G.B. Xu, Y.T. Zhou, F.Q. Zu, Effects of liquid structure transition on solidification by the Newton thermal analysis method, Applied Physics A 113(2) (2013) 431-437.

[140] M. Gäumann, R. Trivedi, W. Kurz, Nucleation ahead of the advancing interface in directional solidification, Materials Science and Engineering: A 226 (1997) 763-769.

[141] Z. Wang, F. Wang, Y. Peng, Z. Zheng, Y. Han, Imaging the Homogeneous Nucleation During the Melting of Superheated Colloidal Crystals, Science 338(6103) (2012) 87-90.

[142] H.-T. Li, Y. Wang, Z. Fan, Mechanisms of enhanced heterogeneous nucleation during solidification in binary Al-Mg alloys, Acta Materialia 60(4) (2012) 1528-1537.

[143] S. Klein, D. Holland-Moritz, D.M. Herlach, Crystal nucleation in undercooled liquid zirconium, Physical Review B 80(21) (2009).

[144] J.H. Perepezko, G. Wilde, Melt undercooling and nucleation kinetics, Current Opinion in Solid State and Materials Science 20(1) (2016) 3-12.

[145] U. Dahlborg, M. Calvo-Dahlborg, P.S. Popel, V.E. Sidorov, Structure and properties of some glass-forming liquid alloys, Eur. Phys. J. B 14(4) (2000) 639-648.

[146] B. Yang, J.H. Perepezko, J.W. Schmelzer, Y. Gao, C. Schick, Dependence of crystal nucleation on prior liquid overheating by differential fast scanning calorimeter, The Journal of chemical physics 140(10) (2014) 104513.

[147] R.F. Tournier, E. Beaugnon, Texturing by cooling a metallic melt in a magnetic field, Science

and Technology of Advanced Materials 10(1) (2009) 014501.

[148] R.F. Tournier, Crystal growth nucleation and Fermi energy equalization of intrinsic spherical nuclei in glass-forming melts, Science and Technology of Advanced Materials 10(1) (2009) 014607.

[149] R. Tournier, Expected properties of gold melt containing intrinsic nuclei, Proceedings of the 6th International Conference on Electromagnetic Processing of Materials, EPM 2009, 2009, pp. 304-307.

[150] A. Leggett, Superfluid ^{3}He A is a liquid ferromagnet, Nature 270(5638) (1977) 585.

[151] E.M. Chudnovsky, Magnetic properties of amorphous ferromagnets, Journal of Applied Physics 64(10) (1988) 5770-5775.

[152] J. Reske, D.M. Herlach, F. Keuser, K. Maier, D. Platzek, Evidence for the existence of long-range magnetic ordering in a liquid undercooled metal, Physical review letters 75(4) (1995) 737-739.

[153] T. Shinohara, H. Watanabe, Nuclear Magnetic Resonance of Co^{59} in Ferromagnetic Cobalt Compounds Co_3B and Co_2B, Journal of the Physical Society of Japan 20(11) (1965) 2020-2027.

[154] D.M. Herlach, Non-equilibrium solidification of undercooled metallic metls, Materials Science and Engineering: R: Reports 12(4) (1994) 177-272.

[155] H. Okamoto, B-Co (Boron-Cobalt), Journal of Phase Equilibria 24(4) (2003) 376-376.

[156] I. Kaban, T. Halm, W. Hoyer, Structure of molten copper-germanium alloys, Journal of non-crystalline solids 288(1) (2001) 96-102.

[157] X. Oudet, Paramagnetism: An alternative view II: The Curie constant, Journal of Magnetism and Magnetic Materials 98(3) (1991) 307-332.

[158] A. Ghasemi, Compositional dependence of magnetization reversal mechanism, magnetic

interaction and Curie temperature of $Co_{1-x}Sr_xFe_2O_4$ spinel thin film, Journal of Alloys and Compounds 645 (2015) 467-477.

[159] D.S. Bertoldi, E.M. Bringa, E.N. Miranda, Analytical solution of the mean field Ising model for finite systems, Journal of Physics: Condensed Matter 24(22) (2012) 226004.

[160] V. Lopez-Dominguez, J.M. Hernàndez, J. Tejada, R.F. Ziolo, Colossal Reduction in Curie Temperature Due to Finite-Size Effects in $CoFe_2O_4$ Nanoparticles, Chemistry of Materials 25(1) (2013) 6-11.

[161] Y. Zhang, Z.P. Lu, S.G. Ma, P.K. Liaw, Z. Tang, Y.Q. Cheng, M.C. Gao, Guidelines in predicting phase formation of high-entropy alloys, MRS Communications 4(2) (2014) 57-62.

[162] Z.H.I. Sun, M. Guo, J. Vleugels, O. Van der Biest, B. Blanpain, Strong static magnetic field processing of metallic materials: A review, Current Opinion in Solid State and Materials Science 16(5) (2012) 254-267.

[163] S. Asai, K.-s. Sassa, M. Tahashi, Crystal orientation of non-magnetic materials by imposition of a high magnetic field, Science and Technology of Advanced Materials 4(5) (2003) 455-460.

[164] T. Liu, Q. Wang, A. Gao, C. Zhang, D. Li, J. He, Crystal orientation and grain alignment in a hypoeutectic Mn-Sb alloy under high magnetic field conditions, Journal of Alloys and Compounds 481(1-2) (2009) 755-760.

[165] E. Beaugnon, Levitation of organic materials, Nature 349 (1991) 470.

[166] J. Gao, M. Han, A. Kao, K. Pericleous, D.V. Alexandrov, P.K. Galenko, Dendritic growth velocities in an undercooled melt of pure nickel under static magnetic fields: A test of theory with convection, Acta Materialia 103 (2016) 184-191.

[167] C. Wei, J. Wang, Y. He, H. Kou, J. Li, The effect of high magnetic field on the microstructure

evolution of a Cu-Co alloy during non-equilibrium solidification, Journal of Crystal Growth 515 (2019) 78-82.

[168] W. Xuan, H. Liu, C. Li, Z. Ren, Y. Zhong, X. Li, G. Cao, Effect of a high magnetic field on microstructures of Ni-Based single crystal superalloy during seed melt-back, Metallurgical and Materials Transactions B 47(2) (2016) 828-833.

[169] S. Hu, Y. Dai, A. Gagnoud, Y. Fautrelle, R. Moreau, Z. Ren, K. Deng, C. Li, X. Li, Effect of a magnetic field on macro segregation of the primary silicon phase in hypereutectic Al-Si alloy during directional solidification, Journal of Alloys and Compounds 722 (2017) 108-115.

[170] Z. Lu, Y. Fautrelle, Z. Ren, X. Lu, X. Li, Effect of a high magnetic field on the morphology of the primary dendrite in directionally solidified Pb-25at.%Bi peritectic alloy, Materials Letters 160 (2015) 366-370.

[171] X. Li, Q. Li, Z. Ren, Y. Fautrelle, X. Lu, A. Gagnoud, Y. Zhang, C. Esling, H. Wang, Y. Dai, Investigation on the formation mechanism of irregular dendrite during directional solidification of Al-Cu alloys under a high magnetic field, Journal of Alloys and Compounds 581 (2013) 769-775.

[172] X. Li, Z. Ren, Y. Fautrelle, Y. Zhang, C. Esling, Morphological instabilities and alignment of lamellar eutectics during directional solidification under a strong magnetic field, Acta Materialia 58(4) (2010) 1403-1417.

[173] D. Du, Y. Fautrelle, Z. Ren, R. Moreau, X. Li, Effect of a high magnetic field on the growth of ternary Al-Cu-Ag alloys during directional solidification, Acta Materialia 121 (2016) 240-256.

[174] J. Wang, Y. He, J. Li, H. Kou, E. Beaugnon, Strong magnetic field effect on the nucleation of a highly undercooled Co-Sn melt, Scientific reports 7(1) (2017).

[175] R. Willnecker, D. Herlach, B. Feuerbacher, Grain refinement induced by a critical crystal

growth velocity in undercooled melts, Applied physics letters 56(4) (1990) 324-326.

[176] L. Liu, X.X. Wei, Q.S. Huang, J.F. Li, X.H. Cheng, Y.H. Zhou, Anomalous eutectic formation in the solidification of undercooled Co-Sn alloys, Journal of Crystal Growth 358 (2012) 20-28.

[177] Q. Wang, A. Gao, T. Liu, F. Liu, C. Zhang, J. He, Solidified microstructure evolution of Mn-Sb near-eutectic alloy under high magnetic field conditions, Journal of Materials Research 24(07) (2011) 2331-2337.

[178] Z.H.I. Sun, X. Guo, M. Guo, J. Vleugels, O. Van der Biest, B. Blanpain, Alignment of weakly magnetic metals during solidification in a strong magnetic field, Journal of Alloys and Compounds 551 (2013) 568-577.

[179] S. Asai, Application of high magnetic fields in inorganic materials processing, Modelling and Simulation in Materials Science and Engineering 12(2) (2004) R1.

[180] H. Morikawa, K. Sassa, S. Asai, Control of precipitating phase alignment and crystal orientation by imposition of a high magnetic field, Materials transactions, JIM 39(8) (1998) 814-818.

[181] J. Wang, J. Li, H. Kou, E. Beaugnon, Instability Pattern Formation in a Liquid Metal under High Magnetic Fields, Scientific reports 7(1) (2017) 2248.

[182] B. Michaud, E. Beaugnon, A. Sulpice, R. Tournier, J. Claverie, Experimental study of the magnetic orientation of ceramic fibers, Materials Transactions, JIM 41(8) (2000) 962-965.

[183] J.J. Abbott, O. Ergeneman, M.P. Kummer, A.M. Hirt, B.J. Nelson, Modeling magnetic torque and force for controlled manipulation of soft-magnetic bodies, IEEE Transactions on Robotics 23(6) (2007) 1247-1252.

[184] N. Olyanina, A. Bel'tyukov, V. Lad'yanov, Viscosity of Co-B melts, Russian Metallurgy

(Metally) 2016(2) (2016) 150-155.

[185] G. Diguet, E. Beaugnon, J.Y. Cavaillé, From dipolar interactions of a random distribution of ferromagnetic particles to magnetostriction, Journal of Magnetism and Magnetic Materials 321(5) (2009) 396-401.

[186] M.Z. Pedram, A. Shamloo, E. Ghafar-Zadeh, A. Alasty, Dynamic analysis of magnetic nanoparticles crossing cell membrane, Journal of Magnetism and Magnetic Materials 429 (2017) 372-378.

[187] C. Li, Z. Ren, W. Ren, Y. Wu, Y. Zhong, K. Deng, Nucleation and Growth Behaviors of Primary Phase in Al-Cu Hypereutectic Alloy in High Magnetic Fields, Progress In Electromagnetics Research 18 (2010) 71-84.

[188] J. Osborn, Demagnetizing factors of the general ellipsoid, Physical review 67(11-12) (1945) 351.

[189] X. Li, A. Gagnoud, Y. Fautrelle, Z. Ren, R. Moreau, Y. Zhang, C. Esling, Dendrite fragmentation and columnar-to-equiaxed transition during directional solidification at lower growth speed under a strong magnetic field, Acta Materialia 60(8) (2012) 3321-3332.

[190] J. Wang, S. Yue, Y. Fautrelle, P.D. Lee, X. Li, Y. Zhong, Z. Ren, Refinement and growth enhancement of Al_2Cu phase during magnetic field assisting directional solidification of hypereutectic Al-Cu alloy, Scientific reports 6 (2016) 24585.

Publication list

I: Publications in international journals

[1] **Y. He**, J. Li, L. Li, J. Wang, E. Yildiz, E. Beaugnon, Magnetic-field-induced chain-like assemblies of the primary phase during non-equilibrium solidification of a Co-B eutectic alloy: Experiments and modeling, Journal of Alloys and Compounds 815 (2020) 152446.

[2] **Y. He**, J. Li, J. Wang, E. Yildiz, S. Pairis, E. Beaugnon, Temperature-induced structure transition in a liquid Co-B eutectic alloy, Materials Letters 234 (2019) 351-353.

[3] **Y. He**, J. Li, L. Li, J. Wang, E. Yildiz, E. Beaugnon, Composition dependent characteristic transition temperatures of Co-B melts, Journal of Non-Crystalline Solids 522 (2019) 119583.

[4] **Y. He**, J. Li, J. Wang, E. Beaugnon, Transition from hypereutectic to hypoeutectic for rapid solidification in an undercooled Co-B alloy, Journal of Crystal Growth 499 (2018) 98-105.

[5] **Y. He**, J. Li, J. Wang, H. Kou, E. Beaugnon, Liquid–liquid structure transition and nucleation in undercooled Co-B eutectic alloys, Applied Physics A 123(6) (2017) 391.

[6] J. Wang, **Y. He**, J. Li, C. Li, H. Kou, P. Zhang, E. Beaugnon, Nucleation of supercooled Co melts under a high magnetic field, Materials Chemistry and Physics 225 (2019) 133-136.

[7] J. Wang, **Y. He**, J. Li, H. Kou, E. Beaugnon, Strong magnetic field effect on the nucleation of a highly undercooled Co-Sn melt, Scientific reports 7(1) (2017) 4958.

[8] J. Wang, **Y. He**, J. Li, H. Kou, E. Beaugnon, Reexaminations of the effects of magnetic field on the nucleation of undercooled Cu melt, Japanese Journal of Applied Physics 55(10) (2016) 105601.

[9] J. Wang, **Y. He**, J. Li, R. Hu, H. Kou, E. Beaugnon, Experimental platform for solidification and in-situ magnetization measurement of undercooled melt under strong magnetic field, The Review of scientific instruments 86(2) (2015) 025102.

[10] J. Wang, **Y. He**, J. Li, R. Hu, H. Kou, E. Beaugnon, Overheating dependent undercooling in a hypoeutectic Co-B alloy, Materials Chemistry and Physics 149-150 (2015) 17-20.

[11] C. Wei, J. Wang, **Y. He**, H. Kou, J. Li, The effect of high magnetic field on the microstructure evolution of a Cu-Co alloy during non-equilibrium solidification, Journal of Crystal Growth 515 (2019) 78-82.

[12] L. Li, J. Li, **Y. He**, W.Y. Wang, H. Kou, J. Wang, Tensile properties and deformation micromechanism of Ti-based metallic glass composite containing impurity elements, Journal of Alloys and Compounds 784 (2019) 220-230.

[13] L. Li, J. Li, **Y. He**, M. Lai, M. Zhu, W.Y. Wang, H. Kou, J. Wang, A new microscopic coordinated deformation model of Ti-based bulk metallic composites during tensile deformation, Scripta Materialia 172 (2019) 23-27.

[14] **Y. He**, J. Li, L. Li, J. Wang, E. Beaugnon, Overview: Liquid-liquid Structure Transition in Metallic Melt and its Impact on Solidification, to be submitted.

II: Contributions to international Conferences

[1] **International Conference on Magneto-Science 2019,** Oct 11-14, 2019, Hefei, China.
Oral: On the Eutectoid Decomposition of $Co_3B \rightarrow Co_2B+\alpha$-Co in a Co-B Eutectic Alloy.

[2] **Material Analysis and Processing in Magnetic fields**, June 26-29, 2018, Grenoble, France.

Poster: Liquid-liquid structure transition in a Co-B eutectic melt: an in-situ magnetization measurement.

[3] **International Conference on Magneto-Science 2017**, October 23-27, 2017, Reims, France.

Poster: Magnetic texturing by cooling a Co-18.5at.%B eutectic alloy in a magnetic field.

[4] **Chinese Materials Conference 2014**, July 4-7, 2014, Sichuan, China.

Oral: Effect of overheating on the magnetic properties and nucleation in a supercooled hypoeutectic Co-B liquid.

Acknowledgements

Upon the completion of the thesis, I would like to take this opportunity to express my sincere gratitude to all those who helped me during my study. Without their kind helps and supports, this thesis research would not have been possible.

The present work is accomplished at the Laboratoire National des Champs Magnétiques Intenses (LNCMI), Université Grenoble Alpes, Grenoble, France, and the State Key Laboratory of solidification processing, Northwestern Polytechnical University, Xi’an, China. I am so honored and appreciated to work in these two well-known laboratories and to be a student of the two famous universities.

My deepest gratitude goes first and foremost to my supervisors, Professor Eric Beaugnon, Professor Jinshan Li and Professor Jun Wang. They have offered me not only the guidance and supports to my Ph.D. study, but also the constant and selfless help in my daily life. Their useful suggestions, incisive comments and constructive criticism have contributed greatly to the completion of this thesis. I do appreciate their patience, encouragement, and professional instructions during my Ph.D. study.

I appreciate my colleges in the two laboratories and my friends who gave me their help and time listening to me and helping me work out my problems. Special thanks to Professor Haifeng Wang, Mr. Eyub Yildiz, Dr. Sébastien Pairis, Professor Sophie Rivoirard, Mr. Shibo Su, et al.

I am deeply indebted my beloved families for their loving considerations, endless supports and great confidence in me. A special gratitude and love would go to my wife, Mrs. Qi Li, who has always been loving, helping, encouraging, supporting and accompanying me.

I gratefully acknowledge the China Scholarship Council (CSC) for providing a Ph.D. scholarship to support my study in France. This work was supported by the National natural Science Foundation of China under Grant Nos. 51690163 and 51690164, the Program of Introducing Talents of Discipline to Universities under Grant No. B08040, the fund of the State Key Laboratory of Solidification Processing in NWPU under Grant Nos. 103-QP-2014 and 2019-TS-04 and the Fundamental Research Funds for the Central Universities under Grant No. 3102015ZY085. I gratefully acknowledge all these institutions for their financial support.